

LEVEL II

79-500

1

UCRL-62493

AD A063015

EQUATION OF STATE AND TRANSPORT  
MEASUREMENTS ON EXPANDED LIQUID  
METALS UP TO 8000°K AND 0.4 GPa

William Mark Hodgson  
(Ph.D. Thesis)

DDC  
RECEIVED  
9 JAN 1979  
E

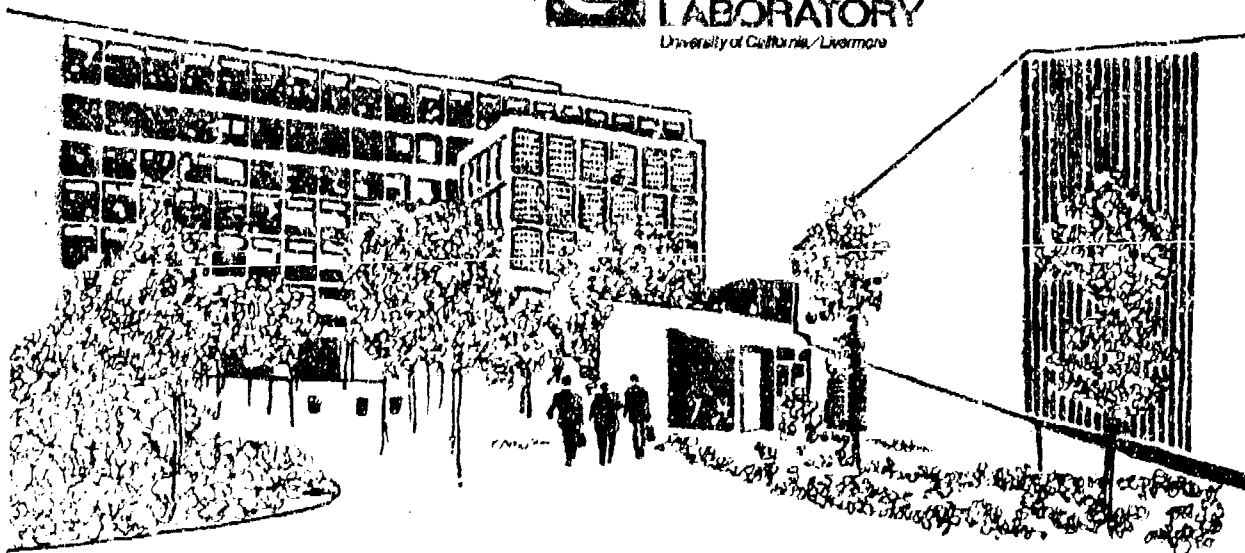
May 1978

Work performed under the auspices of the U.S. Department of  
Energy by the UCLL, under contract number W-7405-ENG-40

DDC FILE COPY



LAWRENCE  
LIVERMORE  
LABORATORY  
University of California/Livermore



DISTRIBUTION STATEMENT A

Approved for public release;  
Distribution Unlimited

79 01 08 016

# NOTICE

"This report was prepared as an account of work sponsored by the United States Government. Neither the United States nor the United States Department of Energy, nor any of their employees, nor any of their contractors, subcontractors, or their employees, makes any warranty, express or implied, or assumes any legal liability or responsibility for the accuracy, completeness or usefulness of any information, apparatus, product or process disclosed, or represents that its use would not infringe privately-owned rights."

# NOTICE

Reference to a company or product name does not imply approval or recommendation of the product by the University of California or the U.S. Department of Energy to the exclusion of others that may be suitable.

Printed in the United States of America

Available from

National Technical Information Service

U.S. Department of Commerce

5285 Port Royal Road

Springfield, VA 22161

Price: Printed Copy \$ : Microfiche \$3.00

Page Range	Domestic Price	Page Range	Domestic Price
001-025	\$ 4.00	326-350	\$12.00
026-050	4.50	351-375	12.50
051-075	5.25	376-400	13.00
076-100	6.00	401-425	13.25
101-125	6.50	426-450	14.00
126-150	7.25	451-475	14.50
151-175	8.00	476-500	15.00
176-200	9.00	501-525	15.25
201-225	9.25	526-550	15.50
226-250	9.50	551-575	16.25
251-275	10.75	576-600	16.50
276-300	11.00	601-up	1
301-325	11.75		

1 Add \$2.50 for each additional 100 page increment from 601 pages up.

UNCLASSIFIED

SECURITY CLASSIFICATION OF THIS PAGE (When Data Entered)

REPORT DOCUMENTATION PAGE		READ INSTRUCTIONS BEFORE COMPLETING FORM
1. REPORT NUMBER CI 79-50D	2. GOVT ACCESSION NO.	3. RECIPIENT'S CATALOG NUMBER
4. TITLE (and Subtitle) Equation of State and Transport Measurements on Expanded Liquid Metals up to 8000° and 0.4 GPa		5. TYPE OF REPORT & PERIOD COVERED Dissertation
7. AUTHOR(s) William Mark Hodgson		6. PERFORMING ORG. REPORT NUMBER
9. PERFORMING ORGANIZATION NAME AND ADDRESS AFIT Student at the University of California at Davis		8. CONTRACT OR GRANT NUMBER(s)
11. CONTROLLING OFFICE NAME AND ADDRESS AFIT/CI WPAFB OH 45433		10. PROGRAM ELEMENT, PROJECT, TASK AREA & WORK UNIT NUMBERS
14. MONITORING AGENCY NAME & ADDRESS (if different from Controlling Office)		12. REPORT DATE May 1978
		13. NUMBER OF PAGES 211
		15. SECURITY CLASS. (of this report) UNCLASSIFIED
		15a. DECLASSIFICATION/DOWNGRADING SCHEDULE
16. DISTRIBUTION STATEMENT (of this Report)  Approved for Public Release, Distribution Unlimited		
17. DISTRIBUTION STATEMENT (of the abstract entered in Block 20, if different from Report)		
18. SUPPLEMENTARY NOTES  APPROVED FOR PUBLIC RELEASE AFR 19017. JAN 2 1979 JOSEPH P. HIPPS, Major, USAF Director of Information, AFIT		
19. KEY WORDS (Continue on reverse side if necessary and identify by block number)		
20. ABSTRACT (Continue on reverse side if necessary and identify by block number)		

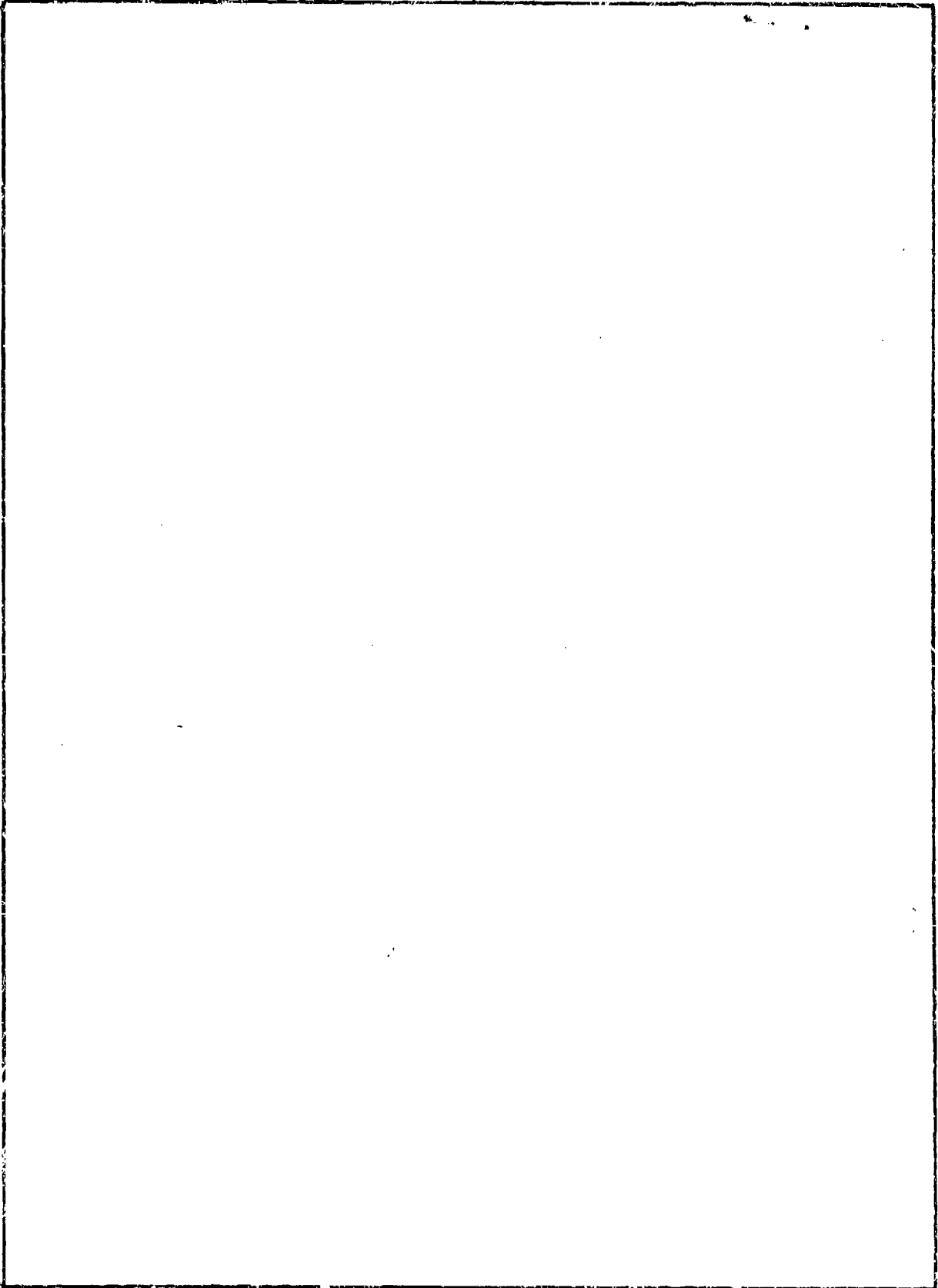
DD FORM 1 JAN 73 1473

EDITION OF 1 NOV 65 IS OBSOLETE

UNCLASSIFIED

SECURITY CLASSIFICATION OF THIS PAGE (When Data Entered)

SECURITY CLASSIFICATION OF THIS PAGE(When Data Entered)



SECURITY CLASSIFICATION OF THIS PAGE(When Data Entered)



## INSTRUCTIONS FOR PREPARATION OF REPORT DOCUMENTATION PAGE

**RESPONSIBILITY.** The controlling DoD office will be responsible for completion of the Report Documentation Page, DD Form 1473, in all technical reports prepared by or for DoD organizations.

**CLASSIFICATION.** Since this Report Documentation Page, DD Form 1473, is used in preparing announcements, bibliographies, and data banks, it should be unclassified if possible. If a classification is required, identify the classified items on the page by the appropriate symbol.

### COMPLETION GUIDE

**General.** Make Blocks 1, 4, 5, 6, 7, 11, 13, 15, and 16 agree with the corresponding information on the report cover. Leave Blocks 2 and 3 blank.

**Block 1.** Report Number. Enter the unique alphanumeric report number shown on the cover.

**Block 2.** Government Accession No. Leave blank. This space is for use by the Defense Documentation Center.

**Block 3.** Recipient's Catalog Number. Leave blank. This space is for the use of the report recipient to assist in future retrieval of the document.

**Block 4.** Title and Subtitle. Enter the title in all capital letters exactly as it appears on the publication. Titles should be unclassified whenever possible. Write out the English equivalent for Greek letters and mathematical symbols in the title (see "Abstracting Scientific and Technical Reports of Defense-sponsored RDT&E," AD-667 000). If the report has a subtitle, this subtitle should follow the main title, be separated by a comma or semicolon if appropriate, and be initially capitalized. If a publication has a title in a foreign language, translate the title into English and follow the English translation with the title in the original language. Make every effort to simplify the title before publication.

**Block 5.** Type of Report and Period Covered. Indicate here whether report is interim, final, etc., and, if applicable, inclusive dates of period covered, such as the life of a contract covered in a final contractor report.

**Block 6.** Performing Organization Report Number. Only numbers other than the official report number shown in Block 1, such as series numbers for in-house reports or a contractor/grantee number assigned by him, will be placed in this space. If no such numbers are used, leave this space blank.

**Block 7.** Author(s). Include corresponding information from the report cover. Give the name(s) of the author(s) in conventional order (for example, John R. Doe or, if author prefers, J. Robert Doe). In addition, list the affiliation of an author if it differs from that of the performing organization.

**Block 8.** Contract or Grant Number(s). For a contractor or grantee report, enter the complete contract or grant number(s) under which the work reported was accomplished. Leave blank in in-house reports.

**Block 9.** Performing Organization Name and Address. For in-house reports enter the name and address, including office symbol, of the performing activity. For contractor or grantee reports enter the name and address of the contractor or grantee who prepared the report and identify the appropriate corporate division, school, laboratory, etc., of the author. List city, state, and ZIP Code.

**Block 10.** Program Element, Project, Task Area, and Work Unit Numbers. Enter here the number code from the applicable Department of Defense form, such as the DD Form 1498, "Research and Technology Work Unit Summary" or the DE Form 1634, "Research and Development Planning Summary," which identifies the program element, project, task area, and work unit or equivalent under which the work was authorized.

**Block 11.** Controlling Office Name and Address. Enter the full, official name and address, including office symbol, of the controlling office. (Equates to funding/sponsoring agency. For definition see DoD Directive 5200.20, "Distribution Statements on Technical Documents.")

**Block 12.** Report Date. Enter here the day, month, and year or month and year as shown on the cover.

**Block 13.** Number of Pages. Enter the total number of pages.

**Block 14.** Monitoring Agency Name and Address (if different from Controlling Office). For use when the controlling or funding office does not directly administer a project, contract, or grant, but delegates the administrative responsibility to another organization.

**Blocks 15 & 15a.** Security Classification of the Report: Declassification/Downgrading Schedule of the Report. Enter in 15 the highest classification of the report. If appropriate, enter in 15a the declassification/downgrading schedule of the report, using the abbreviations for declassification/downgrading schedules listed in paragraph 4-207 of DoD 5200.1-R.

**Block 16.** Distribution Statement of the Report. Insert here the applicable distribution statement of the report from DoD Directive 5200.20, "Distribution Statements on Technical Documents."

**Block 17.** Distribution Statement (of the abstract entered in Block 20, if different from the distribution statement of the report). Insert here the applicable distribution statement of the abstract from DoD Directive 5200.20, "Distribution Statements on Technical Documents."

**Block 18.** Supplementary Notes. Enter information not included elsewhere but useful, such as: Prepared in cooperation with . . . Translation of (or by) . . . Presented at conference of . . . To be published in . . .

**Block 19.** Key Words. Select terms or short phrases that identify the principal subjects covered in the report, and are sufficiently specific and precise to be used as index entries for cataloging, conforming to standard terminology. The DoD "Thesaurus of Engineering and Scientific Terms" (TEST), AD-672 000, can be helpful.

**Block 20.** Abstract. The abstract should be a brief (not to exceed 200 words) factual summary of the most significant information contained in the report. If possible, the abstract of a classified report should be unclassified and the abstract to an unclassified report should consist of publicly-releasable information. If the report contains a significant bibliography or literature survey, mention it here. For information on preparing abstracts see "Abstracting Scientific and Technical Reports of Defense-Sponsored RDT&E," AD-667 000.

⑨ Doctoral thesis,



LAWRENCE LIVERMORE LABORATORY

University of California Livermore, California 94550

⑮ AFIT

⑲ CI-79-50D

⑫ 224 p.

⑭

UCRL-52493

⑥

EQUATION OF STATE AND TRANSPORT  
MEASUREMENTS ON EXPANDED LIQUID  
METALS UP TO 8000°K AND 0.4 GPa

⑩ William Mark Hodgson  
(Ph.D. Thesis)

⑪

⑮ W-7485-eng-48 MS date: May 1978

**DISTRIBUTION STATEMENT A**

Approved for public release;  
Distribution Unlimited

ACCESSION for	
NTIS	White Section <input checked="" type="checkbox"/>
DDC	Buff Section <input type="checkbox"/>
UNANNOUNCED	<input type="checkbox"/>
JUSTIFICATION _____	
BY	
DISTRIBUTION/AVAILABILITY CODES	
Dist.	SPECIAL
A	

390 999 79 01 08 016

## Equation of State and Transport Measurements on Expanded Liquid Metals up to 8000°K and 0.4 GPa

By

Major

WILLIAM MARK HODGSON

B.S. (University of Idaho) 1964

M.S. (Air Force Institute of Technology) 1966

## DISSERTATION

Submitted in partial satisfaction of the requirements for the degree of

DOCTOR OF PHILOSOPHY

in

# Engineering-Applied Science

in the

GRADUATE DIVISION

of the

UNIVERSITY OF CALIFORNIA

DAVIS

**Approved:**

proved: John W. Shaver  
~~A. H. M. M. M.~~

### Committee in Charge

Deposited in the University Library.

**Date**

Librarian

W. Mark Hodgson  
May 1978  
Applied Science

EQUATION OF STATE AND TRANSPORT MEASUREMENTS  
ON EXPANDED LIQUID METALS UP TO 8000 K AND 0.4 GPa

Abstract

Equilibrium measurements of pressure, enthalpy, density, temperature and resistivity have been made on liquid lead, platinum, gold-copper, uranium, niobium, and niobium-hafnium at high temperatures and pressures. A unique method of determining sample temperatures from multi-channel fast radiation pyrometry has been developed and used to calculate temperatures between 1600 and 8000 K without definitive emissivity information. Pseudo-potential theory has been used to model the lead resistivity and equation of state measurements and t-matrix theory has been applied to the uranium resistivity data.

The central experimental concept involves resistively heating an uncontained 1 mm diameter wire sample at a rate slow enough to allow uniform energy deposition and pressure equilibration, but fast enough to avoid significant heat loss and sample collapse through gravitational or instability effects. The containment vessel is several orders of magnitude larger than the sample and filled with an inert gas which maintains a constant pressure experimental environment independent of the sample's expanding volume. Energy from a 70 kJ capacitor bank drives a current as high as 35 KA through the wire bringing the material through a succession of hot, low density liquid states. Current through and voltage drop across a known segment of the wire is continuously monitored yielding information about sample enthalpy and resistance at any point in

time. In addition the sample surface temperature is measured with radiation pyrometry while streak photography provides a continuous record of the wire diameter. The streak record yields the sample volume which in turn can be used in conjunction with the resistance to compute the resistivity. The elevated pressures elevate the metal's boiling point, allowing the investigation of highly expanded yet still liquid (and conducting) states.

Recorded temperatures reached 8000 K for Pt and 5000 K for uranium with maximum temperatures for the remaining materials intermediate between these two values. An approximate mapping of the liquid-vapor two phase boundary has been made for lead to include an estimate of the critical point parameters. The metal to insulator transition in lead occurred at a specific volume expansion of approximately 3.65 for supercritical pressures. Equilibrium measurements have been extended at least a factor of two in temperature, enthalpy, and specific volume over previous static measurements for the materials of this work. Accuracy is estimated to be good enough to support definitive theoretical comparison, and in some cases, to produce reliable derivative quantities.

Pseudo-potential calculations using local potential form factors have been shown to be capable of predicting the liquid metal resistivity data over the limited range of previous work, but are found to be inadequate for modelling the resistivity of the most expanded states reached in these measurements. T-matrix calculations on uranium resistivity using APW supplied phase shifts produced reasonable agreement with the data only if suggested modifications were incorporated.

## Table of Contents

Abstract	ii
Table of Contents	iv
List of Figures	vi
List of Tables	viii
1. Introduction	1
2. The Experiment	10
The Isobaric Expansion Experiment	10
Diagnostics	18
Technical Concepts and Experimental Limitations	29
3. Data Analysis and Accuracy	42
Enthalpy	43
Volume (Density) Measurement	46
Temperature Analysis Technique	51
4. The Measured Properties of Liquid Pb, Pt, AuCu, U, Nb, and NbHf	63
Lead	63
Platinum	83
Gold-Copper	94
Uranium	103
Niobium	115
Niobium-Hafnium	123
5. Electrical Resistivity and Equation of State Modelling	132
Nearly Free Electron Resistivity	133
Electrical Resistivity and Equation of State	
Calculations on Liquid Lead	143
Uranium T-Matrix Calculations	148

6. Recommendations	157
Experimental Improvements	157
Projected Data and Computational Refinements	161
Applications of the Reported Data	162
References	164
Acknowledgements	172
Appendices	
A. Temperature Uncertainties	173
B. PYRO, A Computer Code for Determining Temperatures	180
C. Free Electron Relaxation Time	196
D. Local Potential Form Factors	203

## List of Figures

1. Schematic of Isobaric Expansion Experiment	3
2. Schematic Phase Diagram	11
3. IEX Sample and Anvil Assembly	12
4. Drawing of the IEX Sample Holding Anvil Assembly	14
5. Drawing of the IEX Pressure Cell Assembly	16
6. IEX Resistive Heating Circuit	17
7. Current and Voltage Oscilloscope Traces for Lead at 0.4 GPa	20
8. Pyrometer Response Voltage and Resulting SCT Temperature for Lead at 0.3 GPa	22
9. Expansion of Lead at 0.2 GPa	25
10. Liquid Lead Wire at 0.2 GPa and 0.1 GPa	27
11. The Isobaric Expansion Experiment	28
12. Skin Effect Calculation in Lead and Gold-Copper	34
13. SCT and TCT Temperatures for Lead at 0.3 GPa	56
14. Pyrometer Relative Intensity Calibration	60
15. Enthalpy vs Liquid Lead Temperature	64
16. Measured Emissivities of Liquid Lead	69
17. Volume Expansion of Liquid Lead	72
18. Thermal Expansion of Liquid Lead	76
19. Sound Velocity in Liquid Lead at 0.3 GPa	78
20. Liquid Lead Resistivity	82
21. Platinum Enthalpy vs Specific Volume	86
22. Platinum Enthalpy vs Temperature	90
23. Platinum Resistivity	92
24. Gold-Copper Resistivity	96



25. Gold-Copper Enthalpy vs Temperature	98
26. Gold-Copper Enthalpy vs Specific Volume	102
27. Uranium SCT Temperatures Calculated with Constant Emissivities	106
28. Uranium Temperatures Calculated with Temperature Dependent Emissivities	108
29. Uranium Enthalpy vs Temperature	112
30. Enthalpy vs Volume	114
31. Uranium Resistivity vs Enthalpy	116
32. Niobium Temperature	119
33. Niobium Enthalpy vs Temperature	120
34. Niobium Resistivity vs Enthalpy	122
35. Niobium-Hafnium Enthalpy vs Temperature	126
36. Niobium-Hafnium Enthalpy vs Volume	128
37. Niobium-Hafnium Resistivities	130
38. Melting Line Quantities for Lindemann Scaling	139
39. Hard Sphere Diameters for Liquid Lead	140
40. Liquid Lead Pseudo-Potential Calculations	144
41. T-Matrix Calculations on Uranium	152

## List of Tables

1. Measured Properties of Liquid Lead	66
2. Lead Emissivity Determination	68
3. Comparison of Tantalum and Lead Emissivities at 3270 K	71
4. Lead Enthalpy-Volume Least Squares Fit Coefficients	71
5. Comparison of Various Estimates for the Critical Point Parameters of Lead	74
6. Thermophysical Properties of Liquid Lead at 0.3 GPa	80
7. The Resistivity of Liquid Lead for $V/V_0$ between 1.15 and 3.65	84
8. Least Squares Coefficients for Fit of $V/V_0$ vs Temperature for Liquid Lead	84
9. Measured Properties of Platinum	88
10. Platinum Boiling Point	93
11. Measured Properties of Gold-Copper	99
12. Uranium Emissivities Derived from Run U80	105
13. Uranium Emissivities Derived from Run U85	105
14. U80 Emissivity Determination	109
15. U85 Emissivity Determination	110
16. Measured Properties of Liquid Uranium	117
17. Measured Properties of Niobium	124
18. Measured Properties of Niobium-Hafnium	131
19. "MET" Calculations on Liquid Lead	147
20. Fermi Surface Parameters of Liquid Uranium	154


EQUATION OF STATE AND TRANSPORT MEASUREMENTS  
ON EXPANDED LIQUID METALS UP TO 8000 K AND 0.4 GPa

W. Mark Hodgson

1. INTRODUCTION

→ The growing interest in controlled nuclear energy has been accompanied by a requirement for increased knowledge of the behavior of materials under high energy density conditions.<sup>(1)</sup> The efficiency of fission reactors can be improved with coolant fluids capable of maintaining large molecular densities at high temperatures and moderate pressures. Many inertial confinement fusion schemes have been proposed which depend on the optimum conversion of photon energy into kinetic energy.<sup>(2)</sup> The large fields necessary to magnetic confinement fusion concepts may require an extremely dense plasma to carry the generating currents.<sup>(3)</sup> Each of these requirements appear to be met best by characteristics peculiar to metals in the liquid state.

→ The high melting points of most of metals place the liquid state at temperatures too high for easy experimental investigation. Therefore, although liquid theory has received concerted attention with promising results it has yet to be corroborated or refuted over much of the pressure and temperature range pertinent to liquid metals.<sup>(4-6)</sup> A relatively complete mapping of the liquid region to include location of the liquid-vapor coexistence curve through the critical point is available only for Na, K, Rb, Cs, and Hg,<sup>(5)</sup> and for these not all measurements are in agreement. For most metals the critical region lies at higher pressures and temperatures than are accessible to conventional →

experimental techniques. The highly reactive nature of liquid metals makes their containment in uncontaminated form very difficult, and decreases the accuracy with which thermophysical properties can be determined.<sup>(7)</sup> Slow resistive heating methods have provided more precise enthalpy-temperature data but are limited to the melting temperature or below for uncontained samples.<sup>(8)</sup> Exploding wire techniques have for some time probed the highly expanded states although these experiments are generally conducted on time scales too fast to allow intra-sample communication and are plagued by questions of sample equilibrium.<sup>(9)</sup> Thus, both to provide needed engineering data and to stimulate theoretical understanding of low density liquid metals, an investigation of the equilibrium properties of metals above 2000 K and 0.1 GPa is the objective of this work. 

The isobaric expansion experiment (IEX) illustrated schematically in Figure 1 was designed to study liquid metals at pressures up to 0.5 GPa for temperatures as high as 8000 K.<sup>(10,11)</sup> The sample, a cylindrical wire approximately 25 mm long by 1 mm in diameter, is contained in a vessel which is pressurized with an inert gas. Energy from a 70 kJ capacitor bank is added at constant pressure through resistive heating. The enthalpy of a given state can be computed from the time integral of the measured current through the sample multiplied by the voltage drop across it. The sample, rigidly held between two current carrying leads, melts very quickly relieving the axial stresses. Thus expansion is in the radial direction only, and this dimension is continuously monitored with high speed streak photography.<sup>(12)</sup> In addition to current, voltage, pressure and wire diameter, the sample temperature is measured through three channel radiation pyrometry. These data allow

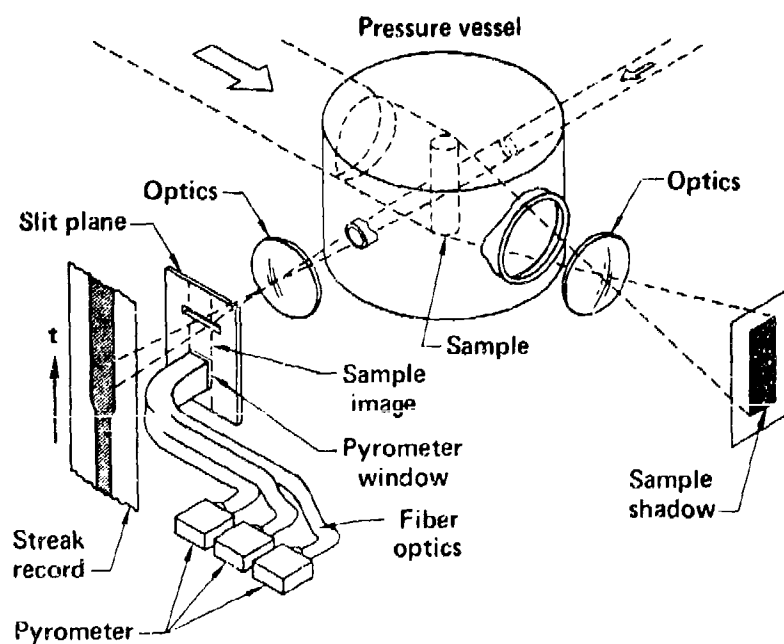


Fig. 1 Schematic of Isobaric Expansion Experiment

A metal specimen in the form of a wire about 1 mm thick and 25 mm long is clamped between metal jaws in a pressure vessel filled with inert gas. The sample is heated rapidly with a precisely shaped electrical pulse as the resulting expansion of the wire is recorded with high speed cameras looking through the sapphire windows of the pressure vessel.

determination of the enthalpy, density, temperature, and pressure of each of the states reached as a result of the resistive heating. Resistivity and, with less precision, derivative quantities such as heat capacity and the thermal expansion coefficient can also be calculated. Runs at different pressures enable an estimate of the compressibility which in turn can be used to calculate the bulk sound speed.

As will be discussed fully in the following section successful study of the liquid state with the IEX experiment depends critically on the choice of energy deposition rate. Heating rates are on the order of  $10^8$  K/sec which represents a compromise between ensuring equilibrium within the wire (slower rate) and completing the experiment before heat losses, hydrodynamic or magnetohydrodynamic instabilities, or gravitational effects become significant considerations. With the aid of physical arguments given in Chapter 2 the sample can be perceived to be a standing liquid column during most of the experimental run of 10-100  $\mu$ s. The liquid column radiates thermal energy sufficient to allow its temperature to be determined, but insignificant compared to the energy being added electrically. Conductive losses are still less significant and the sample remains essentially chemically isolated from its surroundings by a wall of inert gas.

Initial measurements have been made with this apparatus on refractory metals and are in the literature.<sup>(13,14,15)</sup> This thesis extends that work through an experimental investigation of temperature-density curves at several different pressures for lead, platinum, and a gold-copper alloy. Temperature studies are performed on uranium, niobium, and niobium-hafnium and these data are combined with previous work<sup>(13,15)</sup> to present more complete equation of state information on the materials.

Unique experimental results observed are the stable four-fold expansion of liquid lead and the measurable separation of lead isobars in the enthalpy density plane. Lead data are sufficient to permit a qualitative mapping of the liquid vapor coexistence curve and place definitive bounds on critical point parameters. Data on the remaining materials represent a large extension of the high temperature, low density limits of previous equilibrium measurements on these metals, and should provide a reliable test for theoretical modelling efforts.

A second major thrust of this project has been to establish a reliable technique for determining accurate temperatures from fast three channel radiation pyrometry. The posed problem is one of relating the emitted radiation of the sample to a true temperature in the absence of any specific information about the temperature and wavelength dependence of the emissivity. Three channels of pyrometry data provide five independent methods of determining a given temperature, each of them involving the unknown emissivities at the wavelengths of the channel windows. The technique developed in this work exploits the redundancy of the pyrometric data in a way proposed by Lincoln and Pettit.<sup>(16)</sup> Their contention is that the emissivity may be expressed as a simple function of temperature and wavelength, and that this functional relationship and the temperature can be uniquely determined by minimizing the difference among the independently calculated temperatures over a broad temperature range. A weakly linear emissivity temperature dependence has been found to produce the requisite agreement for much of the data studied, but the dependence is not considered significant in view of experimental uncertainties. The analysis technique has led to temperatures, however, which are consistent and reproducible from run to run.

A third goal of the present work has been to compare the experimental results with calculations based upon the Ziman nearly free electron model of a liquid metal.<sup>(17)</sup> The parameter chosen for the initial comparison has been the resistivity and the calculation is dependent on experimental temperatures and densities. Following reasoning first expounded by Ashcroft<sup>(18)</sup>, a guiding philosophy of the theoretical modelling has been to choose extremely simple local pseudo-potential form factors with a minimum number of parameters which are adjusted within constraints imposed by published band structure measurements to give agreement with measured resistivities across a broad range of densities.

The most extensive calculations have been carried out on lead, a known "good" free electron metal. Results indicate good agreement of the measurement and calculation over the very limited density range of previous experimental work, but that the theory does not result in strong enough density dependence over the greatly expanded range of the current work. It was also found that pseudo-potentials giving reasonable results for resistivity did not necessarily lead to a meaningful equation of state nor agree with published potentials based upon modelling measured band structures. The inadequate density dependence of the model is examined through a parametric sensitivity study. Although the work of this thesis provides a broad data base against which to compare theory and discover areas of disagreement, the basic failings of the theory have not been resolved and are beyond the scope of this thesis.

Resistivity calculations have also been made on uranium which presents a more difficult theoretical problem because of the presence of the d and f electrons in the conduction band. The theory applied is that discussed by Hirata, et al<sup>(19)</sup> in which, as in pseudo-potential



formalism, the electron scattering is described in terms of a reaction matrix between plane wave states. In this case, though, the matrix is known as the t-matrix, and the elements depend upon the phase shifts of the atomic potentials as well as the energy at which the scattering takes place. These necessary phase shifts are extrapolated from self consistent augmented plane wave (APW) calculations done by McMahan for compressed uranium.<sup>(20)</sup> The calculations require choices for the effective electron mass and the effective number of free electrons in the conduction band which are not straightforward and have not as yet provided completely satisfactory results. In fact the overall modelling effort is just begun and provides a fertile area for further work.

Chapter 2 contains a description of the experiment and discussion of the considerations necessary to assuming sample equilibrium at each state reached during the electrical energy deposition. The experimental objective, equilibrium investigation of the liquid state of metals, is shown to be achieved through techniques that impose constraints upon the choice of sample and limitations on the temperatures and pressures that can be reached. Chapter 3 deals with the data analysis calculations and develops an estimate of the experimental uncertainty inherent in the measurements. Because the isobaric expansion experiment has been developed in an evolutionary manner over a period of ten years much of the subject matter of Chapters 2 and 3 is in the literature and is presented in outline form only for completeness. For this reason the emphasis in Chapter 3 will be on the temperature determining procedure which is unique to this work and other diagnostic techniques incompletely developed elsewhere.

The experimental results of this project are presented in Chapter 4. These include all properties reported for lead, platinum and gold-copper, and the temperature-enthalpy measurements made for niobium, niobium-hafnium, and uranium. Density enthalpy measurements made by Shaner, et al<sup>(15)</sup> are included for the latter three materials.

The data discussed in Chapter 4 are initially taken in analog form as oscilloscope traces, next digitized with a film reader, and then at various stages of the data reduction are reconstructed using piecewise quadratic fits or cubic splines. This procedure is necessary in order to correlate current, voltage, pyrometer voltages, and streak photography records read at arbitrary times. Using this technique the time parameter is eliminated altogether and the density, temperature and resistivity are plotted as functions of the measured enthalpy which is added electrically. The processed data are then least squares fit as a function of enthalpy to whatever order is deemed necessary for an acceptable fit of the data. The resulting polynomials are given and used to generate tables of thermophysical properties.

Chapter 5 contains a description of the nearly free electron theory that is used to model selected resistivity data. Also reported are lead equation of state calculations done using the same theory as applied in a code under development by Ross.<sup>(21)</sup> Both the pseudo-potential and t-matrix calculations involve the use of a structure factor which is itself the Fourier transform of the pair distribution function of the ionic cores in the liquid metal. For these calculations the ionic cores are modelled as hard spheres and the structure factor used is that developed by Ashcroft and Lekner from a known solution to the Percus-Yevick equation<sup>(47)</sup>. The resistivity determination employs a

unique method of choosing the hard sphere diameters as a function of liquid density and these diameters are compared to those chosen by more conventional techniques. As has been indicated above, the theoretical modelling is preliminary. Satisfactory exploitation of the range of data presented should go far beyond the scope of this work. Possible avenues of theoretical investigation as well as desirable experimental improvements are discussed in Chapter 6.

## 2. THE EXPERIMENT

The isobaric expansion experiment (IEX) was designed to circumvent the containment problems accompanying experimental investigations of hot liquid metals at high temperatures and moderate pressures. (10,11)

Figure 2 illustrates schematically the thermodynamic region of concern to this project. Indicated numbers are estimates for lead based upon the data and arguments advanced in Chapter 4. Throughout much of the region of interest the sample is at temperatures and pressures above which any conceivable container material could maintain its integrity. Even at temperatures at which a container could retain sufficient strength, the corrosive nature of the sample might cause a reaction which would confuse the meaning of the measurements. To avoid these inherent difficulties of externally heated, contained sample techniques the IEX leaves the sample completely uncontained and adds energy through resistive heating. This chapter includes a detailed description of the experiment and its diagnostics, and a discussion of the technical concepts necessary to the essential assumption of equilibrium heating.

### The Isobaric Expansion Experiment

Central to the IEX is the 1 mm x 25 mm cylindrical sample pictured in Figure 3. Energy stored in a 70 kJ capacitor bank drives currents as high as 40 ka through the sample for experimental times as long as 70  $\mu$ s. The current lead is electrically isolated from the massive metal anvil in the lower part of the figure as are the leads accessing the metal ribbon voltage probes shown lightly contacting the sample. A cylindrical conducting cap (not shown) fits over the sample holder contacting both the current lead at the upper end of the sample and the anvil just above

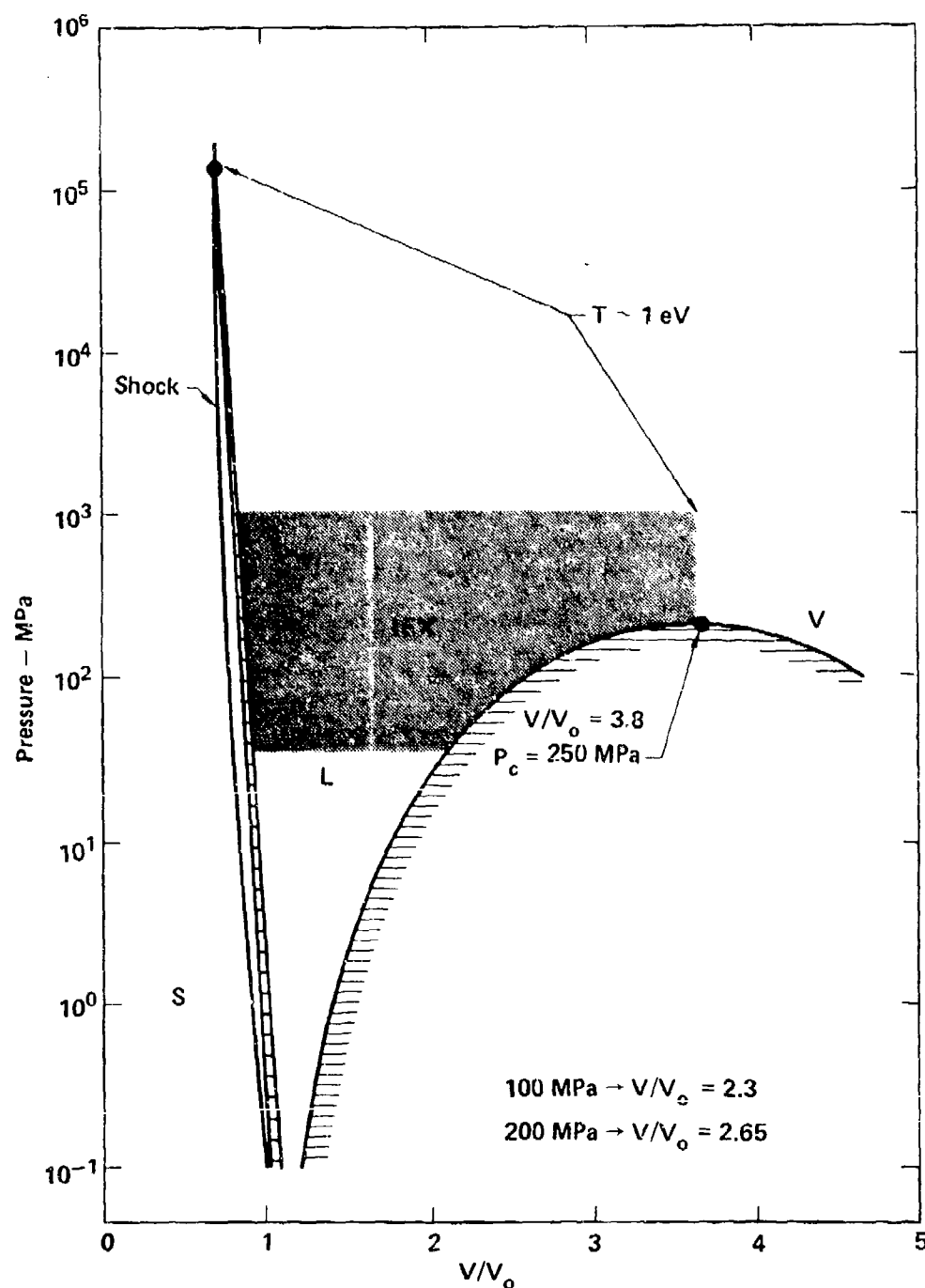


Fig. 2 Schematic Phase Diagram

This is a schematic diagram of the thermodynamic states that can be reached with the IEX experiment. Included for reference are the experimental track of shock driven experiments (principle Hugoniot), the solid liquid two phase region (shaded area at left), and the boundary of the liquid-vapor two phase region. An experimental run follows a horizontal track beginning at normal density and elevated pressure and continues to an expansion at which the sample begins to boil for subcritical pressures or until the critical density is reached for supercritical densities. Specific numbers are those determined experimentally for lead.



Fig. 3 IEX Sample and Anvil Assembly

The 1 mm thick by 25 mm long sample is firmly clamped between two current carrying jaws with voltage measuring probes lightly contacting at a precisely measured separation. The assembly is enshrouded in a grounding cap (not shown) and placed within a pressure vessel in which the O-ring backed indium-coated hoop shown at the base forms the critical pressure seal.

the neoprene O-ring. The cap provides a return path coaxial with the sample ensuring that the magnetic forces generated are azimuthally symmetric and thus do not cause any motion of the sample. The voltage probes are attached to a high impedance differential amplifier allowing the voltage drop across a precisely measured section of the wire to be continuously monitored with minimum perturbing effect on the sample current and thus minimum contact resistance effect. The assembly pictured in Figure 3 is placed in a pressure vessel, the inner diameter of which is only slightly larger than the largest diameter of the anvil. Inert gas is used to pressurize the cell pushing down on the O-ring which in turn presses on the indium coated metal seal just below it. The indium seal has a triangular cross section so that the gas pressure as transmitted by the O-ring forces the lower outer edge out against the inner wall of the vessel and the upper inner edge in against the sample holder. The higher the gas pressure the more the indium seal becomes deformed and the tighter becomes the double edge sealing action. Although care must be taken with the indium seal, pressures of 0.4 GPa are reached routinely and the seal arrangement does not appear to be the limiting consideration.

Details of the anvil are shown in Figure 4 where the assembly of Figure 3 is inverted to the orientation it assumes in the pressure vessel. It is necessary to compromise the cylindrical symmetry of the brass grounding cap in order to provide viewing ports for the optical diagnostics. These ports are covered with thin sapphire shim windows whose function is to protect the interior of the vessel from splattering sample. The placement of the voltage probes on opposite sides of the

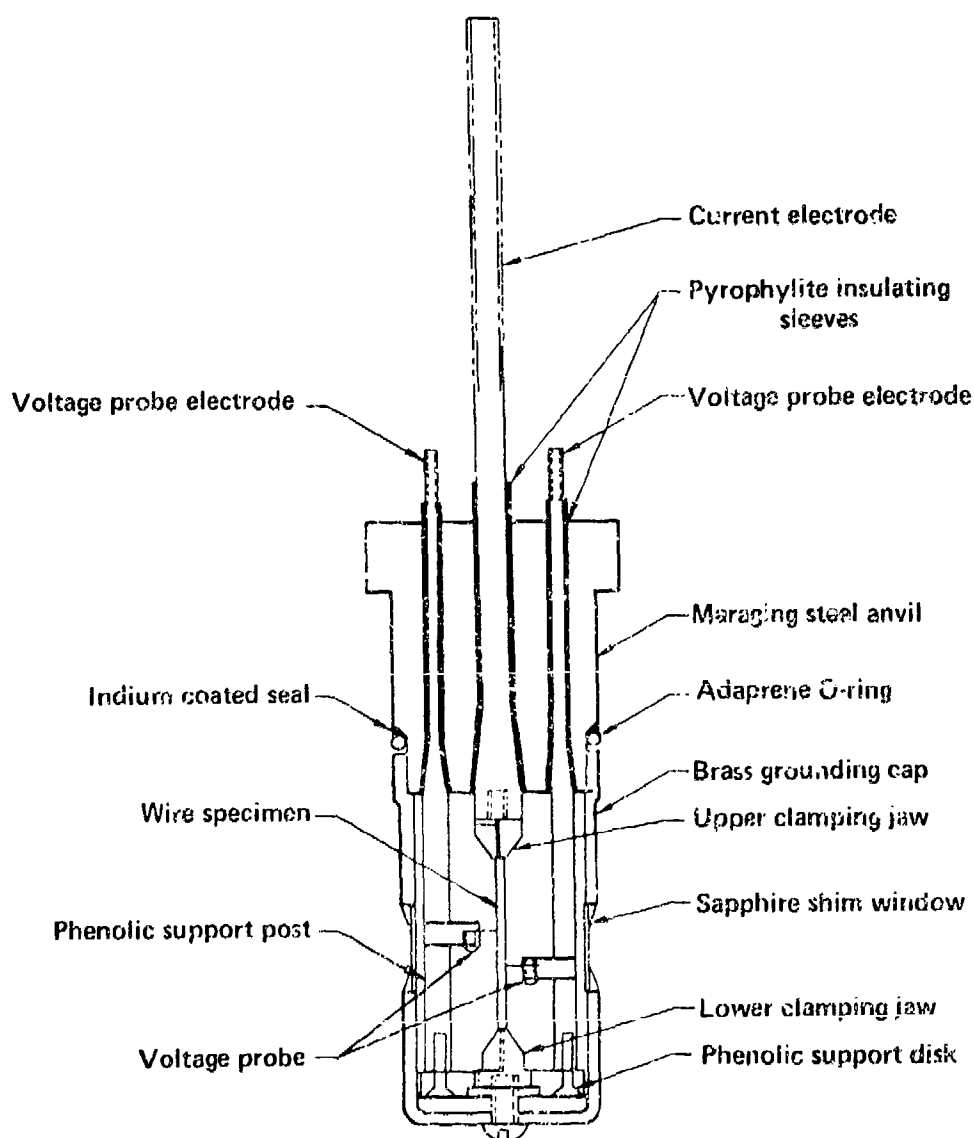


Fig. 4 Drawing of the IEX Sample Holding Anvil Assembly

This cutaway drawing shows the anvil assembly in the orientation it assumes within the pressure vessel. Resistive heating current flows through the central electrode to the sample from whence it returns to the anvil body through the brass grounding cap. Both the current electrode and the voltage probe electrodes are insulated from and sealed to the anvil body with epoxy bathed pyrophyllite liners.



sample reduces the inductive coupling of the voltage measuring circuit with the resistive heating circuit.

Figure 5 is a drawing of the main cell assembly which is machined in two parts, the inner of Maraging steel and the outer of tool steel, which are then pressed together. An aluminum jacket is bolted around the steel to act as a shrapnel shield in case of catastrophic failure. The sets of viewing ports are placed at  $90^\circ$  to one another and sealed with 20 cm thick cone shaped sapphire windows encased in pyrophyllite liners and epoxied in place, permitting a clear line of sight aperture 1.4 cm in diameter. This window arrangement is the pressure limiting component of the experiment. At pressures above 0.4 GPa the difference between the hoop stress and the axial stress in the vessel distorts the viewing port which either cleaves the window or breaks the window to vessel seal. The vessel itself and its associated pressure system are capable of 1 GPa, a considerable improvement over the system discussed in reference 12.

Electrically the sample is an element of the circuit shown schematically in Figure 6. Ballast resistors  $R_1$  and  $R_2$  are chosen to dominate the characteristics of the circuit and together typically total approximately  $0.5 \Omega$ . Current is initiated by firing spark gap 1 and can be shunted around the sample by firing spark gap 2. The coil is a precisely calibrated Pearson probe designed to measure sample current inductively.

The cell is pressurized with either helium or argon, the former having the advantage of a lower index of refraction and the latter being much easier to contain. Experimental pressure is reached by compressing an initial volume of gas successively with 1:1 and then 10:1 hydraulic

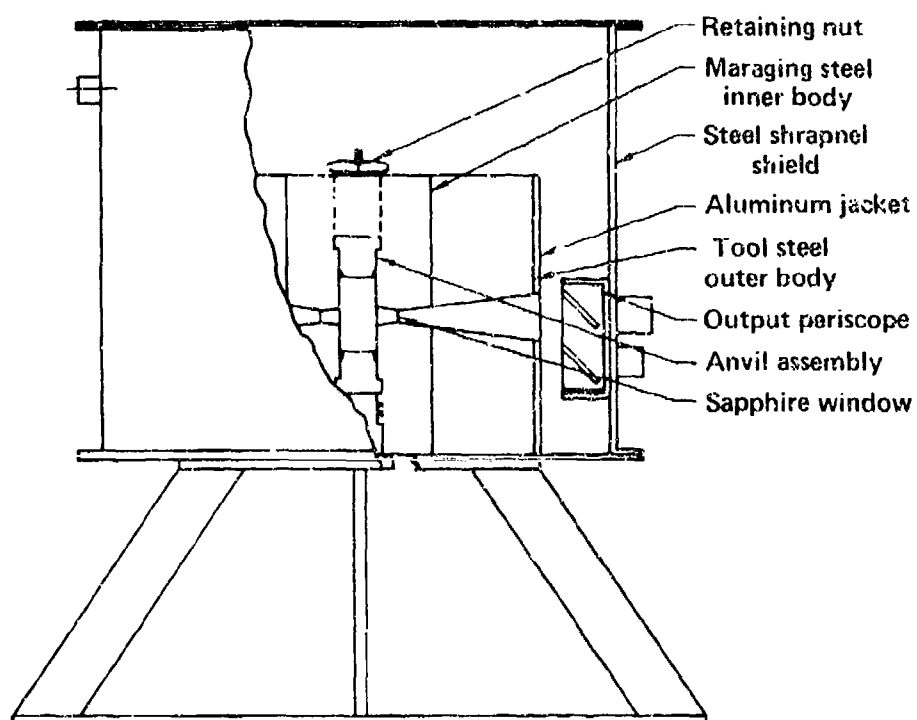


Fig. 5 Drawing of the IEX Pressure Cell Assembly

Major components of the IEX pressure cell are the inner sleeve of Maraging steel which is pressed into the outer sleeve of tool steel. A jacket of aluminum is bolted about these with a further steel shrapnel shield encasing the entire assembly. Two anvil bases are shown sealing the interior while being retained by large steel nuts.

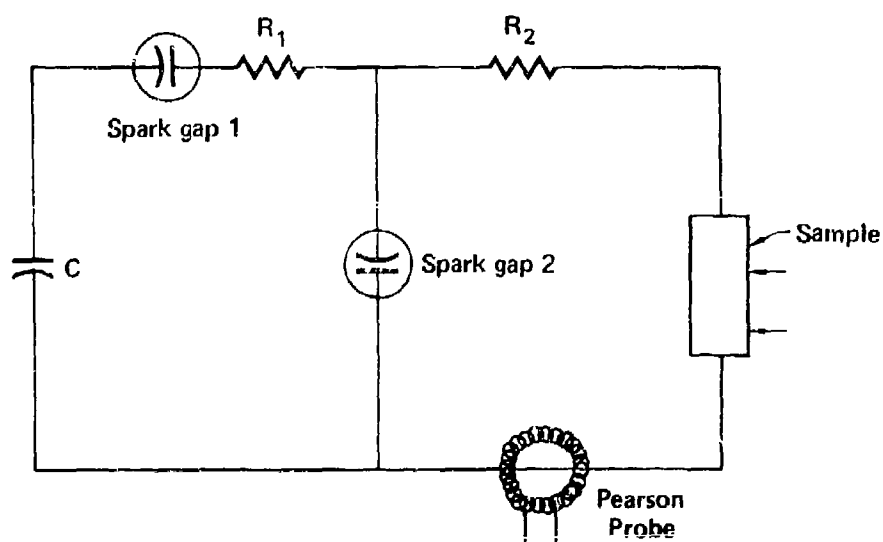


Fig. 6 IEX Resistive Heating Circuit

Energy stored in capacitor C drives a current through ballast resistors  $R_1$  and  $R_2$ , the sample, and the toroidal loop which measures current inductively. The closing of spark gap 1 initiates the current while closing spark gap 2 shunts current around the sample.

rams. Hydraulic pressure is provided by an air driven Haskell pump. After a delay of two to three minutes to allow the compressed gas to equilibrate with the room temperature environment the main capacitor bank is charged. The fire sequence is controlled electronically using a pulse generator and a delay chassis. A single pulse serially opens the oscilloscope camera shutters, triggers the oscilloscopes and a high speed image converter streak camera, initiates current through the sample by firing spark gap 1 (Figure 6), crowbars that current by firing spark gap 2, and Q-switches a ruby laser which back lights the sample for a post shot picture. The resulting data is described in the following section.

### Diagnostics

As initially conceived the isobaric expansion experiment was to provide the enthalpy, pressure, and density information necessary to generate an equation of state that was both analogous to and complimentary to that produced by shock compression work.<sup>(22)</sup> Temperature could then be inferred by assuming that heat capacity measured by more conventional techniques at relatively low temperatures would be applicable to the high temperature regimes attainable with the IEX. To this end the original pressure vessel was fitted with beryllium windows through which a pulsed x-ray source made a radiograph of the expanded sample once during an experimental run.<sup>(10)</sup> This experimental scheme proved inadequate for at least two reasons. First, small errors in the assumed heat capacity lead to prohibitively large errors in the calculated temperatures when extrapolated over a broad range of enthalpies. Secondly, in practice it proved very difficult to make consistent representative density measurements when limited to a single

point per run. These considerations led to the current diagnostic capability discussed in reference (12) and described in the following paragraphs.

Pressure is monitored with a gauge precise to 0.5 MPa. The sample occupies less than 0.1% of the pressurized volume so that even four-fold volume expansions alter the pressure imperceptibly. Current through the sample is measured continuously through the inductive response of the Pearson probe indicated in Figure 6. The potential at two points on the sample is fed to a differential preamplifier for display on an oscilloscope. Typical current and voltage traces are displayed in Figure 7, taken from a 0.4 GPa run made on lead. The overall shape of the current trace is indicative of the slightly overdamped nature of the heating circuit, and the points at which the bank is fired and crow-barred are readily identifiable features. The early part of the voltage record is characteristic of a significant inductive contribution to the overall sample impedance, a feature that must be corrected for in determining the enthalpy of the material. Also easily recognizable on the voltage trace are the beginning and ending of melt, the long linear liquid region, and the increased curvature of the trace as the sample approaches the liquid vapor two phase region. Pressure, voltage, and current measurements remain essentially as developed in ref. 10 and are made on each experimental run.

In order to obtain maximum sample radiation for the pyrometric measurement the temperature and density data are taken on separate runs and then correlated through common enthalpies. For temperature data the sample, magnified a factor of five, is imaged upon the end of a randomized fibre optic bundle. A slit is placed just in front of the

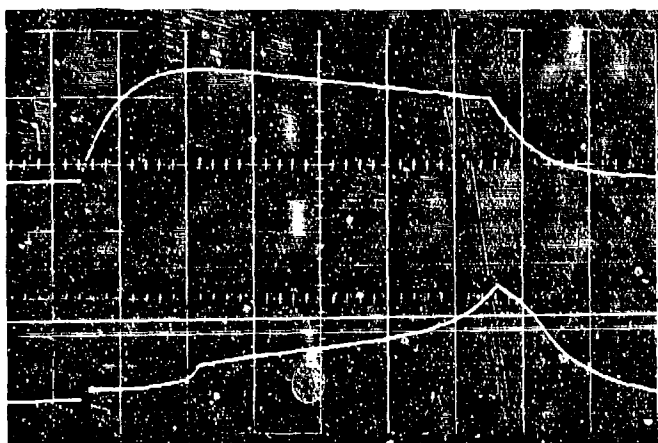


Fig. 7 Current and Voltage Oscilloscope Traces for Lead at 0.4 GPa

The upper trace, scaled at 8307 amps/cm, exhibits the overdamped nature of the circuit of Fig. 6 with a rapid rise following bankfire, a long period of slow decay, and an exponential decay after crowbar. The voltage trace, scaled at 200 volts/cm begins with a sharply rising inductive signal which diminishes as the sample is heated through the solid phase. Melt is identified by the short steep linear region which is followed by a longer more slowly increasing portion indicative of the liquid phase which in turn bends sharply upward as the liquid vapor two phase region is approached. Time base for both traces is 5  $\mu$ s/cm.

fibre optic bundle to select a 0.8 mm x 3 mm section of the sample for viewing. The sample edges are occluded because radiation from the edges has been observed to not strictly obey Lambert's law. The fibre bundle is branched randomly among three pyrometers, each thus viewing the same area of the sample. Radiation exits the trifurcated bundle through 100 nm width interference filters centered at three separate wavelengths within the visible and near infrared region of the spectrum. The response of the photodiodes is amplified logarithmically in each channel and displayed as an oscilloscope trace. The intensity within the window of an individual pyrometer typically varies by as much as four orders of magnitude over a temperature range of 2000-8000 K. As will be discussed in the following chapter the accuracy of the temperature determination benefits from having low intensity low temperature data on the same trace with the high temperature data. This requirement to have the complete temperature range measureable in each channel dictated that the better precision inherent in linear amplification be sacrificed in favor of the greater range of a logarithmic response. The unusually broad temperature range along with the electrically noisy environment created by the bank circuit made necessary a special very stable amplifier which was designed and built for the experiment prior to this work.<sup>(12)</sup> Temperature data for lead at 0.3 GPa recorded in the 650 nm channel is shown in Figure 8 along with the temperatures calculated from that data. Except for the noise signal caused by bankfire and crowbar the trace is relatively featureless which indicates that the sample remained in a single phase over the range of recorded temperatures.

Calibration of the temperature data is best served if the sample undergoes a phase transition in the range of good detector sensitivity.

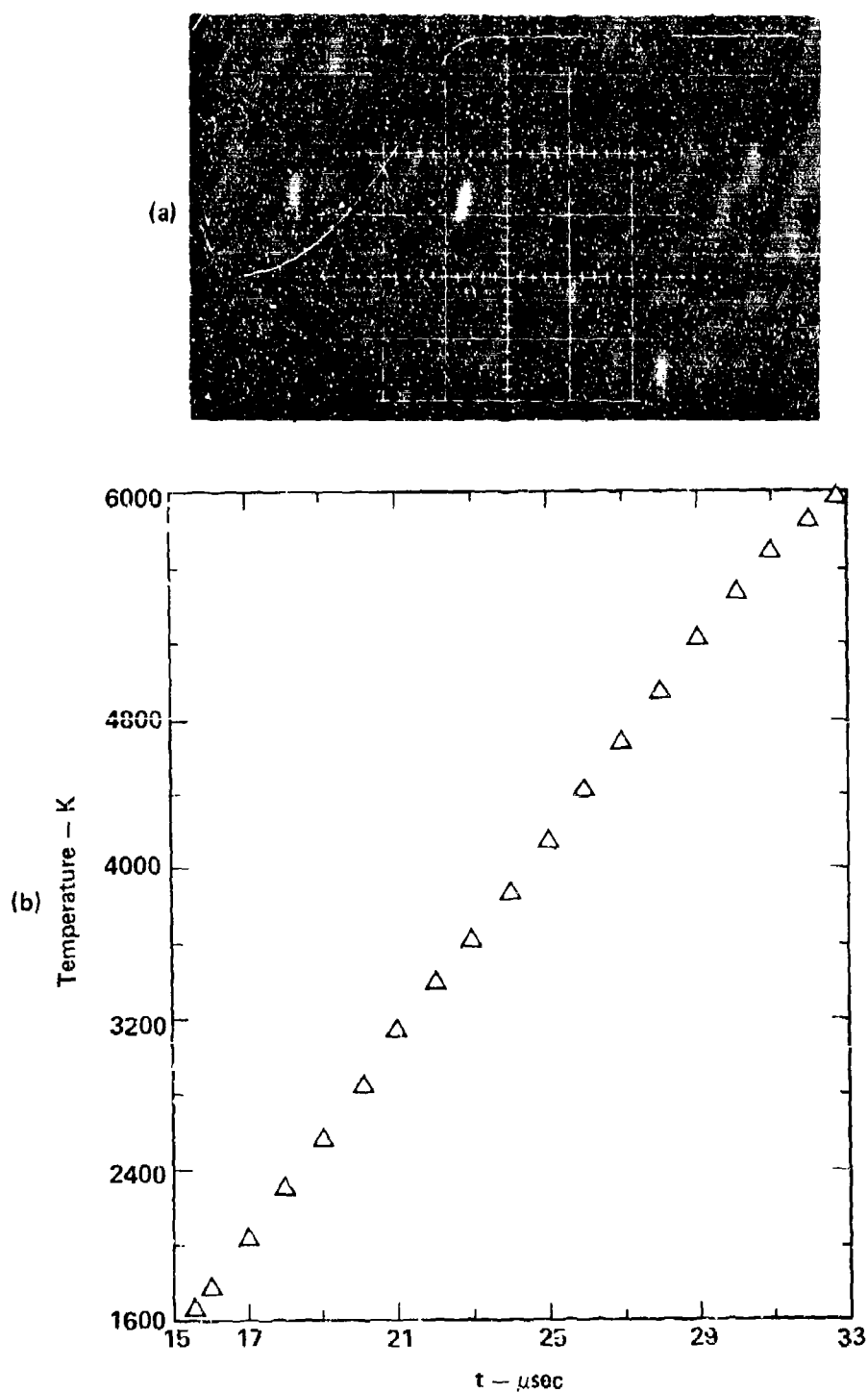


Fig. 8 Pyrometer Response Voltage and Resulting SCT Temperature for Lead at 0.3 GPa  
 (a) Pyrometer response voltage recorded in the 650 nm channel for lead at 0.3 GPa.  
 (1) and (2) are the noise signals from bankfire and crowbar, respectively. The scales  
 are log intensity (0.5 V/cm) vertical and 5  $\mu\text{s}/\text{cm}$  horizontal. (b) Temperature vs time  
 plot for the shot shown in (a).



A material satisfying this criterion is tantalum which melts at 3270 K producing a melting plateau in the data trace where the temperature does not increase during the time necessary to add the enthalpy of fusion.<sup>(23)</sup> Because the melting plateau provides such a convenient means of associating measured intensity with known temperature much has been done to extend the measurement capability below 2000-2500 K. Specifically the optics between the cell and the detectors was changed to redefine the exit aperture of the cell and present more sample radiation to the detectors. With the improved sensitivity it has been possible to discern melting plateaus for platinum ( $T_m = 2045$  K), Nb ( $T_m = 2741$  K), and uranium ( $T_m = 1406$  K). However, the lower temperature melting points of uranium and platinum have not proven useful for calibration purposes because of the large uncertainty in the measured intensities at such low temperatures. In addition the greater intensity associated with the higher temperatures frequently saturates the photodiodes making the high temperature readings unusable. Clearly, even with the logarithmic amplifier it is not possible to accurately measure the entire temperature range in a single experimental run.

Volume measurements are made with a high speed image converter streaking camera which produces a continuous record of the diameter of the expanding sample. The sample is back lighted with a one watt argon ion laser, the beam of which is sufficiently spread by diffraction to uniformly illuminate the entire 14 mm diameter aperture of the viewing port. This image is brought to a focus at the plane of a horizontal slit with a magnification of approximately ten to fifteen. An image of the slit is then relayed through a 10 nm width narrow band interference

filter to a second intermediate focus with a slight gain in magnification. The narrow band filter is centered at the laser frequency ( $\lambda = 5145\text{\AA}$ ) for the purpose of excluding the thermal radiation emanating from the sample. The streaking camera is focussed on this last image of the slit producing a continuous record of the image covering a 50 mm length of film in 100  $\mu\text{s}$ . The camera itself produces a demagnification so that the final overall magnification is about ten. Figure 9 is the streak photograph from a 0.2 GPa lead run accompanied by the expansion data reduced from that photo. Timing marks are generated every 1 or 2  $\mu\text{s}$  by switching a continuous wave HeNe laser with a Pockels cell and bringing the pulsed beam to a focus at the center of the slit image before the camera. The Pockels cell is driven by a high voltage oscillator whose frequency is measured with a high speed digital counter. Thus the time scale is known precisely in the streak photograph while the start of the sweep is determined relative to bank fire by monitoring the camera grid voltage on an oscilloscope. The accuracy of this technique will be discussed in the next chapter.

Whether a run is dedicated to enthalpy-volume or enthalpy-temperature measurements the second optical viewing port is used to obtain a late time photograph of the sample in order to confirm or deny the sample's equilibrium status. Early in the firing sequence a signal to a capacitive discharge unit controlled capacitor bank shorts the bank across flashlamps which optically pump an air cooled ruby rod. This pumping operation occurs on the time scale of hundreds of milliseconds in contrast to the tens of microseconds necessary for the rest of the experiment. The rod is placed in an optical resonator cavity with one mirror obscured by two polarizing elements, one of them a Pockels cell

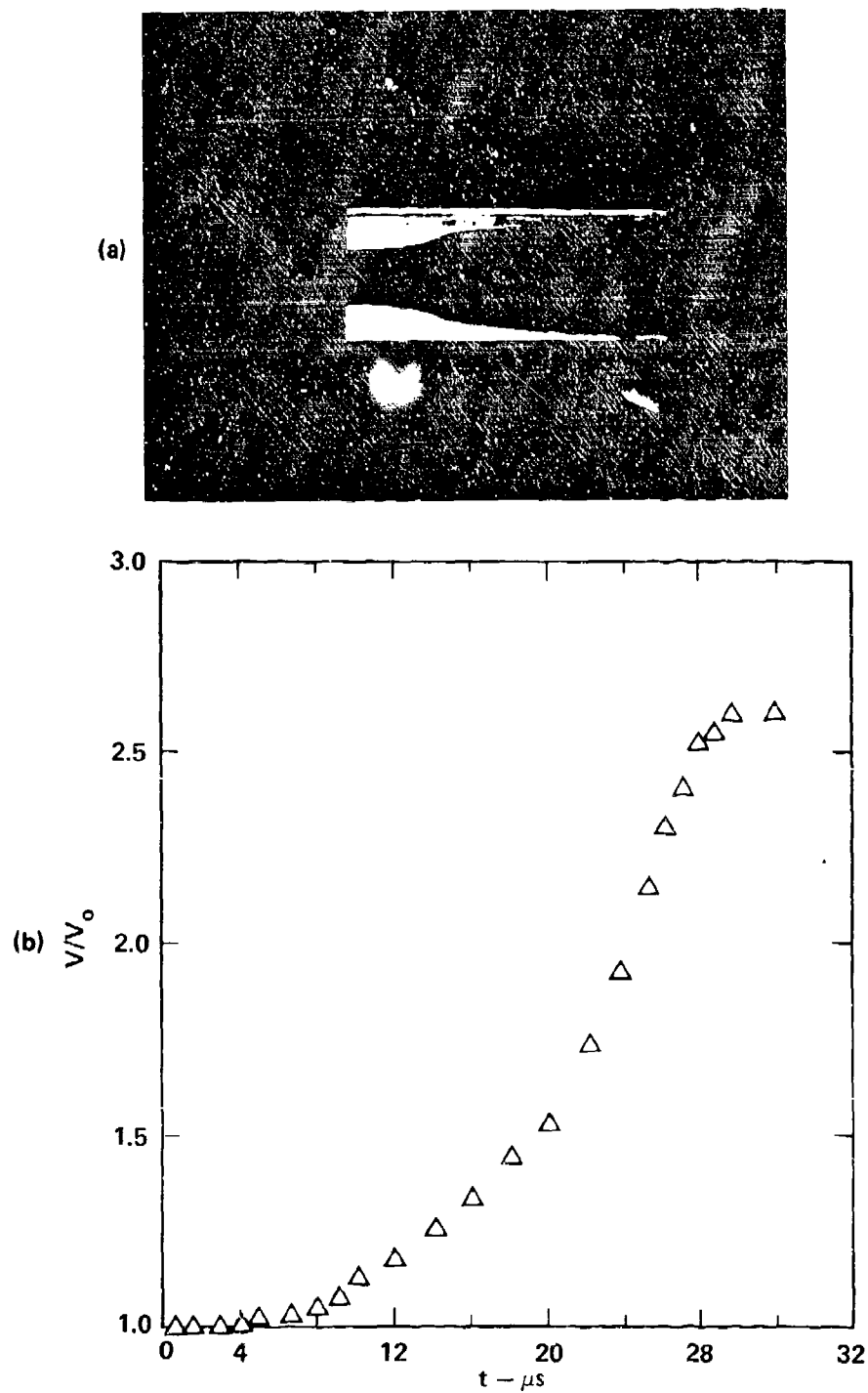


Fig. 9 Expansion of Lead at 0.2 GPa

Streak photograph of diameter vs time and resulting analyzed relative volume vs time data. (a) Streak photograph. Time marks in the center of the shadow of the wire are spaced by  $2.001 \mu\text{s}$ . (b) Analyzed data.

whose plane of polarization is at  $90^\circ$  to the other. From 5 to 10  $\mu$ s after the main bank voltage has been crowbarred (see Figure 6) a separate high voltage pulse is impressed across the Pockels cell rotating its plane of polarization allowing the fully pumped ruby rod to lase. This precisely timed pulse of laser light ( $\lambda = 6941\text{\AA}$ ) is transmitted through a beam expanding telescope, into and through the pressure cell, through intermediate optics into a framing camera. As with the streak photography it is necessary to discriminate against sample thermal radiation by placing a narrow band filter between relay lenses (where the imaging light is coaxial). In addition the intensity of the ruby light is controlled by placing two black glass flats used as first surface turning mirrors in the optical train and by further attenuating with neutral density filters.

Two examples of the resulting picture are shown in Figure 10, the first illustrating lead at 0.2 GPa expanded stably to 2.7 times normal volume. The second picture is of lead under the same experimental conditions as the sample in the first picture except for a pressure of 0.1 GPa. The lead at 0.1 GPa has been pushed beyond stable equilibrium conditions, evidently reaching to and beyond the volume at the liquid-vapor two phase boundary (see Figure 2). Data from experimental runs in which the sample exhibits this late time behavior are usually disregarded.

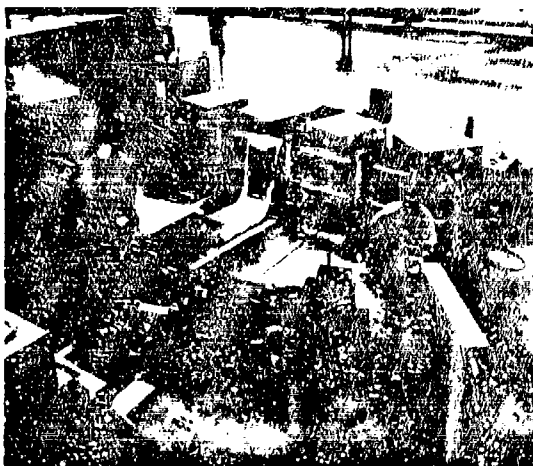
The major components of the experiment including the diagnostic apparatus are most easily envisioned through the photographs of Figure 11. Major components in picture (1) are the cell itself, the main bank capacitors, the hut housing the Q-switched ruby laser, and the framing camera for the ruby snapshot. Picture (2) displays the image of the



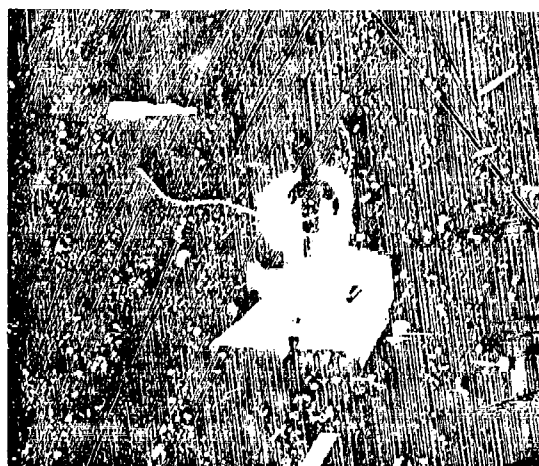
Unstable liquid lead at 0.1 GPa



Fig. 10 Liquid Lead Wire at 0.2 GPa and 0.1 GPa  
 Ruby laser photographs of lead wires in dense argon. (a) Stable expansion to  $V/V_0 = 2.61$  at 0.2 GPa. (b) Unstable expansion with same energy deposition as (a) but at 0.1 GPa.



(1) Pictured in front from left to right are the pressure cell, the framing camera used for the ruby laser snapshot, and the argon ion laser used to back light the streak photography. Behind are the four modules of six capacitors each.



(2) Image of the sample cell upon the adjustable slit in front of the fibre optics bundle.



(3) The main control panel showing pressurization system controls on the left and electronics controls on the right.



(4) Part of the oscilloscopes used in recording data.

Fig. 11 The Isobaric Expansion Experiment

Photographs of various components of the IEX.

sample being brought to focus on the end of the trifurcating fibre optic. Picture (3) shows the main experimental control panel on the right and the pressurization panel on the left. The data recording oscilloscopes are in picture (4). To enhance reliability current, voltage, and pyrometer response voltages are measured redundantly. Data reduction considerations are discussed in the following chapter.

### Technical Concepts and Experimental Limitations

The basic contention for the validity of the experimental measurements discussed in this work is that it is possible through resistive heating to bring a metallic sample to an equilibrium state, and to know the state parameters by measuring the pressure of the environment, the amount of electrical energy added, and the thermal radiation of the sample. In this section it will be established through elementary physical arguments that such a claim is valid within certain constraints on the characteristics of the material, the size of the sample, and the duration of the experiment.

It can be shown that the electrical energy added per unit mass per unit time is  $j^2 \rho_e / \rho_m$  where  $j$  is the current density,  $\rho_e$  is the electrical resistivity, and  $\rho_m$  is the mass density. In this experiment  $j$ ,  $\rho_e$  and  $\rho_m$  are all functions of time so the total energy added to the sample per unit mass is the integral of the above expression. For reasons to be discussed it is best to deposit the energy with as low a current density as possible which, in turn, puts bounds upon  $\rho_e$ . In practice satisfactory data has been taken on materials with initial resistivities as low as 0.05-0.07  $\mu\Omega\text{m}$  (AuCu) and as high as 13.75  $\mu\Omega\text{m}$  (carbon). The upper limit, although not firmly established, is governed

by practical considerations of cell design. Should the sample resistance grow very large it would dominate resistors  $R_1$  and  $R_2$  (see Figure 6) placing a large part of the bank voltage across the sample. This voltage appears between the current carrying lead shown in Figs. 3 and 4 and the anvil body, a space of 0.35 mm filled with pyrophyllite and epoxy. At high sample resistivities the voltage frequently breaks this insulating barrier shunting the current around the sample. Various materials have been tried for this crucial seal, but better insulating arrangements have proven to be less pressure tight, allowing the cell gas to diffuse out.

The lower limit of sample resistivity has not been established experimentally. However, small resistivities make uniform energy deposition more difficult by slowing the diffusion of the current density to the center of the sample. In addition small resistivities make large currents necessary to achieve the large enthalpies required to investigate the lower density liquid states, and these large currents lead more readily to the growth of instabilities. The instability question will be considered first.

In a pinched plasma column slight departures from cylindrical symmetry grow unstably.<sup>(24)</sup> Such an instability is the magnetohydrodynamic necking in the linear pinch whose characteristic growth time is given by  $a/V_a$ , where  $a$  is the wire radius and  $V_a$  is the Alfvén velocity based on the magnetic field at the wire surface.<sup>(12)</sup>  $V_a = \frac{B}{[\mu_0 \rho]^{1/2}}$  and  $B = \mu_0 I / 2\pi a$  yielding an instability growth time of  $T_c = \frac{2\pi}{I} \left[ \frac{\rho e}{\mu_0} \right]^{1/2}$ .  $T_c$  for lead near melt with a current of 30 ka is about 5  $\mu$ s. Experimental runs made on lead demonstrated it to be stable as much as 60  $\mu$ s past melt which could mean that the sample was very symmetrical and remained so during expansion.



Nevertheless, the possibility of significant MHD instability on the time scale of the experiment makes low current energy deposition preferable to higher current heating.

More immediate resistivity considerations center upon the need to achieve a uniform energy density throughout the sample. A perfectly conducting wire, of course, would exclude all fields from its interior carrying the current in an infinitesimally thin region near the surface. In less perfect conductors this situation applies initially, but radially inward diffusion of the current density eventually causes direct resistive heating of the entire wire. For a time then, the energy deposition is not uniform throughout the wire and it is necessary to determine how long this non-equilibrium condition persists.

In the absence of a uniform current density equilibrium could only be reached through heat transport. Heat conduction, should it prove significant on the time scale of the experiment, could eventually lead to a uniform temperature in the sample. The Einstein diffusion relation  $T = \langle x^2 \rangle / 2D$  provides a straightforward check on the thermal communication length, or conversely minimum times necessary to establish thermal equilibrium.<sup>(25)</sup>  $\langle x^2 \rangle$  is an average squared displacement which is chosen as the initial wire radius 0.5 mm, and  $D$  is the self diffusion coefficient,  $K/C_p \rho_m$ .  $C_p$ , the constant pressure heat capacity, is measured to be 3.61 R and  $\rho_m \approx 9.1 \times 10^3 \text{ kg/m}^3$  for liquid lead at 2500 K (see Chapter 4).  $K$ , the thermal conductivity is not measured but can be deduced from the electrical conductivity through the Wiedemann-Franz law,  $K = L\sigma T$ .<sup>(26)</sup>  $L$ , the Lorenz number, is assumed to be  $2.6 \times 10^{-8} \text{ watt-ohms/K}^2$  and  $\sigma$  is measured to be  $6.25 \times 10^5 \text{ ohms/m}$  yielding a value for  $K$  of 40.63 watts/m-K. The self diffusion

coefficient is then  $3.1 \times 10^{-5} \text{ m}^2/\text{sec}$  and a characteristic time for heat transport between the outer edge and the center of the wire is 4 ms, which is one and half orders of magnitude too large for heat conduction to play a significant role in establishing equilibrium.

Clearly then, valid IEX equation of state measurements are dependent upon the rapid establishment of a uniform current density. Qualitatively, a positive change of resistivity with temperature would tend to damp out slight temperature inhomogeneities by shunting more current to the cooler less resistive areas. It will be shown quantitatively that a positive temperature derivative plays a strong role in achieving uniform current density by driving the diffusion of the magnetic flux to the center of the wire. Of the materials studied to this point only carbon has exhibited a negative resistivity derivative ( $\partial \rho_e / \partial T$ ) and this occurred at resistivities high enough to ensure that the diffusion of the current density was essentially instantaneous. Evidence of sample destruction caused by an accelerating shunting of the current to a non uniformly hot region was observed only rarely.

The diffusion of the current density can be calculated through application of Maxwell's equations in conjunction with Ohm's law. <sup>(23)</sup> If the displacement current is assumed negligible compared with the current density and the magnetic permeability is constant in space and time  $\nabla \times \mathbf{B} = \mu_0 \vec{J}$  and  $\nabla \times \rho_e \vec{J} = -\partial \mathbf{B} / \partial t$ , where  $\rho_e$  is again the resistivity. Combination of these two expressions implies  $\nabla \times \nabla \times \rho_e \vec{J} = -\mu_0 \partial / \partial t \vec{J}$ . If the current density is only in the axial direction and is not a function of the long dimension of the sample the cylindrical symmetry allows the expression to be reduced to:

$$\frac{1}{\mu_0 r} \frac{\partial}{\partial r} \left[ r \frac{\partial}{\partial r} (\rho_e J) \right] = \frac{\partial J}{\partial t} \quad (2-1)$$

where  $J$  is now the magnitude of the current density in the axial direction. For a spatially independent resistivity the usual separation of variables,  $J(r, t) = j(r) e^{i\omega t}$ , yields:

$$\frac{\partial^2 J}{\partial r^2} + \frac{1}{r} \frac{\partial J}{\partial r} - \frac{i}{\delta^2} J = 0 \quad (2-2)$$

where  $\delta = (\mu_0 \omega \rho_e)^{-1/2}$  is just the classical skin depth in SI units. Using the initial lead resistivity of  $0.206 \times 10^{-6} \Omega\text{-m}$  and assuming the dominant Fourier component of the current pulse to have a period of 10  $\mu\text{s}$ , the classical skin depth has a value of about 0.5 mm. For gold-copper the initial resistivity is  $0.073 \times 10^{-6} \Omega\text{-m}$  and skin depth is about 0.3 mm. Both numbers are on the order of the sample radius which, of course, is a primary consideration in choosing the sample size.

Because  $\rho_e$  is a function of the temperature and the temperature is at least a function of position it is necessary to numerically integrate Eq. (2-1) to calculate current density and thus the energy deposited as a function of wire radius. The ratio of the energy density on the surface to that at the center is plotted for both lead and gold-copper in Figure 12. In each case the energy distribution is found to be essentially uniform before the pyrometry begins to respond and before there is significant expansion of the sample.

Though it appears feasible to add energy uniformly to the sample through resistive heating, other points bear consideration before the

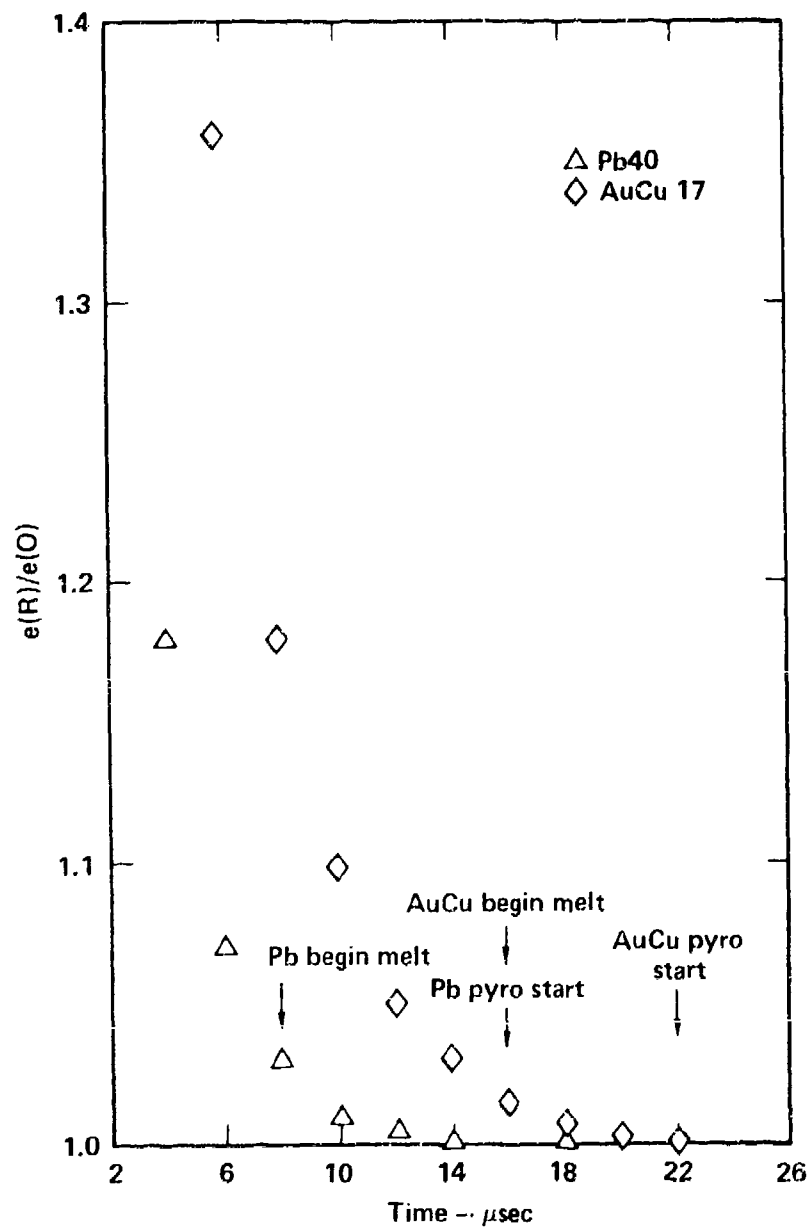


Fig. 12 Skin Effect Calculation in Lead and Gold-Copper  
Results of current density diffusion calculation showing the ratio of the energy deposited at the center of the wire as a function of time. Energy deposition is shown to be uniform across the wire by the time the pyrometers begin to respond.

sample can be assumed to be in equilibrium. It has already been argued that the sample boundary experiences a constant pressure independent of its state of expansion. In order for this expansion to occur, however, the pressure interior to the sample must exceed the gas pressure by some finite amount. To maintain equilibrium the boundary condition must be communicated to the interior on a time scale short relative to the time necessary for a significant volume expansion. The vehicle of communication is a pressure relief wave which travels from the surface inward at the bulk sound speed, and a representative time is the time necessary for this relief wave to reach the center of the sample. The sound speed is inversely proportional to the square root of the density times the compressibility,  $U_s = [1/\rho_m K_s]^{1/2}$ . Lead, being the most compressible of the materials of this study, should give a worst case number. Soft sphere calculations based on the data in Chapter 4 and measured sound speeds near melt at 0.1 MPa show  $U_s$  to vary from a high of 1.8 mm/ $\mu$ s at  $T = 600$  K to 1.1 mm/ $\mu$ s near  $T = 4000$  K. Direct thermodynamic calculations using the data of Chapter 4 show  $U_s$  to be very close to 1 mm/ $\mu$ s over a temperature range from 3000 K to 6000 K. This latter figure yields a relief wave transit time of 0.5  $\mu$ s, certainly short enough to make the assumption of a uniform pressure valid.

The contention that the change in enthalpy of the sample is directly the electrical energy added is true only if heat losses are negligible during the time of the experiment. Early concern over possible index of refraction changes due to sample caused heating of the inert gas led to the choice of x-ray radiographs rather than optical techniques for the density measurement.<sup>(10)</sup> Subsequently it was shown that for times of 100  $\mu$ s or less the characteristic diffusion length in dense argon is

about  $3 \times 10^{-3}$  mm. (12) This calculation derives from the Einstein self diffusion relation previously used with  $K = 70 \times 10^{-3}$  watts/m-K and  $\rho_m C_p \approx 10^6$  j/m<sup>3</sup> K. On the time scales of interest there is negligible thermal conduction beyond the surface of the sample and consequently very little optical aberration.

A dual and somewhat antagonistic requirement is placed on the radiative energy transfer from the sample. Thermal radiation has to be strong enough to be reliably recorded by the pyrometers yet not significant when compared to the electrical energy being added. Typical electrical energies added are from 0.7 to 2.0 MJ/kgm over a time span of 30 to 50  $\mu$ s. The rate of thermal energy emission is given by the Stefan-Boltzmann expression for a gray body,  $dE/dt = \epsilon \sigma T^4$ . Estimates of the emissivity of lead (see Chapter 4) over a temperature range of 2000-6000 K are 0.20-0.25 with some wavelength dependence. Reasoning that the most energy is emitted at the highest temperature for which the density is low a temperature of 4500 K for a density of  $5.7 \times 10^3$  kgm/m<sup>3</sup> over a time of 30  $\mu$ s will give an energy loss representative of a typical experiment on lead. Under these assumptions total radiated energy is  $8.65 \times 10^{-5}$  MJ/kgm and is far less than the error associated with the enthalpy measurement. A worst case calculation might involve a material heated to 10,000 K over a time span of 60  $\mu$ s, with a hypothetical density half that of the expanded lead, and an emissivity of approximately 0.5. Even with the unrealistic assumption that the sample remain at peak temperature for 60  $\mu$ s total radiated energy would be only  $1.71 \times 10^{-3}$  MJ/kgm, again within the accuracy of the enthalpy measurement. It is evident, therefore, that samples whose diameter is on

the order of 1 mm lose only insignificant energy radiatively for total experimental times of 100  $\mu$ s or less and temperatures less than 10,000 K.

Irregularities in the surface of the sample could give rise to the growth of hydrodynamic instabilities driven by the surface tension of the liquid. If the surface deformation is small these instabilities propagate at a velocity given by  $V = [2\pi\gamma/\rho_m\lambda]^{1/2}$  where  $\gamma$  is the surface tension,  $\rho_m$  is the liquid density, and  $\lambda$  is the scale size of the instability.<sup>(27)</sup> A calculation of this velocity in liquid lead will demonstrate the significance of the effect. Care in the preparation and handling of the lead samples conservatively limits the size of surface irregularities to 10  $\mu$ m or less. For calculational purposes consider the model deformation to be a dome (or pit) whose radius is 5  $\mu$ m. A characteristic time for the growth of the instability might be the time necessary for the deformation to move half the length of the sample or about 10 mm. The surface tension of lead at 1000 K is approximately 0.4 nt/m and the density is  $10^4$  kgm/m<sup>3</sup>.<sup>(28)</sup> The propagation velocity is then 7 m/sec and the instability growth time is about 1500  $\mu$ s, a time longer than other time constraints.

A final consideration in defining the parameter range accessible to a successful experiment is perhaps the most obvious, the influence of gravity. Throughout much of the duration of an experimental run the sample is a free standing liquid column whose motion is impeded only by viscous forces. An estimate of the effect of gravity can be made by computing the displacement due to gravitational acceleration in the space of 100  $\mu$ s, neglecting viscous retarding forces. This purposely

pessimistic estimate is about 5  $\mu\text{m}$  which is on the order of 0.1% of the length of the sample and is insignificant to the experiment.

It has been established that it is indeed possible to resistively heat a sample to a succession of equilibrium states if the heating time is longer than about 5-10  $\mu\text{s}$ , the time necessary for flux diffusion to equilibrate the energy density, and if large changes in state do not occur in less than 0.5  $\mu\text{s}$ , the time required for the acoustical equilibration of the pressure. Heat transport processes do not become significant to the state of the sample as a whole for times less than 100  $\mu\text{s}$ . The upper limit on experimental times and temperatures less than 10,000 K are imposed by the growth rate of magnetohydrodynamic instabilities, modeled as the Alven wave velocity, which leads to an instability growth time of 5-10  $\mu\text{s}$ . This time constraint,  $r/V_a = [\rho_m/\mu_0]^{1/2} 2/j$ , is about an order of magnitude shorter than times routinely reached with no evidence of instability. The conclusion is that experimental times are constrained to be less than 70-100  $\mu\text{s}$  by the possible growth of MHD instabilities which are not initiated until well after bankfire. The disparity between the calculated and actual time limits is added evidence that the sample expands uniformly, maintaining a smooth symmetrical surface until late time.

The maximum enthalpy of the state that can be reached with the experiment is the time integral of the deposition rate,  $\Delta H_{\text{max}} = \int_0^t j^2 \rho_e/\rho_m dt$ . If the time dependence of all parameters involved is ignored  $\Delta H_{\text{max}}$  can be estimated as:

$$j^2 \frac{\rho_e}{\rho_m} t = j \frac{2\rho_e 10}{[\mu_0 \rho_m]^{1/2}} \quad (2-3)$$



where 10 is the adjustment factor contributed by experimental evidence. It should be noted that neither the characteristic instability time nor the maximum attainable enthalpy is a function of sample dimension. The sample diameter is limited to less than 1 to 2 mm by the times required to diffuse the field and equilibrate the pressure. Minimum sample diameter is limited by the difficulty in handling thin wires and, in the extreme, by radiative heat losses.

The validity of the temperature measurement requires special examination because it depends not upon the bulk properties of the sample but on the conditions at the surface. Fields associated with the thermal radiation are representative of the material only within a skin depth of the surface. To illustrate the considerations important to the pyrometry consider a rectangular cell of 6000 K liquid lead of unit area and one skin depth deep. At 6000 K the blackbody peak is at a wavelength of approximately 5000Å, and the characteristic skin depth for this radiation is given by  $\delta = [\mu_0 \omega \sigma_e]^{-1/2} = 384\text{Å}$ , where a measured conductivity of  $1.43 \times 10^5 \text{ mhm}^{-1}$  has been used. The pertinent issue is whether the thermophysical conditions prevailing in this element of material at the surface are those of the sample as a whole, or have been significantly altered because of surface energy losses. A crude estimate can be made by assuming that because of the short times involved conduction is not important and that energy may only be added to the cell through direct electrical heating and is lost by radiation. Using a measured density of  $5.68 \text{ kgm/m}^3$  and a measured enthalpy addition rate of  $4.7 \times 10^4 \text{ MJ/kgm-sec}$  the rate at which energy is being added to the cell is  $1.33 \times 10^3 \text{ J/sec}$ . The energy loss rate, using an estimated emissivity of 0.25, is found to be  $1.84 \times 10^3 \text{ J/sec}$ . In the absence of conduction the

surface element loses energy at a rate faster than it is gained and the temperature is not indicative of the amount of electrical energy that has been added. The error in the temperature can be calculated by comparing the total electrical energy added to the slab to the total energy radiated during the course of the experiment. The total energy added is  $3.83 \times 10^{-2}$  joules and the radiated energy is calculated using a measured temperature-time relationship to be  $7.94 \times 10^{-3}$  joules. For the spectral window of the pyrometer used in measuring the temperature the radiated energy varies as approximately  $T^5$ . Therefore the error in temperature for the calculated error in energy is given by  $\Delta T/T = 1/4 \Delta E/E = 5\%$ . While this does not appear to be a serious error the implication that the surface layer cannot be heated above a temperature somewhat less than 6000 K because of radiative losses is wrong, and is a direct result of the simplifying assumption that all radiated energy is drawn from within one skin depth of the surface.

The fact that blackbody spectra characteristic of temperatures much greater than 6000 K have been observed indicates that the radiative losses of the surface are being resupplied by the conduction of energy from the interior of the sample. In order to make an estimate of the potential heat conduction rate consider the temperature deficit calculated in the last paragraph to appear across the skin depth. In this case the heat conduction rate into the cell is  $q_1 = K_1 A \left. \frac{dT}{dx} \right|_1$  and the thermal conductivity can again be calculated from the Wiedemann-Franz law,  $K_1 = L\sigma T = 22 \text{ watts/m-K}$ . The rate into the surface slab is then  $1.72 \times 10^7 \text{ joules/sec}$ . Similarly the conduction rate out of the slab into the gas can be calculated from  $q_2 = K_2 A \left. \frac{dT}{dx} \right|_2$  where  $K_2$  is the  $70 \times 10^{-3} \text{ watts/m-K}$  used previously and the gradient is

estimated as a linear change from 5700 K to 300 K over the thermal diffusion length in  $33 \mu\text{s}$  (time necessary to reach an indicated 6000 K). With these assumptions  $q_2 = 1.76 \times 10^4$  joules/ sec. The energy balance in the surface slab is controlled by the heat conducted from the sample interior which raises the temperature of the surface element reducing  $dT/dx|_1$  until equilibrium is achieved.

It is possible with the approximate discussion of the above paragraphs to argue that the temperature at the surface of the lead sample is within 1% of the bulk temperature of the sample at 6000 K. However, without a dynamic heat transfer calculation on the entire wire, it is not possible to know exactly the deviation of the surface temperature from that of the interior nor to predict the temperature past which the surface element cannot be heated. Complicating the calculation is the fact that the thermal conductivities involved are a function of temperature. It should also be noted that the skin depth and thus the width of the surface element from which energy is radiated is a function of wavelength, and that the significant spectral content of the blackbody radiation varies strongly as a function of temperature. A valid calculation would necessarily include specific knowledge of the surface roughness. Skin depths are on the order of 500A while late time streak photography indicates surface irregularities as large as  $10 \mu\text{m}$ . Finally it is unclear whether linear heat transport analysis is applicable to cases involving the steep temperature gradients inherent in the short time scales of this experiment. In the absence of such a detailed heat transfer calculation the inherent inaccuracy of the measure temperatures cannot be reduced below 1% for the data reported in Chapter 4.

### 3. DATA ANALYSIS AND ACCURACY

As described in the previous chapter each experimental run produces a wealth of data for the most part in the form of photographed oscilloscope traces. Those parameters recorded as a function of time are the current through the sample, the voltage drop across a measured portion of the sample, the voltage response of the photodiodes, and the image of a sample diameter. A common time reference point is established on the many independently recorded data by the electrical noise spike recorded when the spark gap is fired closing the circuit to the main capacitor bank. Each analog trace is digitized with respect to that reference point by reading the film on a Grant Model 2000 film reader controlled by a Digital Equipment Corporation PDP8/e computer. The x-y stage of the film reader enables a particular point on the film to be located to the nearest micron. A film is "read" by locating a succession of arbitrarily spaced points on the trace, and, at each location, pressing a foot pedal which causes the x and y positions of that point to be punched on a computer card. A typical trace is adequately represented by 50-100 points, which form a table of raw data as a function of time.

This chapter is a discussion of the calculations necessary to transform these digitized data tables into accurate thermophysical properties. Most of the calculations described were performed on the computer using a code originally developed by Henry<sup>(10)</sup> but extensively modified by Gathers,<sup>(29)</sup> and a series of codes developed on the current project. The primary properties emerging from these analyses are the enthalpy, density, temperature, and resistivity. Invoking the equilibrium arguments advanced in the last chapter pressure

is read directly from a gas pressure gauge and requires no analysis. The enthalpy determination has received much prior attention<sup>(10,11)</sup> and will be addressed only briefly. Density and resistivity are straightforward once the credibility of the measurements has been established. However, the determination of a true temperature based upon multi-channel intensity data is involved and will be discussed in detail. Estimates of the measurement precision and the overall accuracy will be made.

### Enthalpy

Determination of the enthalpy remains essentially as described by Henry, et al,<sup>(11)</sup> and is calculated from the experimental current and voltage according to the following expression:

$$\Delta H = H(T) - H(298) = \int_0^{t_p} I(t) V_r(t) dt \quad (3-1)$$

where  $V_r$  refers to the voltage drop due to the passive impedance of that part of the sample between the voltage probes. The enthalpy calculated is thus the amount of electrical energy added to the mass of the interprobe sample, and that mass is known from an Archimedian measurement of the initial density plus a comparator measurement of the initial diameter and probe separation.

Current is determined from the voltage response of the Pearson probe which is calibrated against an N.B.S. standard to be accurate to within 0.1% over a frequency range of 12-100 kHz. For each of the experimental runs the oscilloscope horizontal and vertical amplifiers are calibrated with a precisely adjusted signal generator in conjunction with a time

mark generator. Calibration signals for each scope are read on the Grant film reader and are used to convert film distances to voltages. The primary source of error in this procedure derives from scope non-linearity (averaged out in the calibration procedure) and imprecision in finding the center of scope traces and timing marks. Errors in probe calibration are systematic while reading errors are random and are greatly reduced by the redundancy of calibration and data measurements.

In order to correlate  $I(t)$  and  $V_p(t)$ , which are read at arbitrary times with the film reader, it is necessary to reconstruct continuous functions from the tables of digitized data. This is done with overlapping piecewise continuous quadratic fits, i.e. quadratic fits are made for successive sets of three data points with the first points in adjacent sets displaced by one point from each other. The first point in the second set is the second point in the first set, etc. This means that each region of the time axis except for the ends is covered by two quadratic fits and a parameter value is taken as the average of the two values calculated with the two quadratic functions overlapping in a given time region. This interpolation scheme has the effect of reducing random error but also destroys some of the features of the trace.

The interprobe voltage includes both inductive and resistive contributions and may be expressed as:

$$V_m(t) = I(t)R(t) + L_T(t) [dI(t)/dt] + I(t) [dL_T(t)/dt] \quad (3-2)$$

where the first term is  $V_R(t)$  required in Eq. (3-1).  $L_T(t)$ , the total inductance, includes the self inductance of the sample  $L(t)$ , and the inductance due to the interaction of sample current generated fields with the voltage measuring circuit. The latter quantity, labelled here  $M(t)$ , is reduced by placing the voltage probes on opposite sides of the sample but is apparently still a sensitive function of the exact positions of various electrical elements in the circuit and varies from shot to shot.  $L(t)$  is calculated using the following expression for a coaxial line: (30)

$$L(t) \approx \frac{\mu_2}{2\pi} \left[ \ln \frac{a_2}{a_1} + \frac{1}{\sqrt{4\pi}} \frac{1}{\mu_2} \sqrt{\frac{\mu_1 \rho_1}{v}} \left( \frac{1}{a_1} + \frac{1}{a_2} \right) \right] \quad (3-3)$$

where the subscripts 1 and 2 refer to the inner (sample) and outer (ground cap) conductors, respectively.  $\mu_1$  and  $\mu_2$  are considered equal and equal to the permittivity of free space while  $\rho_1$  is the measured resistivity of the sample.  $v$  is a frequency characteristic of the current pulse through the sample.  $L(t)$  is a function of time through time variation of  $a_1$ , the sample radius, and  $\rho_1$  the resistivity.

In practice for those runs in which  $a_1$  is measured the self inductance is calculated, and  $M(t)$  is then chosen to be an additional constant value that might be necessary to eliminate obvious inductive spikes in the voltage record. For those runs in which a volume measurement is not made  $L_t(t)$  is chosen as that constant inductance which best eliminates inductive spikes in the voltage record. Of course this eliminates the third term in Eq. (3-2) from the calculation. In

either case  $V_R(t)$  is that measured voltage remaining after the inductive correction is subtracted.

At early times the inductive component of the measured voltage is large compared with the resistive part, and any uncertainty in making the inductive correction is translated into a significant error in the computed enthalpy. At later times the uncertainty in the inductive contribution shrinks markedly in significance because the resistive voltage dominates completely for large slowly varying currents and high resistivities. Therefore, the overall uncertainty in the calculated enthalpy may be as much as 15% from 1-5  $\mu\text{sec}$  into the experiment but falls to 2% for the experiment as a whole. The possibility of large early time enthalpy uncertainties has a noticeable effect only on the temperature calibration procedure to be discussed in a later section.

#### Volume (Density) Measurement

The volume measurement discussed in Chapter 2 and illustrated in Figure 9 rests on the assumption that the expansion of the sample is in the radial direction only, and thus any change in volume may be known by monitoring the sample diameter. The procedure for establishing the time dependence of the sample diameter involves measuring pre-shot and data streak photographs, and an additional photograph monitoring the gating voltage in the image converter camera. This last photograph shows the time relationship between bank fire which is evidenced by a noise spike, and the point at which the streak photograph begins. The pre-shot streak photograph calibrates the faithfulness of the camera in reproducing a constant diameter image as a function of time. The size of the photographed image may vary by as much as 2% for a 100  $\mu\text{s}$  record.



In analyzing each streak photograph the positions of both edges of the image are reduced to sets of x-y coordinates as was done with the current and voltage traces. These edge locations are measured with respect to the film position at which the streak record begins. The exact position of the streak record beginning is somewhat indistinct and therefore uncertain to 500  $\mu\text{m}$  or less, introducing as much as a 1  $\mu\text{s}$  error into the time base. Readings of the image edges are made at arbitrary positions with respect to the common base point. Cubic splines are used to form continuous functions of edge position versus distance from camera start. The image diameter can then be calculated by subtracting the positions of the left and right edges for common film distances from the base point. Because sample heating does not begin until after camera start the early part of the record gives the initial diameter of the sample, and the relative volume can be calculated as the squared ratio of the diameter to the initial diameter.

The time scale is established in two steps. First, the time between the camera start base point and bankfire is found and then the time versus distance relationship for the streak photograph is computed. The latter operation is done by measuring the positions of the time marks on the photograph and again using cubic splines to form a continuous function of time versus distance. Since the volume ratio has been computed as a function of film distance the time versus distance spline fit can be used to find volume ratio as a function of time from camera start. These calculations are carried out for both the pre-shot streak record and the data record producing  $V/V_0(t)|_0$  and  $V/V_0(t)|_D$ . The actual sample volume ratio calculated as a function of time and corrected for camera non-linearities in two directions is:

$$V/V_0(t)|_{\text{true}} = [V/V_0(t)|_D] / [V/V_0(t)|_0] \quad (3-4)$$

Error in the measured volume ratio derives from uncertainties in locating the two edges of the photographed shadow and uncertainties in determining an accurate time scale. Timing errors can be further divided into a systematic part caused by an incorrectly determined streak start time, and a random part caused by errors in reading the positions of the timing marks. The possible start time error has already been identified as corresponding to a film distance of less than 500  $\mu\text{m}$  while the timing mark position is accurate to within 50  $\mu\text{m}$ . For a typical photograph 1 mm of film corresponds to 2  $\mu\text{s}$ , meaning the confidence interval for the time axis is  $\pm 1 \mu\text{s}$ . The absolute nature of this error makes it significant for the initial stages of a run but of diminishing importance at later times.

At least three factors contribute to problems in locating the shadow edge exactly. These are diffraction effects, instrument resolution limits, and irregularities in the surface of the sample itself. Relatively elementary considerations indicate the last of these is the limiting factor in volume accuracy.

The sample is a thin wire bathed in monochromatic essentially collimated light whose shadow is brought to focus on the photocathode of the streaking camera. Because the diameter of the wire is large compared to the wavelength of the illuminating radiation the diffraction at each edge can be considered independently of the other. Consider a straight edge a distance  $a$  from a light source whose shadow falls on a plane a distance  $b$  from the edge. The first diffraction intensity maximum falls

at a distance from the edge of the geometrical shadow given by  $x = \left( \frac{b(a+b)}{a} \lambda \right)^{1/2}$ . (31) Were no optical elements present between the source and the sample and between the sample and the viewing plane  $a$  and  $b$  would be comparable and on the order of 3 or 4 meters each. In this case with  $\lambda = 0.5145 \times 10^{-6}$  m the first intensity maximum would be displaced from the edge of the geometrical shadow by 2 mm making the precise location of the edge impossible. In practice diffraction is taken care of empirically by the introduction of lenses and mirrors between the sample and the image plane sufficient to cancel any diffraction effects. The intervening optical elements have the effect of reducing  $b$  so that  $a$  is large by comparison and  $x \approx (b\lambda)^{1/2}$ . The optical elements are positioned so that a desirable magnification is achieved and observed diffraction patterns are completely eliminated.

Instrument resolution is another possible source of uncertainty in determining the exact position of the sample edge as a function of time. In taking the streak data the shadow of the sample is brought into sharp focus at the plane of the slit with a magnification of approximately 10. The slit width is adjusted to 0.5 mm and the image of the slit with the shadow of the sample is relayed to the focal plane of the camera with essentially no further change in magnification. During a typical experimental run the slit image is swept across the film plane at 0.5 mm/ $\mu$ s. As a worst case example a lead sample may go through a factor of four change of volume in 40  $\mu$ s causing the each edge of the shadow image to advance 5 mm in 40  $\mu$ s (0.125 mm/ $\mu$ s). Each point on the film outside the geometric shadow receives 1  $\mu$ s of illumination during which time the radius of the shadow grows by 0.125 mm. Assume the intensity of the backlighting, the response of the photocathode, and the sensitivity of

the film are such that a point on the film requires  $0.5 \mu\text{s}$  of exposure to become fully saturated. In this case each point on the image edge will define a radius greater than it should be by  $0.063 \text{ nm}$  and the deduced radius of the sample will be in error by  $0.0063 \text{ mm}$  which is a percentage error ranging between 1.2% and 0.6%. The time requirement for film saturation is actually somewhat less than  $0.5 \mu\text{s}$  so the 0.6% to 1.2% error is perhaps conservative.

A further consideration in determining the edge of the shadow image is possible optical distortion that might be caused by the growth of a diffusional boundary layer. Again using the Einstein diffusion relationship and the high pressure argon transport coefficients given in Chapter 2 with an experimental time of  $50 \mu\text{s}$  the diffusion length is  $2.4 \times 10^{-3} \text{ mm}$ . Depending on the index of refraction of the boundary layer this should also make the radius of the sample appear larger than its actual size.

A final phenomenon having a potentially deleterious effect on the accuracy of the radius measurement is the roughness of the surface of the sample. The initial sample diameter is measured to be uniform within less than 1% which is equivalent to an absolute non-uniformity in the radius of  $5 \times 10^{-3} \text{ mm}$ . It is not unreasonable to assume that the sample expansion may amplify these surface irregularities by a factor of 2 although large flaws should result very quickly in prohibitive MHD instabilities. A conservative estimate of the contribution of surface roughness to radius uncertainty is then  $10 \times 10^{-3} \text{ mm}$ , and this is corroborated by observation.

The various phenomenological contributors to the uncertainty in locating a single edge may be combined with random measurement

inconsistencies in a way less severe than additive to give a percentage error in the radius. The volume ratio is a function of  $r$  and  $r_0$  as follows:

$$f(r, r_0) = \frac{V}{V_0} = \frac{r^2}{r_0^2} \quad (3-5)$$

yielding an error given by

$$\frac{\Delta f}{f} = 2 \left( \frac{\Delta r}{r} + \frac{\Delta r_0}{r_0} \right) \quad (3-6)$$

Although most of the radius errors discussed are either absolute or grow not as a constant percentage they are converted to percentage errors here by choosing an average value for the radius. The film measurement uncertainty is chosen as  $5 \times 10^{-3}$  mm. The initial radius can be measured over a long period of time and therefore is susceptible only to a  $5 \times 10^{-3}$  mm surface roughness factor and a  $2 \times 10^{-3}$  mm film measurement error.  $\Delta r_0/r_0$  is then 1% and  $\frac{\Delta r}{r}$  is 1.7%. The total uncertainty in the volume ratio for an individual run is 5%. The excellent agreement of redundant data reduces this uncertainty to the neighborhood of 2%.

#### Temperature Analysis Technique

The technique for deducing the temperature of the sample is unique to this work and will be discussed in four major parts. This section will begin with a treatment of the theory necessary to radiation pyrometry and close with an outline of the calculational procedures used to implement that theory. An estimate of the uncertainties in the computed

temperatures will be made in Appendix A and details of the computer calculation are presented in Appendix B.

The basic assumption of the temperature determining technique is that the hot metal sample radiates with the characteristic blackbody spectrum modified by a wavelength and temperature dependent emissivity. In the experiment the emissions in three separate regions of this spectrum are continuously monitored with the pyrometers described in Chapter 2. The true sample temperature may be determined independently from each channel of pyrometric data and from the two possible unique ratios of these single channel data. To facilitate this discussion the true sample temperature deduced from the measured emission of a single channel is designated the SCT temperature, and the true sample temperature derived from the ratio of the measured intensities of two separate channels is labelled the TCT temperature.

The SCT temperature may be defined as that value of T which satisfies the following equality: (32)

$$I_i(T) = G_i \int_{\lambda_1}^{\lambda_2} \epsilon(\lambda, T) D_i(\lambda) B_i(\lambda) \frac{C_1}{\lambda^5 [e^{C_2/\lambda T} - 1]} d\lambda \quad (3-7)$$

where i designates pyrometric channel,

$G_i$  = geometrical calibration factor

$D_i$  = measured detector response function

$B_i$  = fractional transmission of the filter

$C_1 = 3.74126 \times 10^4$  watts  $\mu^4/\text{cm}^2$

$C_2 = 14388 \mu \text{ K}$

$\epsilon(\lambda, T)$  = sample emissivity.

The interference filter determines the limits of integration  $\lambda_1$ , and  $\lambda_2$ . Although in general  $\epsilon(\lambda, T)$  is unknown its wavelength dependence is believed to be weak enough that it may be assumed constant over the narrow spectral range defined by a given filter. Designating the central wavelength of channel  $i$  as  $\lambda_i$  Eq. (3-7) may be expressed as:

$$I_i(t) = G_i \epsilon(\lambda_i, T) F_i(T) \quad (3-8)$$

where

$$F_i(T) = \int_{\lambda_1}^{\lambda_2} D_i(\lambda) B_i(\lambda) \frac{C_1}{\lambda^5 [e^{C_2/\lambda T} - 1]} d\lambda \quad (3-9)$$

In practice  $F_i(T)$  is evaluated numerically for a set of discrete temperatures and then made a continuous function through the use of cubic splines.

In order to solve Eq. (3-8) for the SCT temperature it is necessary to evaluate  $G_i$  and  $\epsilon(\lambda_i, T)$ . Two general methods of finding the calibration factors,  $G_i$ , have been employed in this work. The first involves identifying some characteristic feature of the pyrometer trace to which a known temperature can be attached. For metals which melt above 2000 K the characteristic feature is the pyrometric response to the melting transition. At melt the temperature remains constant for the time required to add the enthalpy of fusion resulting in a relatively flat portion of the pyrometric trace. Within measurement error the melting temperature is independent of pressure so low pressure melting data may be used to obtain a melting temperature.  $G_i$  can then be evaluated as follows:

$$G_i = \frac{I_i(T_C) |_{\text{measured}}}{\epsilon(\lambda_i, T_C) F_i(T_C)} \quad (3-10)$$

where  $T_C$  is the known calibration temperature and  $I_i(T_C)$  is the experimentally determined intensity (at the melting plateau in this case).

A second calibration technique is necessary for those materials which do not undergo a significant phase transition within the temperature range in which the pyrometers have sufficiently sensitive response. For example lead melts at 600 K, a temperature at which the emitted radiation is below the threshold of detector response, and there is no recognizable feature of the pyrometer trace with which a known temperature can be associated. In these cases published low temperature-enthalpy data are extrapolated to the higher temperatures necessary for detector response. A constant  $C_p$ , in many cases estimated, is used for this extrapolation, the purpose being to associate an enthalpy with a known temperature. The enthalpy thus deduced will have been reached at a specific time in the experiment and the intensity measured at that time can be linked to the corresponding temperature. Eq. (3-10) is again used with these parameters to find  $G_i$ .

In concert with the work of Lincoln, et al. a linear temperature dependence is chosen for the emissivity.<sup>(16)</sup>

$$\epsilon(\lambda_i, T) = \epsilon(\lambda_i, T_C) [1 + a_i (T - T_C)] \quad (3-11)$$

Substitution of Eqs. (3-11) and (3-10) into (3-8) produces an expression for the SCT temperature of each channel in which the only remaining unknown parameter is  $a_i$ .



$$I_i(T) = \frac{I_i(T_c)}{F_i(T_c)} [1 + a_i(T - T_c)] F_i(T) \quad (3-12)$$

A suitable choice of  $a_i$  produces an equality which can be solved for the unknown SCT temperature,  $T$ .

The TCT temperature may be defined as that value of  $T$  which makes the measured intensity of any two channels at a given point in time satisfy the following equality:

$$\frac{I_i(T)}{I_j(T)} = \frac{I_i(T_c) F_j(T_c) [1 + a_i(T - T_c)] F_i(T)}{I_j(T_c) F_i(T_c) [1 + a_j(T - T_c)] F_j(T)} \quad (3-13)$$

where the unknown parameters are  $a_i$  and  $a_j$ , and all indicated intensities are, again, measured quantities.

With the three channels of pyrometry data there are for any given time three independent SCT temperatures derivable from Eq. (3-12) and two independent TCT temperatures derivable from Eq. (3-13). The choice of the adjustable parameters for each channel is made on the basis of forcing agreement among the five independently but redundantly chosen temperatures across the full range of temperatures reached during an experimental run. Employing this criterion it is possible to determine the adjustable parameter for each channel and the true temperature of the sample as a function of time.<sup>(16)</sup> Figure 13 illustrates the full range agreement experimentally attainable among the various SCT and TCT temperatures. Graphed results are lead temperatures recorded in 100 nm width channels centered at 450, 600 and 650 nm. In addition to the SCT temperatures for these three channels the TCT temperature derived from

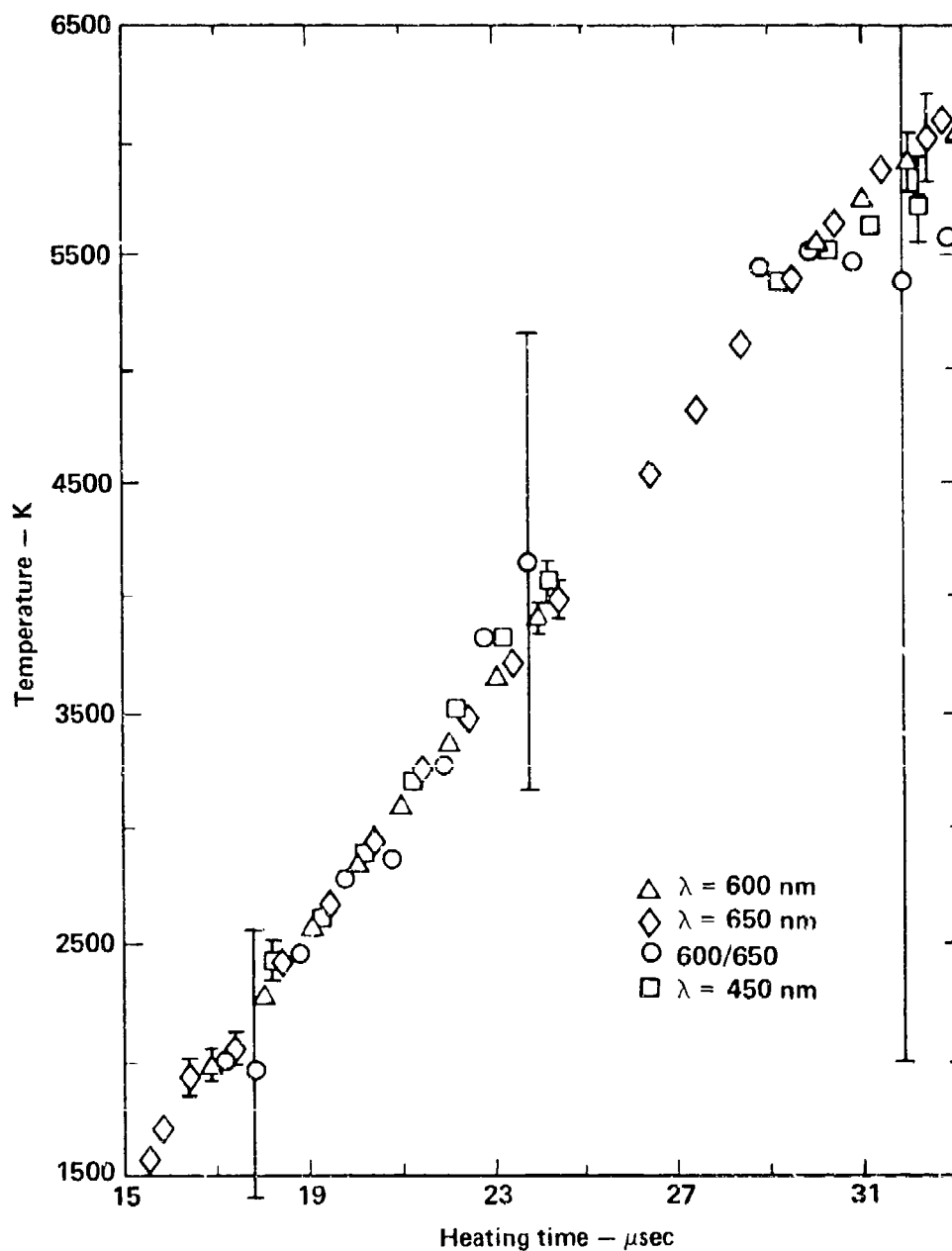


Fig. 13 SCT and TCT Temperatures for Lead at 0.3 GPa

SCT temperatures deduced from pyrometric data recorded at 450, 600, and 650 nm, and TCT temperatures from the ratio of the 600 to 650 nm data are plotted as a function of experimental time in  $\mu$ s. Error bars shown are calculated from the analyses of Appendix A and demonstrate good confidence in the SCT temperatures but large uncertainty in the TCT temperatures.

the ratio of the 600 nm to the 650 nm intensities is shown. Because of experimental uncertainties discussed in Appendix A the ultimate agreement among the independently deduced temperatures is frequently less than perfect. The extremely large uncertainties in the TCT temperature are the result of the fact that the ratio of the blackbody functions in Eq. (3-18) varies less than one order of magnitude for a 5000 K variation in temperature. On the other hand, the blackbody function for an individual channel may vary seven orders of magnitude over the same temperature range making the SCT temperature a much more exactly determined quantity.

Although it is quite possible to obtain very useful temperature data using this technique the emissivities themselves remain specified only in terms of an unknown quantity,  $\epsilon(\lambda_i, T_C)$  (see Eq. 3-11). As will be discussed in Chapter 4  $\epsilon(\lambda_i, T_C)$  must be obtained independently, and emissivity measurements at temperatures in the range of  $T_C$  are almost non-existent.

Several experimental and computational steps separate the pyrometer voltage response trace pictured in the upper portion of Figure 8 from the temperature curve in the lower part of the same figure. The temperatures are derived from application of Eqs. (3-12) and (3-13), which in turn involve the experimental intensities. A primary concern then is translating the oscilloscope trace in volts to measured intensities. The method of finding intensities and subsequently using them to find temperatures will be addressed next. Details necessary to actually implement the technique are discussed in Appendix B.

The usual calibration is done for each oscilloscope for each experimental run to convert the x and y deflections to time and voltage,

respectively. Response of the diode-amplifier-oscilloscope combination is then converted from volts to a relative intensity as follows. The output of a 1.5 watt argon-ion laser is focussed to an appropriate spot size on the integrated end of the trifurcated fiber optic bundle (see Figure 1). Because the amplifiers are ac coupled they respond only to a transient signal. For this reason the CW laser beam is shuttered with a Uniblitz shutter set to remain open approximately 8 ms. A pulse generator is used to trigger both the shutter and the oscilloscope sweeps with the triggering signal to the oscilloscopes delayed 4 ms with respect to the shutter open signal. The oscilloscopes thus sweep a 50-100  $\mu$ s segment of time some 4 ms after the shutter begins to open and well before it begins to close. During this time the shutter is completely open and not bouncing around, and the diodes are exposed to the full intensity of the laser. No interference filters are interposed between the laser and the diodes so each of the three diodes sees the same laser signal which is labelled  $I_0$ . Laser power and the spot size incident on the shutter opening are adjusted so that  $I_0$  is greater than or equal to the maximum signal recorded during a data run. Once these adjustments are made  $I_0$  is assumed to remain constant during the remainder of the calibration procedure.

The oscilloscope camera shutters are opened and the Uniblitz is shuttered, recording the pyrometric response to  $I_0$ . The laser beam is then attenuated with a neutral density filter and the resulting response recorded by triggering the Uniblitz. This process is repeated successively for neutral density filters numbered between 0.3 and 3.6. Intensity attenuation is related to filter number through the expression:

$$I_j/I_0 = 10^{-A_j} \quad (3-14)$$

where  $A_j$  is the neutral density number and  $I_j$  is the intensity transmitted by the  $j^{\text{th}}$  filter. A baseline is established by triggering the oscilloscopes without opening the Uniblitz shutter. The oscilloscope photograph produced is shown in the upper portion of Figure 14 and has the baseline and twelve other voltages recorded. Maximum intensity is at the bottom of the photograph and the baseline is at the top. Beginning immediately above  $I_0$  intermediate voltages correspond to  $A_j$ 's of 0.3, 0.6, 1.0, 1.3, 1.6, 2.0, 2.3, 2.6, 3.0, 3.3, and 3.6. In conjunction with Eq. (3-14) these voltages are used to create the relative intensity versus voltage transfer function graphed in the lower part of Figure 14. It should be noted that  $I_0$  is the lowest trace in the oscilloscope photograph while  $I_0$  relative to itself is one and appears at the top of the relative intensity graph. Points on the graph corresponding to oscilloscope traces are labelled with triangles.

Figure 14 illustrates instrumental idiosyncracies discussed in this chapter and in Appendix A. First, it is evident from the incorrect spacing between the  $A_1 = 0$  and  $A_2 = 0.3$  lines in the photograph that the full laser intensity  $I_0$  has saturated the pyrometer, and that, looking at the lower graph, the maximum voltage response is about 2.58 volts. In fact a straight line extrapolation of the linear portion of the graph indicates that  $I = 0.65 I_0$  would have been sufficient to saturate the diode and any signals stronger than that are lost information. Secondly, the response of the pyrometer near the baseline appears not to be truly logarithmic but somewhat stronger. One

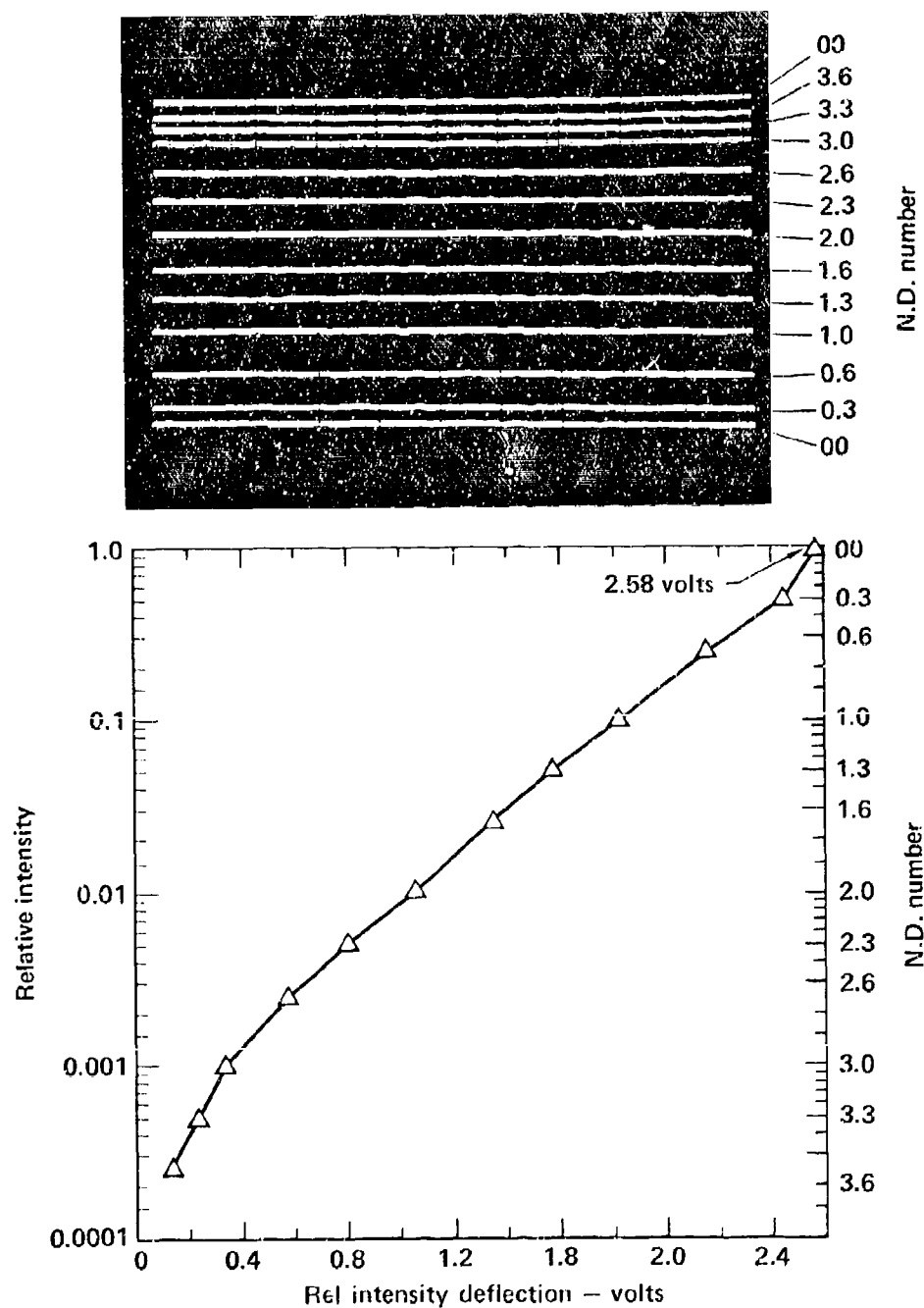


Fig. 14 Pyrometer Relative Intensity Calibration

(a) Pyrometric response to a defocused argon-ion laser beam. The bottom trace corresponds to the full beam which is then attenuated with neutral density filters of the indicated N.D. number to produce the remaining traces.

(b) Plot of intensity relative to unattenuated argon ion beam vs voltages measured from data of (a).

explanation might be that the low intensity signal might be indicative of a significant noise contribution, and the pyrometer response does not assume logarithmic characteristics until the intensity is high enough to completely overshadow the noise. It is this low intensity problem that makes a higher intensity calibration desirable. Minor deviations from linearity in the middle part of the graph are the result either of measurement uncertainty or of imperfectly characterized neutral density filters.

The transfer function of Figure 14 is made a continuous function by using cubic splines. With this function an intensity relative to the maximum laser intensity,  $I_0$ , is associated with measured points from the pyrometer data illustrated in Figure 8. It is these relative intensities that are labelled  $I_i(T)$  and are used in Eqs. (3-8) through (3-13). The relative intensity at the calibration point,  $I_i(T_c)$  is also derived from the transfer function.

At this point the sets of time voltage points read from the pyrometer traces have been transformed to discrete sets of time-relative intensity points read at arbitrary and differing times for each channel. These sets are made continuous functions with cubic splines, and used to produce sets of intensities at common times for all channels. All quantities required in Eqs. (3-12) and (3-13) have now been computed with the exception of the linear coefficients. To avoid complexity the calculation proceeds with two channels at a time. A two dimensional grid of possible  $a_i$ 's is chosen and evaluated one point at a time. For each choice of  $a_i$ 's two SCT and one TCT temperature are found for each point in time. The sum of the squares of the differences among the three temperatures for all common times defines a minimization function which

is computed for each point on the coefficient grid. The values of  $a_i$ 's which minimize this function then define best agreement of the SCT and TCT temperatures, and thus determine the temperature of the sample. It is these temperatures with their inherent qualifications which are reported in Chapter 4.



#### 4. THE MEASURED PROPERTIES OF LIQUID Pb, Pt, AuCu, U, Nb, AND NbHf

Sufficient data are presented here to establish the equation of state of six metals for liquid states at normal densities to as much as four fold expanded. The materials form a disparate group, ranging from the simple free electron metal lead to the more complex and less easily modelled uranium, and were chosen to provide a broad base of data on low density liquid metals. Lead, being the most compressible, provides the most revealing information, enabling surprisingly consistent estimates of the compressibility and the sound speed. Accurate measurements of pressure, enthalpy, density, temperature, and resistivity are reported for all six materials along with less exact estimates of  $C_p$ . The actual data are presented graphically with least squares fits obtained with a code by Knox<sup>(33)</sup> used to generate data tables.

##### Lead

Figure 15 displays measured enthalpy as a function of SCT temperatures determined from 600 nm and 650 nm channels for lead runs at 0.2 and 0.3 GPa. Calibration was established by extrapolating the 0.1 MPa data of Hultgren<sup>(34)</sup> to .3503 MJ/Kgm at 2600 K, and presumes a slightly larger  $C_p$  than estimated by Hultgren for the region of interest.  $C_p = 3.61 \pm 0.25R$  is chosen because it better represents the lower part of the measured temperatures and brings good agreement among the SCT and TCT temperatures. The two longest wavelength channels are in more consistent agreement with each other than they are with the shortest wavelength (450 nm) channel. This is attributed to the sensitivity of the calibration technique and the fact that the low temperature intensity

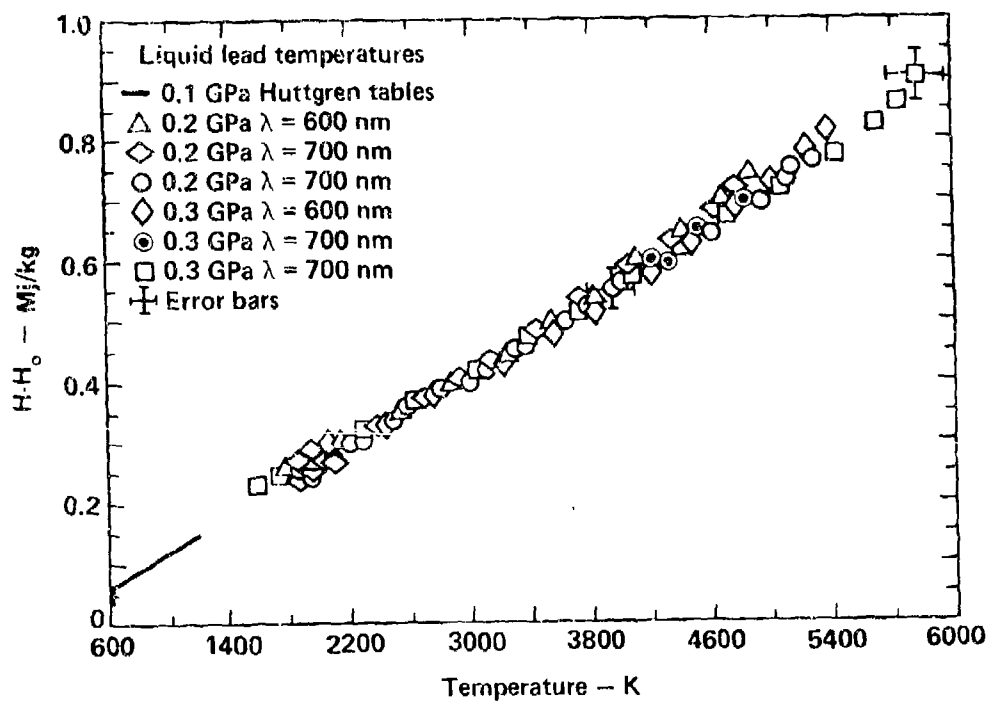


Fig. 15 Enthalpy vs Liquid Lead Temperature

Enthalpy is plotted as a function of SCT temperatures computed from data taken at 0.2 and 0.3 GPa in the 600 and 650 nm channels. The calibration point, 2600 K and 0.35 MJ/kg, is extrapolated from the plotted 0.1 MPa literature data. The vertical scale is specific enthalpy with respect to cell pressure and 300 K.

is much stronger in the long wavelength channels and therefore more precisely determined. A least squares fit of these six data traces is given below and selected values presented in Table 1.

$$\begin{aligned}
 H &= C_1 + C_2 T + C_3 T^2 \\
 C_1 &= 2.227465 \times 10^{-2} \\
 C_2 &= 1.167629 \times 10^{-4} \\
 C_3 &= 4.682139 \times 10^{-9}
 \end{aligned}
 \tag{4-1}$$

Enthalpy is referenced to 300 K and the pressure of each individual run. As discussed in detail elsewhere,<sup>(15)</sup> the enthalpy necessary to reach a given temperature is almost independent of pressure for the moderate pressures and temperatures of this work. The difference in the enthalpy necessary to reach a given temperature along separate isobars can be expressed as  $\Delta H \approx V(T_0, P) [(T - T_0)\alpha]^2 \delta P$  where  $T_0 = 300\text{K}$  and  $\alpha$  is the thermal expansion coefficient.  $V(T_0, P)$  is independent of pressure for the moderate pressures germane to the IEX so a sufficiently small  $\alpha$  will establish that  $\Delta H$  is insignificant on the scale of the experimental uncertainty associated with the data of Figure 15. As reported by Gschneidner<sup>(35)</sup>  $\alpha = 29 \times 10^{-6} \text{ K}^{-1}$  for lead at standard temperature and pressure. A rather inexact calculation based on the data of Figure 18 places  $\alpha$  between  $100 \times 10^{-6}$  and  $500 \times 10^{-6} \text{ K}^{-1}$  over a temperature range of 2600 K to 6000 K. An  $\alpha$  of  $300 \times 10^{-6} \text{ K}^{-1}$  produces a predicted separation of 5% in enthalpy between the 0.2 GPa and 0.3 GPa data at 5300 K. No such systematic offset is observed leading to the conclusion that  $\alpha$  must remain below  $100 \times 10^{-6} \text{ K}^{-1}$  until very near the

Table 1  
Measured Properties of Liquid Lead

$T(^{\circ}\text{K})$	$H-H(T_0, P)$ Mj/kgm	$\frac{V}{V_0}$ 0.1 GPa	$\frac{V}{V_0}$ 0.2 GPa	$\frac{V}{V_0}$ 0.3 GPa	$\frac{V}{V_0}$ 0.4 GPa
1600	.2211	1.204	1.202	1.178	1.149
1800	.2476	1.236	1.226	1.206	1.174
2000	.2745	1.267	1.250	1.235	1.201
2200	.3018	1.298	1.276	1.265	1.229
2400	.3295	1.329	1.302	1.296	1.259
2600	.3575	1.359	1.329	1.327	1.290
2800	.3859	1.390	1.358	1.359	1.322
3000	.4147	1.420	1.388	1.391	1.355
3200	.4439	1.451	1.420	1.424	1.389
3400	.4734	1.483	1.454	1.457	1.424
3600	.5033	1.518	1.491	1.491	1.460
3800	.5336	1.557	1.531	1.526	1.497
4000	.5642	1.602	1.575	1.563	1.535
4200	.5953	1.654	1.623	1.601	1.574
4400	.6267	1.717	1.675	1.642	1.615
4600	.6585	1.793	1.732	1.686	1.657
4800	.6906	1.885	1.795	1.733	1.702
5000	.7231	1.998	1.865	1.785	1.748
5200	.7560	2.135	1.942	1.844	1.798
5400	.7893	2.302	2.028	1.909	1.851
5600	.8230		2.122	1.984	1.896
5800	.8570		2.227	2.068	1.969
5980	.8880		2.331	2.155	2.028
	.9000		2.374	2.192	2.032
	.950		2.567	2.362	2.162
	.97		2.652		
	1.000			2.568	2.285
	1.05			2.815	2.426
	1.10			3.110	2.587
	1.15			3.462	2.773
	1.18			3.70	
	1.20				2.985
	1.25				3.230
	1.30				3.510
	1.33				3.70

liquid-vapor two phase boundary and then climb steeply.  $\alpha = 100 \times 10^{-6} \text{ K}^{-1}$  yields a 0.5% offset in enthalpy at 5300 K which is indiscernible with respect to the measurement error of the experiment.

As noted in Chapter 3 the method of determining the temperatures graphed in Figure 13 and 15 does not require knowledge of the absolute sample emissivity (see Eq. 3-12 and 3-13). Computations do produce the  $a_i$ 's, however, and these provide sample emissivities relative to the calibration point emissivities for each channel through Eq. (3-11). In order to obtain a set of absolute emissivities it is necessary to employ a standard for which an emissivity is known to find the  $G_i$ 's for each channel. For these lead data accompanying calibration runs were made on tantalum which has a distinctly identifiable melting plateau within the range of maximum detector sensitivity. Using Eq. (3-10) and the temperature trace of the tantalum control run associated with a given lead run, a value for  $G_i \epsilon_{\text{Ta}}(\lambda_i, T)$  may be obtained at  $T=3270 \text{ K}$ , the tantalum melting point. The tantalum melting point emissivities are known for specific wavelengths<sup>(36)</sup> and interpolation of these data provides representative values for the  $\lambda_i$ 's of this experiment. Assuming the  $G_i$ 's have not changed significantly between the lead and tantalum runs they can be calculated and then used in Eq. (3-10) to find the lead emissivity at the calibration temperature. Application of this calculation is outlined in Table 2 and the resulting emissivities graphed in Figure 16.

It should be pointed out that while this temperature analysis technique results in true sample temperatures with small uncertainties, the emissivities are known much less precisely. There are two major sources of error in the emissivity determination, the large number of

Table 2  
Lead Emissivity Determination

Chan	$\lambda_i$	$G_i \epsilon_{pb}(\lambda_i, T_{TP})$	$G_i \epsilon_{pb}(\lambda_i, T_m)$	$I_i \hat{T}_a(\lambda_i, T_m)$
1	450	$8.60 \times 10^{-4}$	$1.9278 \times 10^{-4}$	$1.2546 \times 10^{-2}$
2	600	$1.8658 \times 10^{-3}$	$1.9320 \times 10^{-3}$	$5.8709 \times 10^{-2}$
3	650	$1.96 \times 10^{-3}$	$2.0393 \times 10^{-3}$	$6.6767 \times 10^{-2}$

	$G_i \epsilon_{Ta}(\lambda_i, T_m) = \frac{I_i T_m(T_m)}{F(\lambda_i, T_m)}$	$\epsilon_{Ta}(\lambda_i, T_m)$	$G_i$	$\epsilon_{Pb}(\lambda_i, T_m)$	$\epsilon_{Pb}(\lambda_i, 2000)$	$\epsilon_{Pb}(\lambda_i, 6000)$
1	$4.2548 \times 10^{-3}$	.40	$1.0637 \times 10^{-2}$	.087	.075	.113
2	$5.2633 \times 10^{-3}$	.38	$1.3851 \times 10^{-2}$	.140	.131	.160
3	$4.2158 \times 10^{-3}$	.37	$1.1394 \times 10^{-2}$	.180	.167	.196

Tie Point Calculation

$$T_{TK} = 2600 \text{ K}$$

$$H_{TP} = .3501 \text{ MJ/kgm}$$

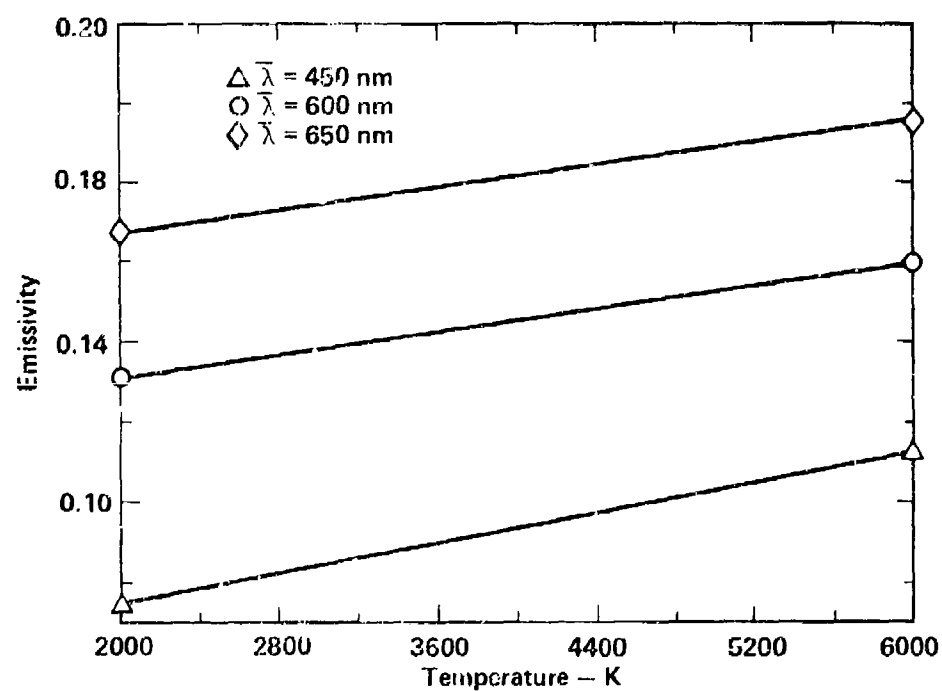


Fig. 16 Measured Emissivities of Liquid Lead  
Emissivities computed from lead data taken at wavelengths of 450, 600, and 650 nm.  
The calculation is outlined in Table 2 and makes use of the known emissivity of tantalum at 3270 K.

arithmetic operations involving uncertain numbers and the uncertainty in the measured lead intensities. The emissivities are presented in Table 3 along with their uncertainties. The computed emissivity variation with temperature is within the measurement error for the temperature range of the experiment and may, in fact, just compensate for the unavoidable uncertainties in the calibration technique. The blue channel which was calibrated at a point nearest minimum detector response exhibits the strongest temperature dependence in its emissivity. It can be said with surety that the liquid lead emissivities are much less than those of tantalum at its melting point, but further deductions are not warranted.

Figure 17 presents the volume expansion of lead along four isobars. The enthalpy is referenced to a state at 0.1 MPa and 298 K. An initial enthalpy input of 0.0086, 0.0172, 0.0257 and 0.0342 MJ/kgm is produced by the work done on the sample during pressurization of the cell for shots at 0.1, 0.2, 0.3 and 0.4 GPa, respectively. These enthalpies are computed from  $\Delta H = (1 - \alpha T) V \Delta P$  using a thermal expansion coefficient of  $29 \times 10^{-6} \text{ K}^{-1}$ . Subsequent enthalpy increases produced by electrical heating are then added to these amounts. Least squares 4th order fits for the four isobars are:

$$V/V_0 = C_1 + C_2 H + C_3 H^2 + C_4 H^3 + C_5 H^4 \quad (4-2)$$

$$H = B_1 + B_2 \frac{V}{V_0} + B_3 \left(\frac{V}{V_0}\right)^2 + B_4 \left(\frac{V}{V_0}\right)^3 + B_5 \left(\frac{V}{V_0}\right)^4$$

where both sets of coefficients are listed in Table 4 and representative values of the parameters are tabulated in Table 1. Also graphed in Figure 17 are lead expansion data derived from Lucas' <sup>(37)</sup> 0.1 MPa



Table 3  
Comparison of Tantalum and Lead Emissivities at 3270 K

Channel	$\lambda$ (nm)	$\epsilon_{Ta}^*$	$\epsilon_{Pb}$
1	450	.40	.09 $\pm$ .05
2	600	.38	.14 $\pm$ .06
3	650	.37	.18 $\pm$ .06

\*From Ref. 34 by interpolation.

Table 4  
Lead Enthalpy-Volume Coefficients

	0.1 GPa	0.2 GPa	0.3 GPa	0.4 GPa
$B_1$	$2.316871 \times 10^{-1}$	-1.806757	-2.334034	-2.429936
$C_1$	1.009796	$9.806604 \times 10^{-1}$	1.012996	1.015107
$B_2$	-2.600625	2.356379	3.600521	3.823210
$C_2$	$1.992454 \times 10^{-2}$	$9.947246 \times 10^{-1}$	$2.932559 \times 10^{-2}$	$-6.336762 \times 10^{-2}$
$B_3$	3.896541	$-5.004613 \times 10^{-1}$	-1.539651	-1.694714
$C_3$	6.296780	$-3.785522 \times 10^{-1}$	3.879281	3.134925
$B_4$	-1.757053	$-6.135478 \times 10^{-2}$	$3.188688 \times 10^{-1}$	$3.718307 \times 10^{-1}$
$C_4$	$-1.433270 \times 10^{+1}$	$2.061060 \times 10^{-1}$	-6.163421	-3.754703
$B_5$	$2.612217 \times 10^{-1}$	$2.438690 \times 10^{-2}$	$-2.597707 \times 10^{-2}$	$-3.192306 \times 10^{-2}$
$C_5$	$1.122190 \times 10^{+1}$	$9.049582 \times 10^{-1}$	3.699364	1.867036

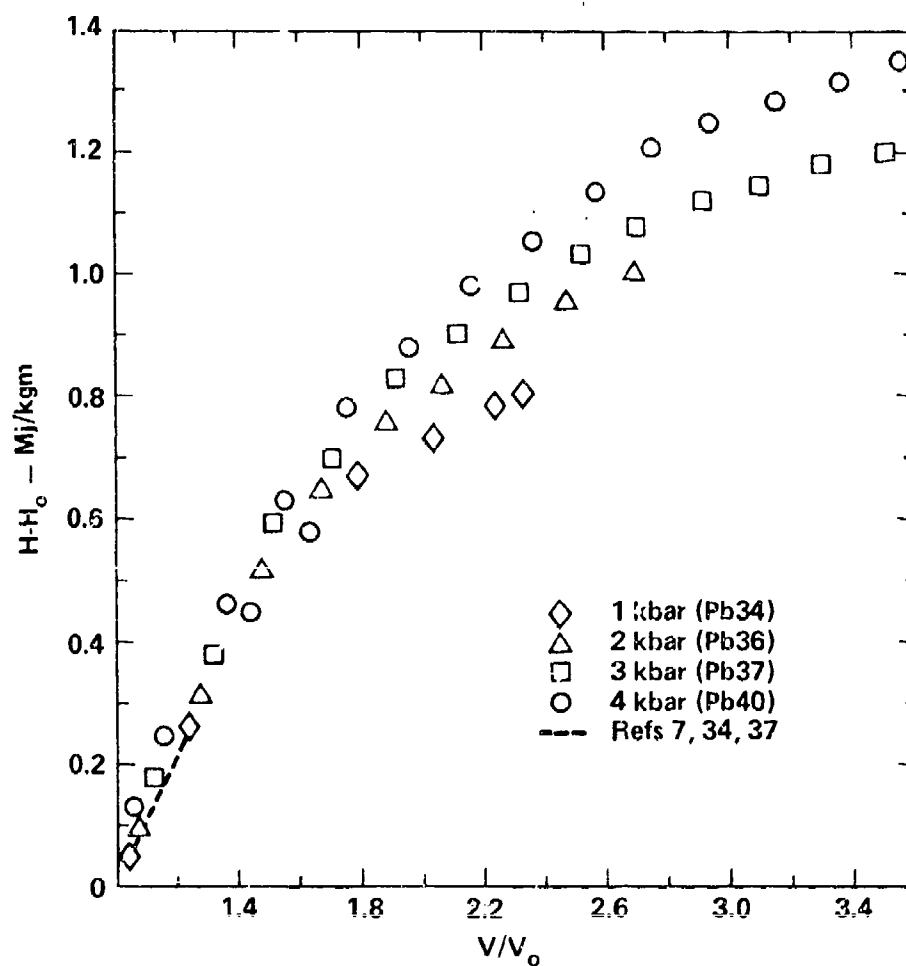


Fig. 17 Volume Expansion of Liquid Lead

Enthalpy as a function of specific volume for lead at 0.1, 0.2, 0.3 and 0.4 GPa. The vertical scale is enthalpy with respect to 300 K and 0.1 MPa. Literature values are the 0.1 MPa data of Kirshenbaum, et al<sup>(7)</sup> with the work of Hultgren, et al<sup>(34)</sup> and Lucas<sup>(37)</sup> used to transform from temperature to enthalpy.

volume temperature relationship using the Hultgren tables<sup>(34)</sup> for conversion to volume-enthalpy. These data are most accurate for  $V/V_0 < 1.15$ , employing extrapolated values for enthalpy as a function of temperature for  $V/V_0 > 1.15$ . On the scale of Figure 17 the data of Kirshenbaum, et al.<sup>(7)</sup> are coincident with those of Lucas where again the Hultgren table is used for enthalpy temperature dependence.

The end points of the individual isobaric expansions were reached as the sample resistivity turned steeply upwards (see Figure 20). An abrupt sharp increase in resistivity is interpreted here to indicate near entry into the two phase region at sub-critical pressures and expansion to critical density at super-critical pressures. As illustrated in Figure 17 this point is reached for expansions of 2.3, 2.7, 3.6 and 3.6 at 0.1, 0.2, 0.3, and 0.4 GPa, respectively. These points define a critical dome and a critical specific volume in the neighborhood of 3.6 fold expanded. A further mildly daring interpretation of these data indicate a critical pressure greater than 0.2 GPa but less than 0.3 GPa, deduced from the fact that the insulating transition occurs at similar expansions for the 0.3 and 0.4 GPa isobars.

Similar reasoning can be applied to the temperature data of Figure 15. The 9.2 GPa temperatures reach approximately 5300 K while the 0.3 GPa temperatures go as high as 6000 K. The critical temperature can be limited to the 5300 to 6000 K range and depends upon how far above 0.2 GPa the top of the critical dome is. Specification of the critical temperature is made less precise by the constant pressure nature of the experimental track. Near the critical region in the pressure-volume plane the isotherms become nearly parallel to the isobars over a significant range of volumes. It is therefore difficult to associate a

specific temperature with a given specific volume. These estimates for the critical parameters of lead are compared with other estimates in Table 5. The soft sphere parameters are based on a modelling of these data<sup>(5)</sup> while the "shock wave" results are based upon the behavior of release adiabats of shock compressed porous lead samples.<sup>(45)</sup> The corresponding states entry is somewhat approximate in that it depends upon measured data in cesium and mercury and on an accurate measurement of the enthalpy of vaporization of lead, a difficult experiment. The accuracy of the current work could be improved as will be discussed in Chapter 6.

---

Table 5  
Comparison of Various Estimates for the  
Critical Point Parameters of Lead

Source	$T_c (^{\circ}\text{K})$	$\frac{V_c}{V_0}$	$P_c (\text{GPa})$
This Work	5300-6000	3.6-3.7	0.2-0.3 GPa
Soft Sphere <sup>(5)</sup>	5158	3.7	0.226 GPa
Shock Wave <sup>(45)</sup>	5300	4.9	0.170 GPa
Hard Sphere <sup>(4)</sup>	4668	3.66	0.208
Corresponding States <sup>(46)</sup>	4980	3.49	0.184

---

The common enthalpy parameter can be used to deduce from the data of Figs. 15 and 17 the expansion of liquid lead as a function of temperature. This has been done using the least squares fits of Eqs. (4-1) and (4-2) and presented graphically in Figure 18. The coefficient of thermal expansion at 2000 K is computed to be  $120 \times 10^{-6}$ ,  $100 \times 10^{-6}$ ,  $120 \times 10^{-6}$ , and  $115 \times 10^{-6} \text{ K}^{-1}$  at 0.1, 0.2, 0.3 and 0.4 GPa,

respectively. To the accuracy of the calculation these values are indistinguishable but are less than the  $150 \times 10^{-6} \text{ K}^{-1}$  reported by Kirshenbaum, et al. (7) This difference is due to the fact that 2000 K is very close to the liquid-vapor two phase region at 0.1 MPa but far removed for the pressures of this work. The thermal expansion coefficient increases rapidly as the two phase boundary is approached at 0.1 and 0.2 GPa yielding a maximum value of  $400 \times 10^{-6} \text{ K}^{-1}$  for the 0.1 GPa isobar at 5400 K and a still growing value of  $260 \times 10^{-6} \text{ K}^{-1}$  at 5960 K for the 0.2 GPa isobar. The two phase boundary is estimated to be near  $V/V_0 = 2.3$  and 2.7 for 0.1 and 0.2 GPa. Less dramatic growth is observed for the thermal expansion coefficients along the two higher pressure isobars because they do not approach critical density for the temperature range of these data, and they are estimated to be above critical pressure. Representative values of the data of references (7) and (37) are plotted for comparison.

Values of the specific heat,  $C_p$ , derived from Eq. (4-1) range from 3.37R at 2000 K to 4.31R at 6000 K. The width and height of the error bars on the data of Figure 15 allow a broad possible range of heat capacities and the choice of a second order fit is arbitrary. It is possible that the heat capacity remains fairly constant to a temperature of approximately 4500 K and then increases above that. Cordoba and Brooks (38) report a heat capacity approaching 3.25R at 800 K while Hultgren, et al. report a heat capacity of 3.44R at 1300 K. (34) To within experimental accuracy the current data is in agreement with these values.

In addition to  $C_p$  it is possible to use the least squares fits to the data reported here to compute several other thermophysical properties

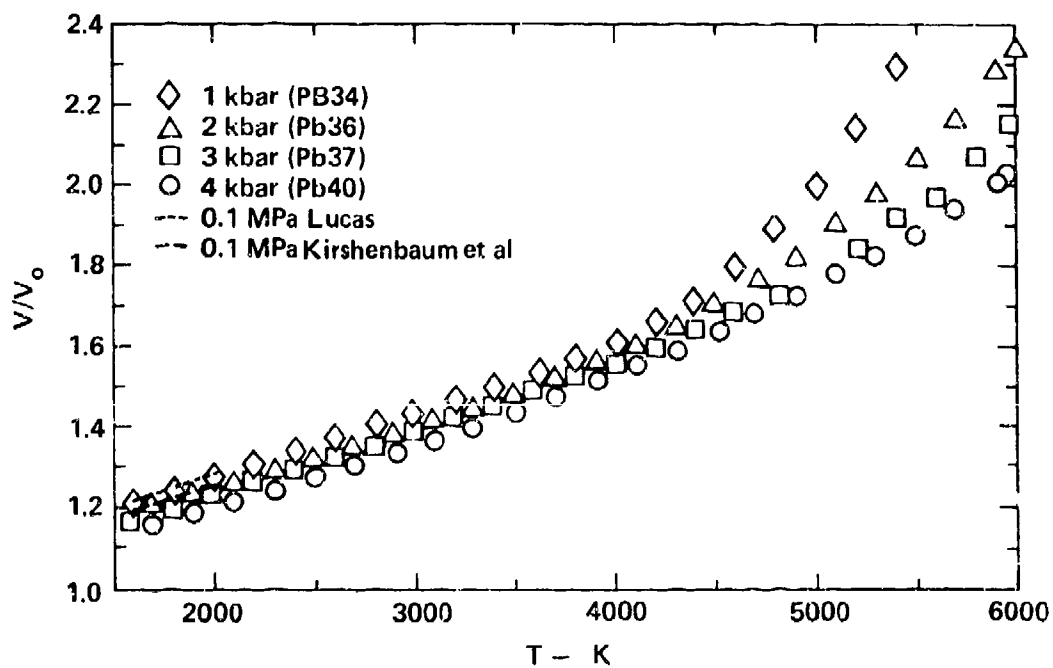


Fig. 18 Thermal Expansion of Liquid Lead

These are the data of Fig. 17 with the data of Fig. 15 used to convert from enthalpy to temperature. Lucas' (37) and Kirshenbaum's, et al (7) data are plotted for comparison.

of liquid lead. Table 6 is a tabulation of computed properties for lead at 0.3 GPa. The temperature range extends only over regions where there is sufficient separation of the isobars to calculate isothermal compressibility,  $K_T = \frac{1}{V} \left( \frac{\partial V}{\partial p} \right)_T$ . It should be remembered that the large number of arithmetic operations performed with experimentally inaccurate numbers renders the computed values of Table 6 inexact, even though they are obviously consistent and appear reasonable. The compressibility is particularly susceptible to inaccuracies in the data because its calculation involves the difference of large almost equal numbers. The resulting error is then carried forward to the dilation term, the ratio of specific heats, and the sound velocity. Because of the lack of data in this temperature range the sound velocities are compared in Figure 19 with Grover's projections based upon Lindemann Law melting point scaling. (39,40,41)

The last four columns of Table 6 display the results of a theoretical estimate of the specific heat at constant volume and the difference in the measured  $C_p$  and the estimated  $C_v$ .  $C_{ve}$  is computed from the free electron expression for electronic heat capacity<sup>(42)</sup> using the experimentally determined specific volume.

$$C_{ve} = \frac{\pi^2}{2} N_e \left[ \frac{KT}{\epsilon_f} \right] R \quad (4-3)$$

The lattice contribution to the specific heat,  $C_{vl}$ , is taken from Grover's expression based upon Lindemann type scaling<sup>(39)</sup>

$$C_{vl} = \frac{3}{2} \left[ 1 + \frac{1}{1+\alpha} \frac{T}{T_m} \right] \quad (4-4)$$

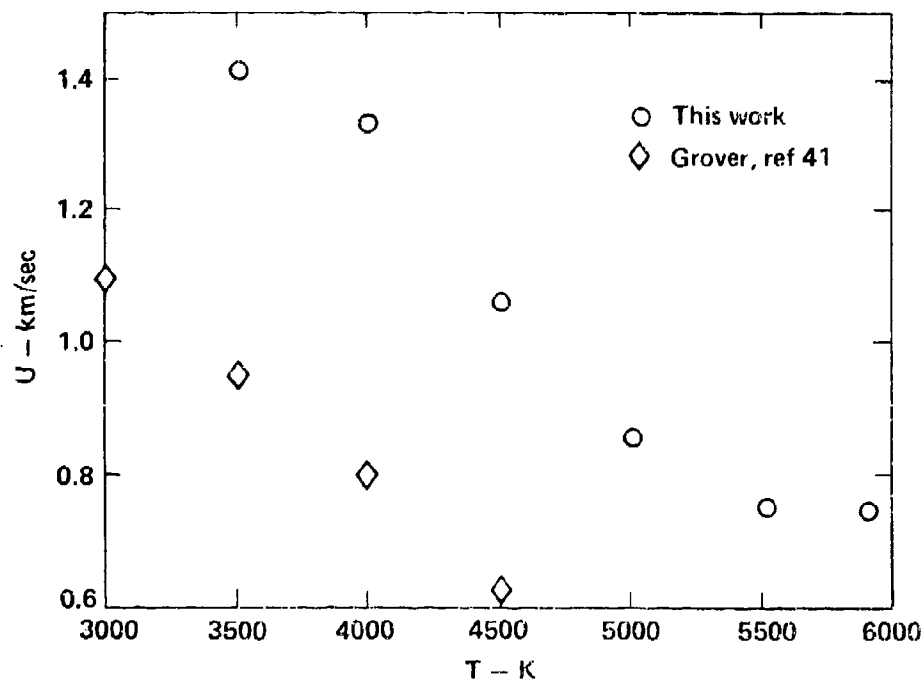


Fig. 19 Sound Velocity in Liquid Lead at 0.3 GPa

The sound velocity is computed using the thermal expansion coefficients and isothermal compressibilities deduced from the data of Fig. 18. Comparison is made to sound velocities calculated by Grover using the "GRAY" model. (39-41) Agreement is considered excellent and fortuitous because of the inherent inaccuracies of each method.



which has been found to be in agreement with soft-sphere modelling over a broad temperature range.  $\alpha$  has been chosen as 0.125 to give best agreement with published data while  $T_m$  is the temperature of melt at a given density and can be calculated using the Lindemann scaling law and the Gruneisen relationship. The Lindemann scaling law is<sup>(40)</sup>

$$\frac{T_m}{T_0} = \left( \frac{\theta_m}{\theta_0} \right)^2 \left( \frac{V_m}{V_0} \right)^{2/3} \quad (4-5)$$

where the subscript m refers to the melting state at specific volume  $V_m$  and the subscript 0 refers to the melting state at standard pressure. The Gruneisen expression is

$$\gamma_G = - \frac{d \ln \theta}{d \ln V} \quad (4-6)$$

and provides a relationship for the normal mode variation as a function of volume.<sup>(43)</sup> The parameter  $\gamma_G$ , is usually inferred from high pressure shock wave experiments but Ross has found it to follow well the linear relationship  $\gamma_G = cV + \frac{1}{2}$ .<sup>(44)</sup> The constant c is determined using  $\gamma_G = 2.62$  at  $V_0 = 1.03$  normal density.<sup>(7,35)</sup> Integration of Eq. (4-6) and its substitution in Eq. (4-5) yields:

$$T_m = T_0 \left[ \frac{V_m}{V_0} \right]^{-1/3} e^{2c(V_0 - V_m)} \quad (4-7)$$

Consistent measurements and calculations should yield reasonable agreement between  $C_p - C_v$  and the dilation term. In view of the estimated nature of the involved parameters the agreement is quite good.

Table 6  
Thermophysical Properties of Liquid Lead at 0.3 GPa

T(K)	$V/V_0$	$K_T \times 10^1$ GPa <sup>-1</sup>	$\alpha \times 10^6$ K <sup>-1</sup>	$D = \frac{\alpha^2 VT}{K_T}$	$C_P$ R	$\gamma = C_P/C_V$ $= [1 - \frac{D}{C_P}]^{-1}$	U km/sec	$C_{ve}$ R	$C_{vL}$ R	$C_V$ R	$D = C_P - C_V$ R
3000	1.3910	1.193	117	1.051	3.603	1.410	1.204	0.674	1.928	2.602	1.006
3500	1.4742	1.055	115	1.419	3.715	1.615	1.410	0.817	1.800	2.616	1.109
4000	1.5630	1.289	120	1.533	3.841	1.664	1.333	0.971	1.700	2.671	1.170
4500	1.6633	2.011	131	1.401	3.958	1.548	1.062	1.138	1.627	2.765	1.193
5000	1.7854	3.279	154	1.417	4.074	1.533	0.858	1.326	1.573	2.900	1.174
5500	1.9452	5.020	190	1.688	4.191	1.674	0.743	1.545	1.536	3.081	1.110
5900	2.1152	6.680	229	2.150	4.284	1.998	0.747	1.752	1.518	3.270	1.014

Plotted in Figure 20 are the measured resistivities as a function of specific volume for runs at 0.1, 0.2, 0.3 and 0.4 GPa. Also graphed are the measurements of Banchilla and Filippov which were taken at variable and unspecified pressures for temperatures as high as 2500 K.<sup>(48)</sup> The conversion from temperature to specific volume was done using Lucas' density temperature relationship which is graphed in Figure 18.<sup>(34)</sup> The current data are in excellent agreement with Banchilla and Filippov over the limited volume range of their measurements. Lead resistivities are apparently a function of specific volume (or density) alone as evidenced by the agreement of the four isobars of resistivity data which are at differing temperatures for a given expansion (see Figure 18). The large expansions are accompanied by liquid state resistivities which grow as much as a factor of seven for the subcritical 0.2 GPa data and a factor of almost 24 for the supercritical 0.4 GPa data. This should be contrasted to platinum, for example, whose liquid state resistivity increases only a factor of two by the time the isobaric expansion reaches the neighborhood of the liquid-vapor two phase region (see Figure 23). The pronounced volume dependence will be discussed further in Chapter 5 where the volume dependent resistivity projected by the nearly free electron model is shown to apply well to lead. A least squares fit of the liquid state data is given below and representative values tabulated in Table 7. Although the lead resistivities

$$\rho = C_1 + C_2 \left( \frac{V}{V_0} \right) + C_3 \left( \frac{V}{V_0} \right)^2 + C_4 \left( \frac{V}{V_0} \right)^4 \quad (4-8)$$

$$C_1 = 0.512205$$

$$C_2 = -0.785519$$

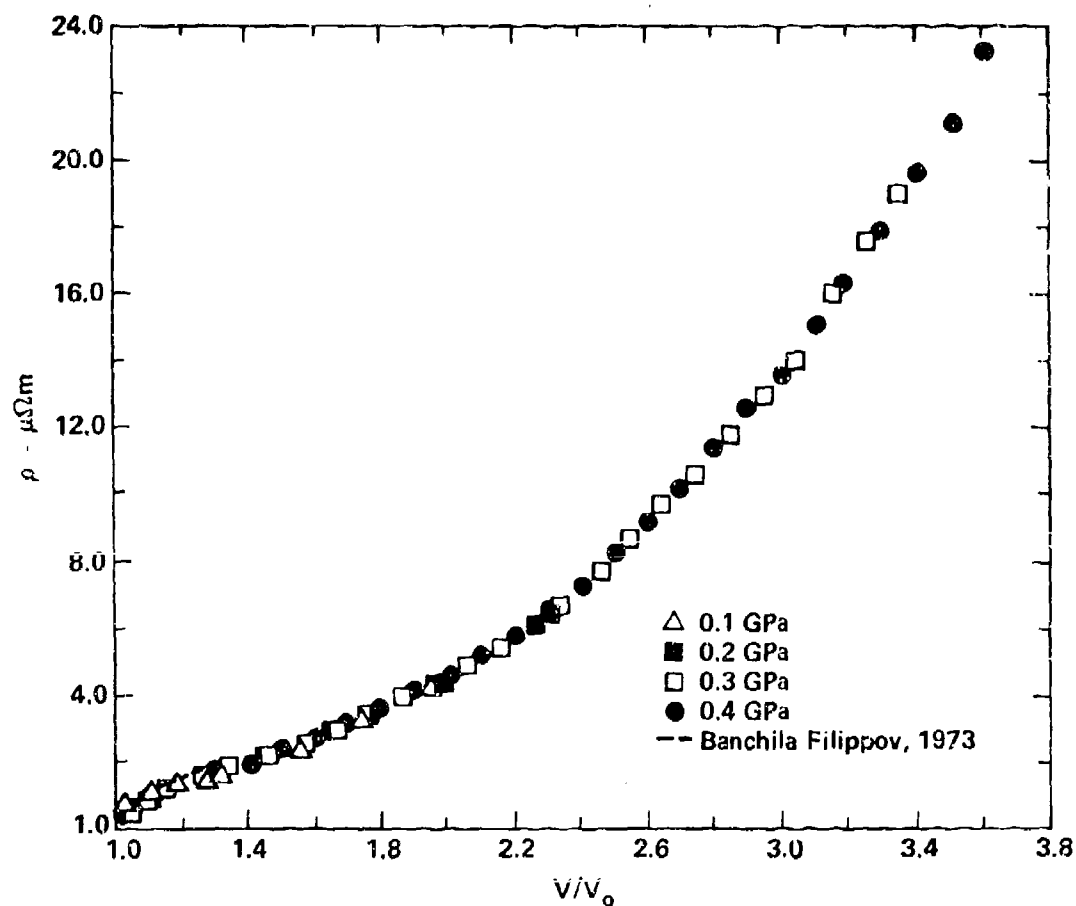


Fig. 20 Liquid Lead Resistivity

Resistivity in  $\mu\Omega\text{m}$  is shown to be a function of specific volume for lead at 0.1, 0.2, 0.3, and 0.4 GPa. Comparison is made with the data of Banchila and Filippov<sup>(48)</sup> which demonstrates the excellent agreement of the two data sets over the limited range of the previous work.

$$C_3 = 1.197060$$

$$C_4 = 0.056275$$

are not a unique function of temperature, the temperature dependence along the various isobars can be deduced by fitting the data of Figure 18 and using volumes so calculated in Eq. 4-8. The volume versus temperature expression necessary to do this is:

$$\frac{V}{V_0} = C_1 + C_2T + C_3T^2 + C_4T^3 + C_5T^5 \quad (4-9)$$

where the coefficients for four isobars are listed in Table 8.

#### Platinum

Platinum specific volume enthalpy data taken at pressures of 0.2, 0.3 and 0.4 GPa are plotted in Figure 21. Enthalpy is referenced to 0.1 MPa and 298 K. Ordinate values are the measured electrically added enthalpies plus an enthalpy of cold compression. As with lead the compressional enthalpies are calculated from the expression  $\Delta H = (1-\alpha T)V_0\Delta P$  where  $\alpha$ , the coefficient of thermal expansion, is  $26.85 \times 10^{-6} \text{ K}^{-1}$ . (35)  $\Delta H$  is then 0.0092, 0.0139, and 0.0185 MJ/Kgm for 0.2, 0.3, and 0.4 GPa, respectively. The compressibility is sufficiently low that expected resolution among the plotted isobars is smaller than experimental uncertainties. Therefore, the following second order expression is fit to all the liquid phase data of Figure 21:

$$\frac{V}{V_0} = A_1 + A_2H + A_3H^2 \quad (4-10a)$$

Table 7  
The Resistivity of Liquid Lead for  
 $V/V_0$  between 1.15 and 3.65

$V/V_0$	$\rho(\mu\Omega m)$	$V/V_0$	$\rho(\mu\Omega m)$	$V/V_0$	$\rho(\mu\Omega m)$
1.15	1.290	2.00	4.630	2.85	11.709
1.20	1.410	2.05	4.926	2.90	12.282
1.25	1.538	2.10	5.236	2.95	12.874
1.30	1.675	2.15	5.559	3.00	13.487
1.35	1.820	2.20	5.896	3.05	14.122
1.40	1.975	2.25	6.247	3.10	14.778
1.45	2.139	2.30	6.613	3.15	15.456
1.50	2.312	2.35	6.993	3.20	16.157
1.55	2.495	2.40	7.389	3.25	16.882
1.60	2.689	2.45	7.801	3.30	17.630
1.65	2.892	2.50	8.228	3.35	18.402
1.70	3.106	2.55	8.672	3.40	19.200
1.75	3.331	2.60	9.134	3.45	20.023
1.80	3.567	2.65	9.612	3.50	20.872
1.85	3.815	2.70	10.109	3.55	21.747
1.90	4.074	2.75	10.623	3.60	22.650
1.95	4.346	2.80	11.157	3.65	23.581

Table 8  
Least Squares Coefficients for Fit of  
 $V/V_0$  versus Temperature for Liquid Lead

	0.1 GPa	0.2 GPa	0.3 GPa	0.4 GPa
$C_1$	1.250943	1.050965	1.13140	1.10334
$C_2$	$-3.43794 \times 10^{-4}$	$6.23018 \times 10^{-5}$	$-1.27027 \times 10^{-4}$	$-9.16413 \times 10^{-5}$
$C_3$	$3.09513 \times 10^{-7}$	$3.00071 \times 10^{-8}$	$1.41486 \times 10^{-7}$	$1.01549 \times 10^{-7}$
$C_4$	$-8.34668 \times 10^{-11}$	$-8.12790 \times 10^{-12}$	$-3.15433 \times 10^{-11}$	$-1.85068 \times 10^{-11}$
$C_5$	$8.26025 \times 10^{-15}$	$1.22937 \times 10^{-15}$	$2.71183 \times 10^{-11}$	$1.41846 \times 10^{-15}$

$$A_1 = 0.99265$$

$$A_2 = 0.19299$$

$$A_3 = 0.15811$$

The inverse relation is:

$$H = B_1 + B_2 \left( \frac{V}{V_0} \right) + B_3 \left( \frac{V}{V_0} \right)^2 \quad (4-10L)$$

$$B_1 = -3.34273$$

$$B_2 = 4.43530$$

$$B_3 = -0.899656$$

Representative values computed with Eq. (4-10) are presented in Table 9. Error bars indicated in Figure 21 represent 5% uncertainty in the volume measurement and 2% uncertainty in the enthalpy as discussed in Chapter 3, and appear overly pessimistic in view of the agreement among the individual data runs.

Solid platinum densities are compared to those measured by Waseda, et al<sup>(49)</sup> using x-ray diffraction techniques. Waseda's expression for the dilation of an individual lattice parameter as a function of temperature is:

$$\frac{\Delta a}{a} = 5.546 \times 10^{-6} (T-298) + 3.750 \times 10^{-9} (T-298)^2 \quad (4-11)$$

and, because of the cubic structure of platinum, results in a volume expansion of  $V/V_0 = 1 + 3 \frac{\Delta a}{a_0}$  where only first order terms have been

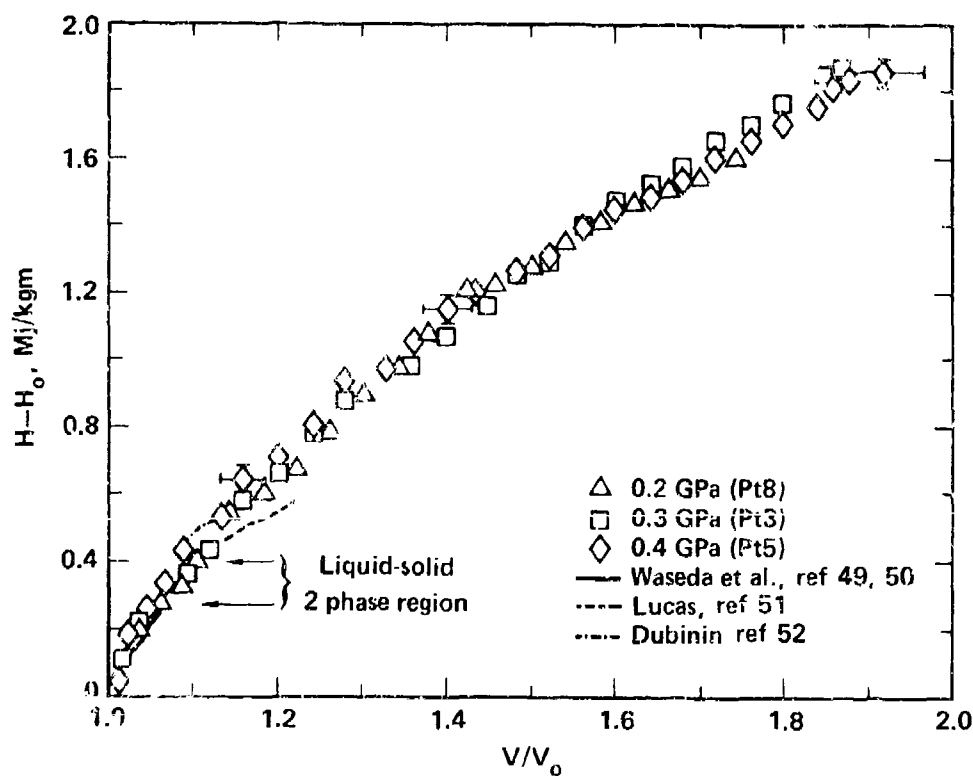


Fig. 21 Platinum Enthalpy vs Specific Volume

Data are for platinum at 0.2, 0.3 and 0.4 GPa with an estimate of the liquid solid 2-phase region deduced from Figs. 22 and 23. The vertical scale is referenced to 300 K and 0.1 MPa. Comparison is made to the work of Waseda, et al (49), Lucas (51), and Dubinin (52) with some discrepancy noted in the liquid state which was reached with some difficulty by the previous investigators.



retained. Expansions computed with Eq. (4-11) using temperatures taken from the enthalpy temperature tables of Hultgren<sup>(50)</sup> are also graphed in Figure 21. Waseda's measurements show platinum to be approximately 6% expanded at the beginning of melt which is reported by Hultgren to occur at an enthalpy of 0.273 MJ/Kgm. The beginning and end of melt are not readily discernible features of Figure 21, but can be identified approximately in the temperature data of Figure 22 and the resistivity data of Figure 23. Melt begins at an enthalpy of  $0.270 \pm 0.005$  MJ/Kgm and is completed by  $0.400 \pm 0.010$  MJ/Kgm yielding an enthalpy of melt of  $0.130 \pm 0.015$  MJ/Kgm which compares with Hultgren's prediction of 0.101 MJ/Kgm.<sup>(50)</sup> Corresponding volume expansions at the beginning and end of melt are  $1.06 \pm 0.005$  and  $1.10 \pm 0.01$ , respectively.

Also plotted in Figure 21 are the projections of Lucas<sup>(51)</sup> and Dubinin.<sup>(52)</sup> Lucas' expression for volume expansion is:

$$\frac{V}{V_0} = 1.1345 + 1.7374 \times 10^{-4} (T - 2042) \quad (4-12)$$

and is a fit to data taken at temperatures between 2042 K and 2200 K. The corresponding expression of Dubinin is:

$$\frac{V}{V_0} = [0.9217 - 1.1189 \times 10^{-4} (T - 2042)]^{-1} \quad (4-13)$$

and was determined by analyzing the configuration of sessile drops at temperatures from 2042 K to 2473 K. The use of Eq. (4-14) to convert from temperature to enthalpy produces the indicated points in Figure 21. The discrepancies between the measurements of Lucas and Dubinin and

Table 9  
Measured Properties of Platinum

Temperature K	$H-H(T_0, P)$ MJ/kgm	$\rho$ ( $\mu\Omega\text{m}$ )	$V/V_0$
2100	0.4661	1.028	1.12
2300	0.5180	1.052	1.14
2500	0.5679	1.076	1.15
2700	0.6178	1.099	1.17
2900	0.6677	1.122	1.19
3100	0.7176	1.144	1.21
3300	0.7675	1.167	1.23
3500	0.8174	1.190	1.26
3700	0.8674	1.214	1.28
3900	0.9173	1.239	1.30
4100	0.9672	1.264	1.33
4300	1.0171	1.291	1.35
4500	1.0670	1.320	1.38
4700	1.1169	1.350	1.41
4900	1.1668	1.383	1.43
5100	1.2167	1.418	1.46
5300	1.2666	1.455	1.49
5500	1.3165	1.496	1.52
5700	1.3664	1.539	1.55
5900	1.4163	1.586	1.58
6100	1.4662	1.636	1.62
6300	1.5161	1.690	1.65
6500	1.5660	1.748	1.68
6700	1.6160	1.800	1.72
6900	1.6659	1.877	1.75
7100	1.7158	1.949	1.79
7300	1.7657	2.025	1.83
7500	1.8156	2.107	1.86

$$V_0 = 0.047 \text{ cm}^3/\text{gm}$$

between each of theirs and ours is embodied in widely differing specific volumes at the end of melt. The relative volume at end of melt is found to be 1.1345 by Lucas, 1.085 by Dubinin, and  $1.10 \pm 0.01$  here. In each of these cases the slope of enthalpy versus  $V/V_0$  is roughly the same for the low temperature liquid region.

Platinum temperature measurements, made at pressures of 0.3 and 0.4 GPa, are plotted in Figure 22. Pyrometry channels were centered at nominal wavelengths of 450, 600, and 700 nm and sample radiation was sufficiently intense in all channels to produce distinct evidence of the melting transition. However, the low melting temperature ( $T_m = 2042$  K) caused the melting transition to occur near enough to minimum detector response to render the blue channel melting intensities too unreliable for calibration purposes. Therefore, the red channels are calibrated on melting point intensities and the blue channel is calibrated by attributing a later time intensity to a higher temperature as determined by red channel data (see Eq. 3-10). Sample radiation in almost all cases was bright enough to saturate the pyrometers at late times, resulting in abnormally large data scatter at temperatures above 6000 K. Error bars on Figure 22 are computed with Eq. A-1 assuming  $I_1/I_i = 10\%$  and  $G_1/G_i = 20\%$ . Because of these uncertainties in calibration and late time measurements the data are least squares fit to the linear function:

$$H = C_1 + C_2 T \quad (4-14)$$

$$C_1 = -5.5935 \times 10^{-2}$$

$$C_2 = 2.4954 \times 10^{-4}$$

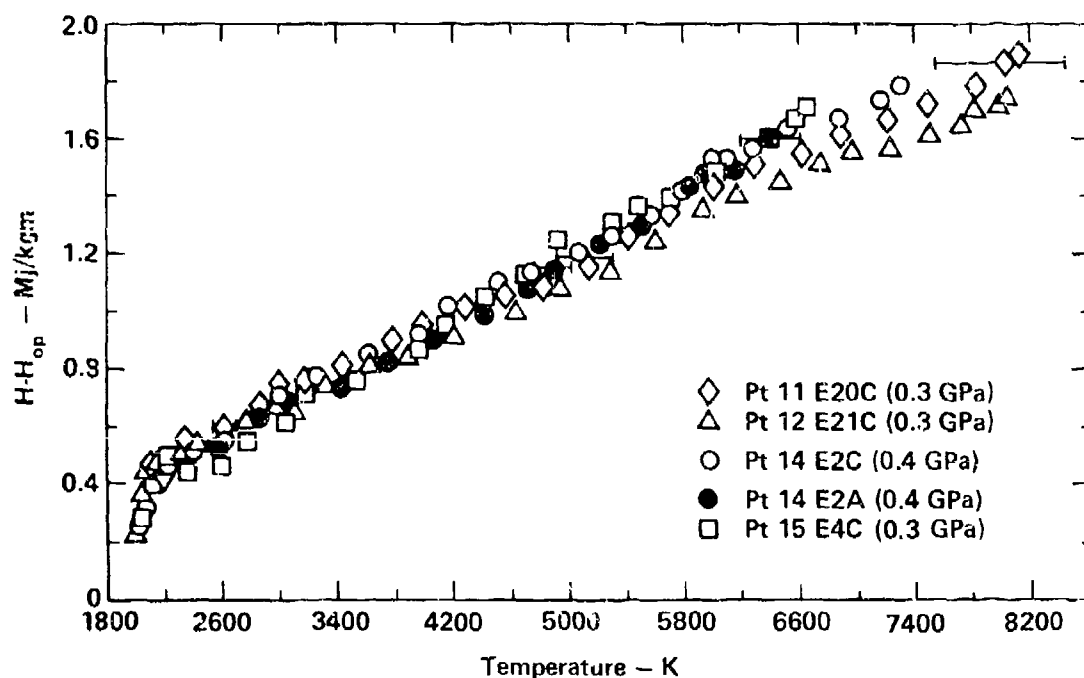


Fig. 22 Platinum Enthalpy vs Temperature  
 Platinum data are taken at 0.3 and 0.4 GPa. The vertical scale is enthalpy referenced to 300 K and 0.1 MPa while the horizontal scale is SCT temperature. Temperature values are derived from data taken at 450 and 700 nm.

over the entire liquid range from 2042 K to 8000 K.  $C_p$ , then, is a broadly averaged heat capacity of  $5.85 \pm 0.50R$ . This can be compared with the liquid heat capacities of other d electron transition metals such as molybdenum whose  $C_p$  is  $8.5R$ , tantalum having a  $C_p$  of  $8.3R$ , or tungsten having a  $C_p$  of  $6.2R$ .<sup>(53)</sup>

Figure 23 presents resistivities measured at 0.2, 0.3, and 0.4 GPa. The independent parameter of choice is enthalpy but could as well have been temperature or specific volume because there is no measured resolution among the platinum isobars as there is for lead. Enthalpy is referenced to the state at 298 K and the ambient cell pressure of each individual run, and is thus the enthalpy due to resistive heating only. A least squares fit of these data in the liquid phase yields the expression:

$$\rho = C_1 + C_2H + C_3H^2 + C_4H^3 \quad (4-15)$$

$$C_1 = 0.711749$$

$$C_2 = 0.921390$$

$$C_3 = -0.679053$$

$$C_4 = 0.327686$$

Use of Eq. (4-10b) for enthalpy versus volume in conjunction with Eq. (4-15) yields the fundamental volume dependence of platinum resistivity.

In an attempt to probe the liquid vapor coexistence region individual runs at 0.2, 0.3, and 0.4 GPa were carried to expansions at which the resistivity began to grow very quickly, i.e. the densities at which a

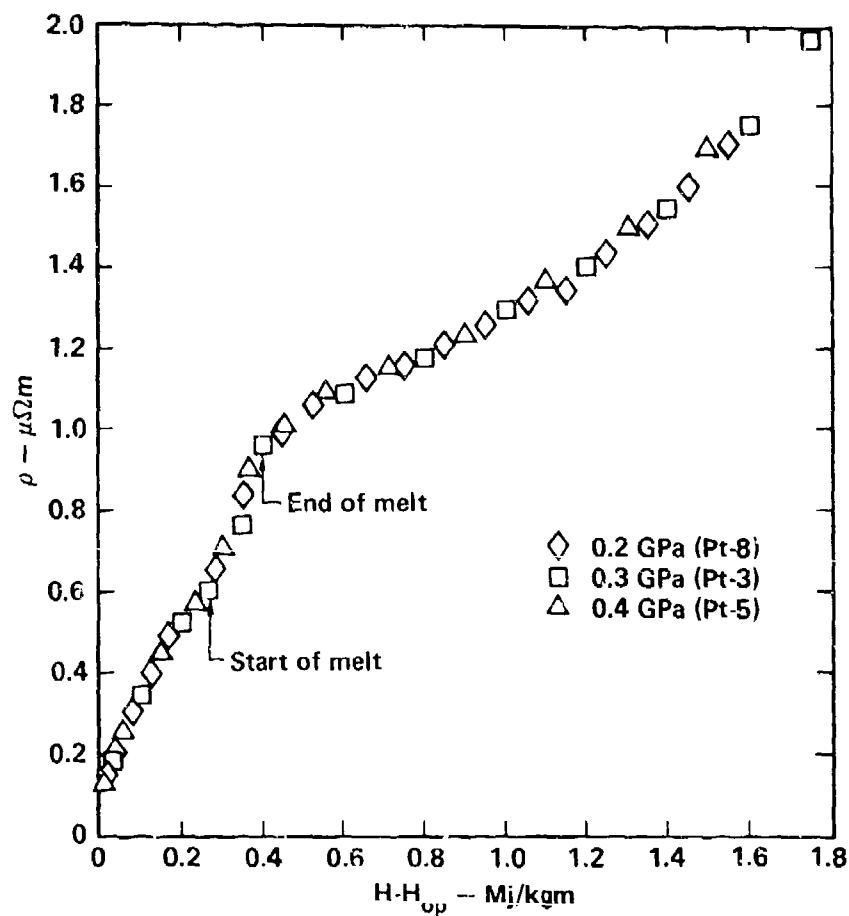


Fig. 23 Platinum Resistivity

The resistivity of platinum in  $\mu\Omega\text{m}$  is plotted as a function of enthalpy referenced to 300 K and cell pressure. No significant separation is observed among isobars at 0.2, 0.3 and 0.4 GPa. With reference to Fig. 21 similar agreement would be obtained for resistivities as a function of specific volume.

metal to insulator transition was observed to occur. Table 10 lists the parameters characteristic of that point on the individual isobars.

Table 10: Platinum Boiling Point

Pressure (GPa)	H (Mj/Kgm)	V/V <sub>0</sub>	$\rho$ ( $\mu\Omega\text{m}$ )
0.2	1.60	1.82	1.85
0.3	1.89	1.90	2.28
0.4	1.90	1.97	2.80

Enthalpy again is that added resistively. Platinum resistivities exhibit moderate increases with enthalpy until what is interpreted here as the boiling point is reached. At that point the resistivity versus enthalpy curve rises almost vertically making the enthalpy and the resistivity measurements somewhat uncertain. For this reason the relative volume parameter of Table 10 has to be regarded as the most reliable of the estimated boiling point parameters.

For pressures between 0.2 and 0.4 GPa the relative expansion at which boiling occurs appears to be only weakly dependent upon pressure, indicating that the slope of the liquid vapor coexistence curve in the pressure-specific volume plane is very steep (see Figure 2). This is interpreted to mean that 0.4 GPa is well below critical pressure since near the peak of the critical dome the coexistence curve must necessarily flatten out. Young and Alder use hard sphere van der Waals calculations to project a platinum critical pressure of 1.05 GPa.<sup>(4)</sup> Subsequent soft sphere calculations have reduced the original hard sphere predictions by significant amounts for other d-electron transition

metals.<sup>(5)</sup> Although no soft sphere calculations are available for platinum by analogy one could logically assume that the critical pressure of platinum might be between 0.5 and 0.6 GPa. The data of this work are consistent with that prediction.

#### Gold-Copper

Several data runs were made on an alloy of gold and copper at pressures of 0.2, 0.3, and 0.4 GPa. From a basic science point of view investigations of pure gold and pure copper would have been preferable, but the pure materials were thought to be too difficult to heat resistively because of low normal state resistivities. The resistivity of gold is  $0.022 \mu\Omega\text{m}$  and that of copper is  $0.017 \mu\Omega\text{m}$ <sup>(54)</sup> at 295 K while the alloy has resistivities of 0.0732 and 0.070  $\mu\Omega\text{m}$  in the cold drawn and annealed forms, respectively. The alloy chosen is 95% by weight or 85% by mole gold, the rest being copper. It is a common material noted for its combined characteristics of strength and resistance to hydrogen embrittlement. It is hoped that, although the transport properties are strongly a function of the alloying, the measured equation of state parameters will bear some close relationship to those of pure gold.

Non-annealed gold-copper resistivities measured at 0.2, 0.3 and 0.4 GPa are plotted in Figure 24. The melting transition is less distinctly identifiable than it is for many pure metals but is interpreted as beginning at approximately  $0.14 \pm 0.02 \text{ MJ/Kgm}$  and ending at  $0.21 \pm 0.01 \text{ MJ/Kgm}$  for a total transition enthalpy deposition of  $0.07 \pm 0.03 \text{ MJ/Kgm}$ . Although not completely equivalent this can be compared to the enthalpy of melt of pure gold which is  $0.064 \pm 0.002 \text{ MJ/Kgm}$ .<sup>(55)</sup> Pure gold melts at 1337.56 K yielding an entropy of melt of  $4.79 \pm 0.15 \times 10^{-5}$



Mj/Kgm for a total transition enthalpy deposition of  $0.07 \pm 0.03$  MJ/Kgm. Although not completely equivalent this can be compared to the enthalpy of melt of pure gold which is  $0.064 \pm 0.002$  MJ/Kgm.<sup>(55)</sup> Pure gold melts at 1337.58 K yielding an entropy of melt of  $4.79 \pm 0.15 \times 10^{-5}$  MJ/Kgm K. For the rapid heating rates of this experiment the alloy is assumed to melt at constant composition but varying temperature. With reference to Hansen's phase diagram the alloy begins melt at 1248 K and ends melt at 1278 K.<sup>(56)</sup> Using an intermediate temperature of 1263 K the transitional entropy for the alloy is  $5.5 \pm 2.4 \times 10^{-5}$  MJ/Kgm-K. If the large confidence interval is ignored the alloy is observed to have a higher transitional entropy than the pure gold, as might be expected.

The resistivity of the alloy does not grow as rapidly as a function of enthalpy as the resistivities of the other metals of this work. At the beginning of melt the Au-Cu resistivity has barely reached  $0.15 \mu\Omega\text{m}$  as compared to the  $0.60 \mu\Omega\text{m}$  value for platinum at a similar point (see Figure 23). Both lead and platinum resistivities are in the neighborhood of  $1.00 \mu\Omega\text{m}$  at the end of melt while that for Au-Cu is a factor of three down. The conductivity of Au-Cu remains very high throughout the liquid region as does the thermal conductivity by Wiedemann-Franz law reasoning. The liquid state resistivities are least squares fit by Eq. (4-16) and representative values listed in Table 11. Enthalpies are

$$\rho = C_1 + C_2 H + C_3 H^2 \quad (4-16)$$

$$C_1 = 0.24382$$

$$C_2 = 0.212790$$

$$C_3 = 0.910419$$

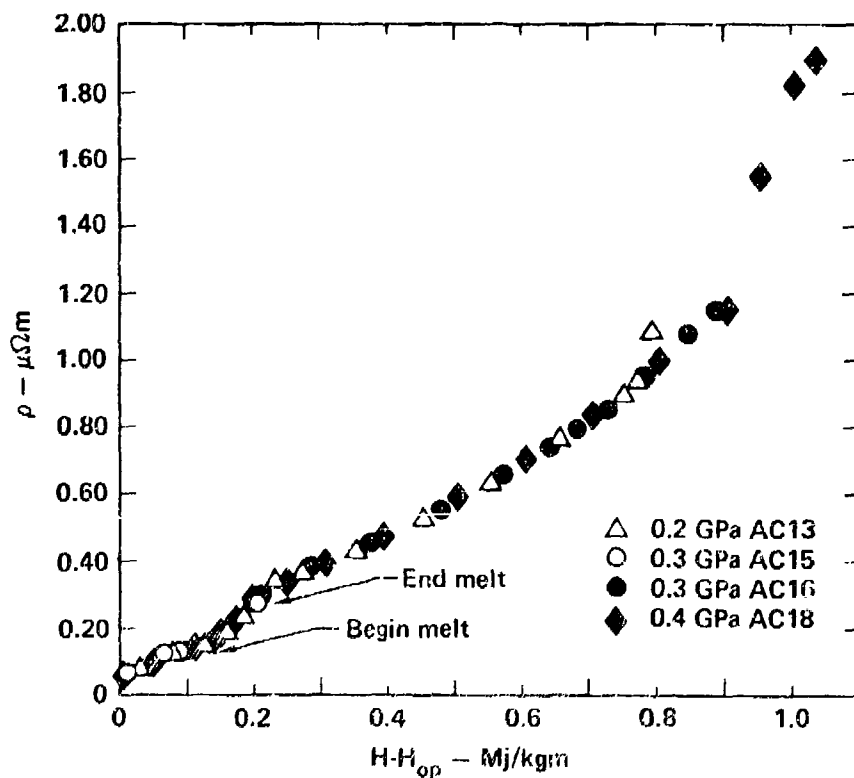


Fig. 24 Gold-Copper Resistivity

The resistivity of gold-copper in  $\mu\Omega\text{m}$  is displayed as a function of enthalpy referenced to 300 K and cell pressure. No significant separation is observed among isobars at 0.2, 0.3 and 0.4 GPa. Sporadic and inconsistent resistivities are recorded for enthalpy depositions above 0.9 MJ/kgm which could be indicative of imperfect voltage probe contact or nearness to the liquid vapor two phase region. The melting transition for this alloy is less distinctly identifiable than it is for single constituent metals.

referenced to 298 K and the cell pressure of a given run and are thus the enthalpies added electrically.

Temperature measurements on the alloy proved very difficult to make consistent for reasons that are not completely understood. Experimental problems arose with a suspected unstable pyrometer baseline while computations proved sensitive to a necessarily indirect calibration technique. Figure 25 is a plot of enthalpy versus temperature for six different runs, the temperature being based upon channels centered at 600, 700, and 900 nm. Several of the data tracks plotted exhibit a sharp upward turn at relatively modest temperatures (detector voltages) while others display a downward dip near minimum detector response. Both of these unphysical characteristics are quite evident in the trace labelled AC8E31BA, in which the temperatures are derived from the 700 nm channel of a 0.20 GPa run. The abnormal initial droop and the later time upturn are thought not to be a function of wavelength nor pressure nor any real effect of the sample, but evidence of electronic instability in the pyrometers. The pyrometers rely on a battery arrangement to maintain a noise-free, stable baseline.<sup>(12)</sup> In retrospect the state of charge of the pyrometer batteries appears to have been marginal for many of the gold-copper data runs. Only the run AC19E32CB was made at a time when the batteries were relatively freshly charged. Data of this run define a line of most confident temperatures and are least squares fit as given in Eq. (4-17) with representative values listed in Table 11.

$$H = C_1 + C_2T + C_3T^2 + C_4T^3 + C_5T^4 + C_6T^5 \quad (4-17)$$

$$C_1 = -1.3517$$

$$C_4 = 1.9526 \times 10^{-10}$$

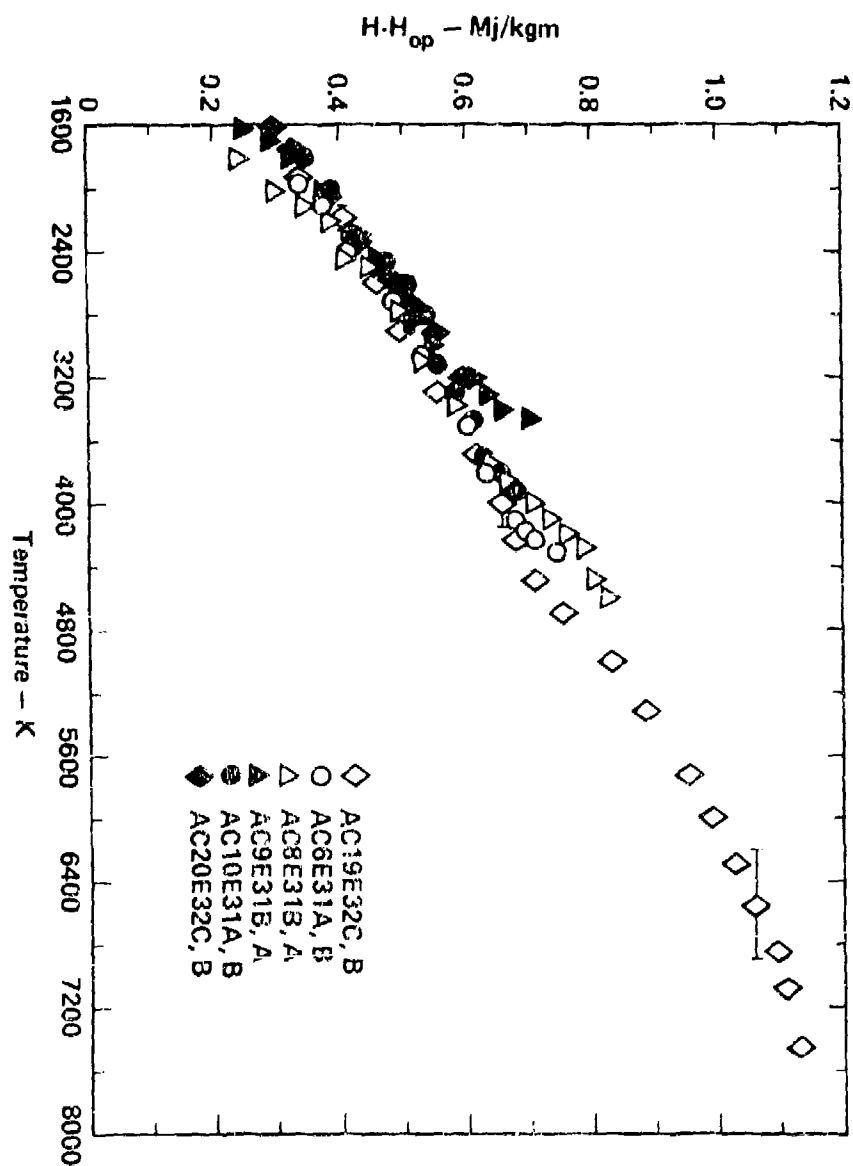


Fig. 25 Gold-Copper Enthalpy vs Temperature  
 Gold-copper pyrometric data taken at 0.2 and 0.3 GPa. Scales are temperature  
 K horizontal and specific enthalpy referenced to 300 K and cell preasure  
 vertical. Trace end excursions are believed to be the result of weak stabilizing  
 voltage in the pyrometers.

Table 11  
Measured Properties of Gold-Copper

T(K)	H-H(T <sub>0</sub> , P) Mj/kgm	$\rho(\mu\Omega\text{m})$	V/V <sub>0</sub>
2000	0.3648	0.443	1.18
2200	0.4061	0.480	1.20
2400	0.4398	0.514	1.22
2600	0.4685	0.543	1.24
2800	0.4941	0.571	1.26
3000	0.5182	0.599	1.27
3200	0.5421	0.627	1.29
3400	0.5668	0.657	1.31
3600	0.5929	0.690	1.32
3800	0.6208	0.727	1.34
4000	0.6508	0.768	1.36
4200	0.6826	0.813	1.38
4400	0.7163	0.863	1.40
4600	0.7514	0.918	1.43
4800	0.7874	0.976	1.45
5000	0.8238	1.037	1.47
5200	0.8601	1.100	1.49
5400	0.8957	1.165	1.51
5600	0.9300	1.229	1.53
5800	0.9623		1.55
6000	0.9924		1.57
6200	1.0197		1.58
6400	1.0442		1.60
6600	1.0658		
6800	1.0845		
7000	1.1007		
7200	1.1151		

$$V_0 = 0.055 \text{ cm}^3/\text{gm}$$

$$C_2 = 1.9810 \times 10^{-3}$$

$$C_5 = 2.0312 \times 10^{-14}$$

$$C_3 = -8.7698 \times 10^{-7}$$

$$C_6 = 7.9449 \times 10^{-19}$$

The fifth order fit is chosen as the lowest order expression that shadows a dip in the heat capacity observed in the oscilloscope record of the pyrometric response. The accuracy of the data suggests a linear fit as entirely suitable. The indicated uncertainty intervals are calculated using Eq. (A-1) with a variable estimate for  $\Delta I_i/I_i$ . As in Figure 24 the enthalpy of Figure 25 and Eq. (4-17) is that added to the sample through resistive heating. Calibration was accomplished by associating the enthalpy needed to reach the end of melt as identified in Figure 24 with a sample temperature of 1278 K. From this base point below minimum detector response a constant heat capacity was used to extrapolate to a measured enthalpy corresponding to an intensity strong enough to be measured with some precision. For run AC19 the base enthalpy was found to be 0.22 MJ/Kgm. A constant heat capacity of  $1.672 \times 10^{-4}$  MJ/Kgm-K was used to establish a calibration point at 2600 K and 0.44 MJ/Kgm. The heat capacity choice was dictated by matching the slope of the enthalpy-temperature curve at the low temperature end and was necessarily an iterative process. It should be emphasized that this technique carried with it accuracy problems inherent in extrapolating over 1000 K which are, however, adequately represented by the graphed error bars. The large electronically caused systematic off-sets are not completely accommodated by the error bars.

Figure 26 displays enthalpy-specific volume data of the 0.2, 0.3, and 0.4 GPa isobars for the gold-copper alloy. Enthalpy is referenced to 298

K and 0.1 MPa and thus includes components due to pressurization and resistive heating. Enthalpies of compression are 0.0109, 0.0163, and 0.0218 MJ/Kgm at 0.2, 0.3, and 0.4 GPa, respectively, and are computed from the expression  $\Delta H = (1-\alpha T) V_0 \delta P$  where  $\alpha = 42.3 \times 10^{-6} \text{ K}^{-1}$ . (57)

Expected resolution of the isobars is far less than experimental uncertainty and, in fact, no consistent separation is observed. In each of the runs of Figure 26 expansion was carried to the point where the samples became non-conducting, although at this limit sample resistivities and to a lesser extent densities exhibited an unstable oscillatory behavior. The diameter fluctuations were not pronounced enough to be easily detected with the late time ruby snapshot. However, the resistivities indicated the sample to be passing back and forth between highly resistive and moderately conductive states. The first sharp upturn of resistivity occurred at enthalpies of 0.88, 1.15 and 0.97 MJ/Kgm for the 0.2, 0.3 and 0.4 GPa runs, respectively. The uncertain behavior of the samples near maximum expansion makes identification of the boundary of the liquid vapor two phase region impossible and casts doubt on the validity of the data beyond  $V/V_0 = 1.6$ . A second order least squares fit of these data is:

$$H = C_1 + C_2 \left( \frac{V}{V_0} \right) + C_3 \left( \frac{V}{V_0} \right)^2 \quad (4-18)$$

$$C_1 = -2.0681$$

$$C_2 = 2.4088$$

$$C_3 = -0.29781$$

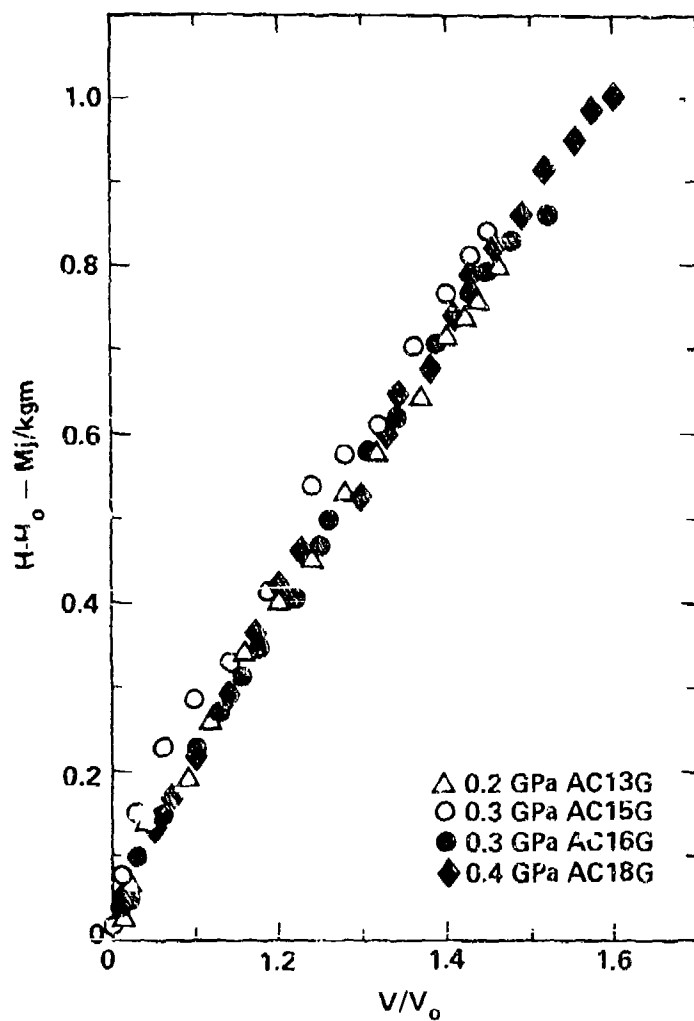


Fig. 26 Gold-Copper Enthalpy vs Specific Volume

Gold-copper data taken at 0.2, 0.3 and 0.4 GPa. The horizontal scale is the specific volume normalized to  $V_0 = 0.055 \text{ cm}^3/\text{gm}$ , and the vertical scale is specific enthalpy referenced to 300 K and 0.1 MPa. No systematic separation among the isobars is observed.



and representative values are listed in Table 11. A comparison of Figs. 24 and 26 indicates that the melting transition occurs at expansions between 1.05 and 1.10.

### Uranium

Uranium temperature data have been analyzed for three separate 0.2 GPa runs labelled here U80, U83, and U85. For purposes of determining the emissivity of uranium, tantalum calibration runs were made in conjunction with U80 and U85, and are here designated Ta58 and Ta61, respectively. These uranium data were used as a test case to compare the temperature determining technique discussed up to this point with a second technique based upon choosing a constant emissivity for each channel that affords best agreement among the applicable SCT and TCT temperatures. The second method, for reference purposes called the constant emissivity method, rests upon evaluating the unknown calibration factor,  $G_i$ , for each channel through use of a tantalum calibration run. Specifically Eq. (3-10) is applied to the measured intensity at the tantalum melting plateau with a known tantalum emissivity. (36)

$$G_i = \frac{I'_i(T_m)}{\epsilon'(\lambda_i, T_m) F_i(T_m)} \quad (4-19)$$

Primes refer to quantities associated with the tantalum standard and  $T_m$  is the tantalum melting temperature assumed to be its one atmosphere value of 3270 K. Substitution of Eq. (4-19) into Eq. (3-8) yields the following expression for the SCT temperature:

$$I_i(T) = \frac{I_1'(T_m) \epsilon(\lambda_i, T) F_i(T)}{\epsilon(\lambda_i, T_m) F_i(T_m)} \quad (4-20)$$

where the sample emissivity  $\epsilon(\lambda_i, T)$  is the only unknown parameter. Application of Eqs. (3-8) and (4-19) to individual channels designated  $i$  and  $j$ , and a small amount of algebraic manipulation, produces an expression for the TCT temperatures that is analogous to Eq. (3-13).

$$\frac{I_i(T)}{I_j(T)} = \frac{\epsilon(\lambda_j, T_m) I_1'(T_m) F_j(T_m) \epsilon(\lambda_i, T) F_i(T)}{\epsilon(\lambda_i, T_m) I_j'(T_m) F_i(T_m) \epsilon(\lambda_j, T) F_j(T)} \quad (4-21)$$

As with Eqs. (3-12) and (3-13) two channels of pyrometry data enable the determination of two SCT temperatures with Eq. (4-20) and one TCT temperature with Eq. (4-21). In practice the unknown sample emissivities  $\epsilon(\lambda_i, T)$  and  $\epsilon(\lambda_j, T)$  were assumed independent of temperature and chosen to bring best agreement among the SCT and TCT temperatures for the entire experimental run. It is important to remember that all measured intensities represented in Eqs. (4-20) and (4-21) are actually intensities relative to a calibration intensity  $I_0$ . For this reason both the tantalum standard and the data run must use the same pyrometer voltage to intensity transfer function (see Figure 14).

Figure 27 illustrates the full range agreement achieved with the choice of emissivities listed in Table 12. For the pyrometric windows of this study the temperatures are only a weak function of the emissivity. It is felt that the fact that the emissivities calculated are of the right order of magnitude represents a positive result. No special meaning should be attached to the precise values nor the relative magnitudes among the channels. The significant conclusion is that the

choice of a reasonable set of emissivities results in close agreement among the SCT temperatures over the full range of temperatures reached in the experiment.

A similar computation was done with the data of run U85. The SCT temperatures calculated exhibited agreement as close as that shown for run U80, and the emissivities necessary to achieve that agreement are listed in Table 13. Within the precision of the calculation the emissivities of Table 13 are consistent with those of Table 12. Stephen's calculates an emissivity of  $0.32 \pm 0.01$  at 650 nm by measuring the radiance temperature at the melting point.<sup>(58)</sup> He then assumes this emissivity to be valid for a temperature range of 1406 to 2350 K.

---

Table 12: Uranium Emissivities Derived from Run U80

$\lambda$	$\epsilon_{Ta}(\lambda_i)^{(36)}$	$\epsilon_{UR}(\lambda_i)$
450	0.40	0.25
600	0.38	0.48
650	0.37	0.37

---

Table 13: Uranium Emissivities Derived from Run U85

$\lambda_i$	$\epsilon_{Ta}(\lambda_i)$	$\epsilon_{UR}(\lambda_i)$
450	0.40	0.44
700	0.37	0.35
900	0.35	0.35

---

To provide a direct comparison of the constant emissivity tantalum calibration method with the method that assumes a linear temperature

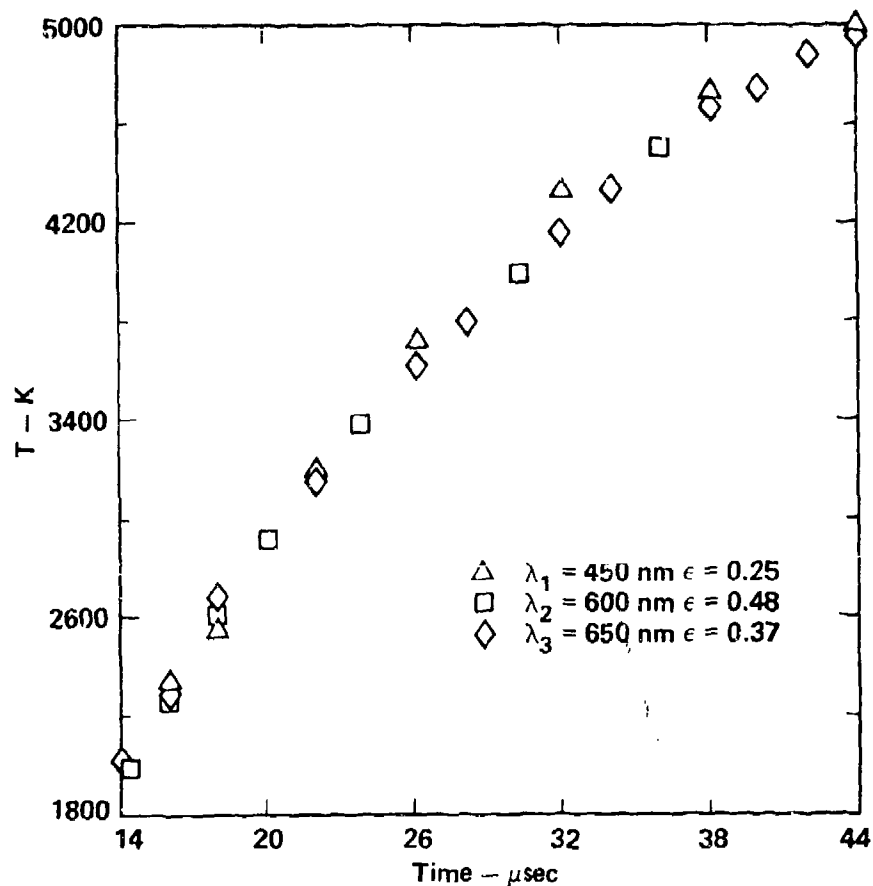


Fig. 27 Uranium SCT Temperatures Calculated with Constant Emissivities

Single channel temperatures are derived from data taken at 450, 600, and 650 nm using constant emissivities of 0.25, 0.48, and 0.37, respectively. Calibration is accomplished by using a separate tantalum calibration run in a manner outlined by Eqs. (4-19) and (4-20). Full range close agreement is obtained with this choice of temperature independent reasonable magnitude emissivities.

dependence, Eqs. (3-12) and (3-13) were applied to the data from the two red channels of run U80. The agreement among the three temperatures is illustrated in Figure 28. The necessary tie point was  $T = 2800$  K and  $H = 0.529$  MJ/Kgm and was chosen by extrapolating Stephens data with a constant  $C_p$ .<sup>(58)</sup> The  $C_p$  was selected as a compromise between Stephens value,  $C_p = 2.04 \pm 0.5 \times 10^{-4}$  MJ/Kgm-K ( $11.6 \pm 0.3$  cal/mole K), and one that matches the low temperature end of the current liquid data,  $C_p = 2.23 \times 10^{-4}$  MJ/Kgm-K ( $12.7$  cal/mole-K). Although the emissivities are not a direct result of the tie point method it is possible to find them through a comparison of the data with its associated tantalum run. An outline of this calculation and the results are presented as Table 14 and Table 15 for runs U80 and U85, respectively. In view of the many arithmetic operations involving uncertain quantities the agreement among the uranium emissivities found in each of the data runs and published by Stephens is excellent. Blue channel ( $\lambda = 450$  nm) data were not used because the low intensities at the tie point were believed to be noise dominated, and did not provide an adequate calibration. The overall temperature dependence of the emissivity is seen to be very slight and may just be compensating for inherent inaccuracies in the measurement and calibration procedures.

Figure 29 presents the enthalpy versus temperature data for runs U80 and U85. Error bars are calculated using Eq. (A-1) with  $\Delta G_i/G_i = 10\%$  and  $\Delta I_i/I_i = 10\%$  for low temperatures and  $5\%$  for higher temperatures. Stephen's data taken at  $0.1$  MPa is plotted also and is least squares fit for the temperature range of  $1407$  K to  $2348$  K by the following expression:<sup>(58)</sup>

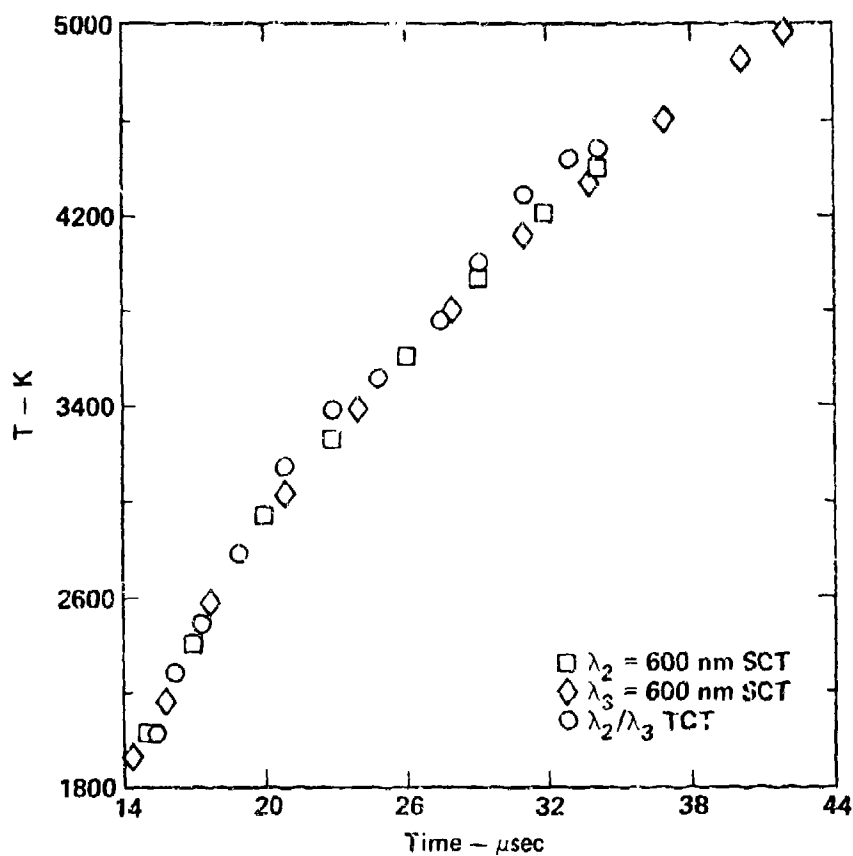


Fig. 28 Uranium Temperatures Calculated with Temperature Dependent Emissivities  
 SCT temperatures derived from data taken at 600 and 650 nm and TCT temperatures deduced from the ratio of the intensities of these two channels show close agreement over the full temperature range. Temperatures are calculated with linearly dependent emissivities and are calibrated to a tiepoint at 2800 K and 0.529 Mj/kgm extrapolated from Stephens data. (58) Emissivity for the 600 nm channel varies between 0.37 and 0.44 while remaining constant at 0.32 for the 650 nm channel.

Table 14  
U80 Emissivity Determination

Chan	$\lambda_i$	$G_i \epsilon_{UR}(\lambda_i, T_{TP})$	$G_i \epsilon_{UR}(\lambda_i, T_m)$	$I_{iTa}(\lambda_i, T_m)$	$G_i \epsilon_{Ta}(\lambda_i, T_m)$ $= \frac{I_{iTa}(T_m)}{F(\lambda_i, T_m)}$
1	450	$2.21 \times 10^{-3}$			
2	600	$5.70 \times 10^{-3}$	$5.86 \times 10^{-3}$	$6.20 \times 10^{-2}$	$5.558 \times 10^{-3}$
3	650	$5.05 \times 10^{-3}$	$5.05 \times 10^{-3}$	$1.2 \times 10^{-1}$	$5.83 \times 10^{-3}$

Chan	$\epsilon_{Ta}(\lambda_i, T_m)$	$G_i$	$\epsilon_{UR}(\lambda_i, T_m)$	$\epsilon_{UR}(\lambda_i, 2500)$ $-\epsilon_{UR}(\lambda_i, 5500)$
1	0.40			
2	0.38	$1.46 \times 10^{-2}$	$0.39 \pm 0.05$	$0.37-0.44$
3	0.37	$1.576 \times 10^{-2}$	$0.32 \pm 0.05$	$0.32-0.32$

Tie Point Calculation

$$T_{TP} = 2800 \text{ K}$$

$$H_{TP} = 0.529 \text{ MJ/Kgm}$$

$$T_m = 3270 \text{ K}$$

Table 15  
U85 Emissivity Determination

Chan	$\lambda_i$	$G_i \epsilon_{UR}(\lambda_i, T_{TP})$	$G_i \epsilon_{UR}(\lambda_i, T_m)$	$I_{iTa}(\lambda_i, T_m)$	$G_{iTa}(\lambda_i, T_m)$ $= \frac{I_{iTa}(T_m)}{F(\lambda_i, T_m)}$
1	450	$7.258 \times 10^{-4}$			
2	700	$1.334 \times 10^{-3}$	$1.348 \times 10^{-3}$	$3.0 \times 10^{-2}$	$1.513 \times 10^{-3}$
3	900	$1.535 \times 10^{-3}$	$1.595 \times 10^{-3}$	$4.1 \times 10^{-3}$	$1.810 \times 10^{-3}$

Chan	$\epsilon_{Ta}(\lambda_i, T_m)$	$G_i$	$\epsilon_{UR}(\lambda_i, T_m)$	$\epsilon_{UR}(\lambda_i, 2500)$ $= \epsilon_{UR}(\lambda_i, 5500)$
1	0.40			
2	0.37	$4.089 \times 10^{-3}$	$0.330 \pm 0.05$	$0.327 - 0.338$
3	0.35	$5.171 \times 10^{-3}$	$0.309 \pm 0.05$	$0.296 - 0.348$

Tie Point Calculation

$$T_{TP} = 2600 \text{ K}$$

$$H_{TP} = 0.488 \text{ MJ/Kgm}$$

$$T_m = 3270 \text{ K}$$



$$H = 0.2449 + 2.039 \times 10^{-4} (T - 1407) \quad (4-22)$$

The current data are fit with the following least squares expression:

$$H = -0.2337 + 2.8813 \times 10^{-4} T \quad (4-23)$$

The enthalpy of Eq. (4-22) is referenced to 0.1 MPa and 298 K while the enthalpy of Eq. (4-23) is referenced to 0.2 GPa and 298 K. A linear fit of the data forces the heat capacity,  $2.8813 \times 10^{-4}$  MJ/kgm K, to be larger than Stephen's heat capacity and the heat capacity used to extrapolate Stephen's data to a temperature tie point. The current data suggests that a lower  $C_p$  is appropriate to approximately 3100 K but that a higher heat capacity better characterizes the material above 3100 K. To illustrate once again the problem with extrapolating  $C_p$ 's measured at lower temperatures to the high temperatures of the current work Stephens  $C_p$  is used to extend his data to 5000 K as illustrated in Figure 29.

Figure 30 is a plot of the volume enthalpy data of two recent runs made on uranium.<sup>(59)</sup> Enthalpy is referenced to 298 K and 0.1 MPa and thus includes an enthalpy of cold compression given by  $\Delta H = V_0 (1 - \alpha T) \Delta P$  where  $\alpha$ , the volume thermal expansion coefficient, is  $3.78 \times 10^{-6}$ .<sup>(35)</sup>  $\Delta H$  is 0.0104 MJ/kgm and 0.0208 MJ/kgm for the 0.2 GPa and 0.4 GPa data, respectively. The data are least squares fit by the following expression:

$$H = -3.2589 + 4.2589 \left( \frac{V}{V_0} \right) - 0.9550 \left( \frac{V}{V_0} \right)^2 \quad (4-24)$$

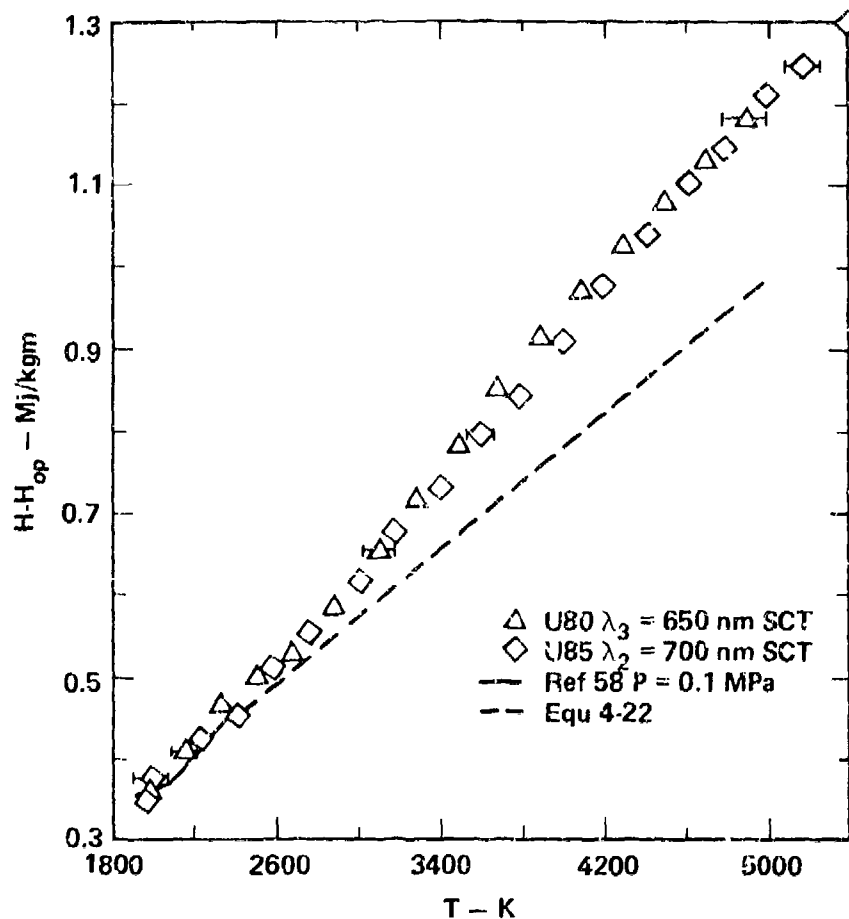


Fig. 29 Uranium Enthalpy vs Temperature

Uranium data taken at 0.2 GPa. The vertical scale is specific enthalpy referenced to 300 K and cell pressure while the horizontal scale is temperature in degrees K. Temperatures are derived from data recorded in the 650 and 700 nm channels and are computed with temperature dependent emissivities. The measurements of Stephens are shown for comparison and extrapolated with constant heat capacity to the high temperatures of this work. (58)

Also plotted in Figure 30 for comparison purposes are 0.1 MPa data. Solid state specific volumes are those of Touloukian<sup>(60)</sup> using Hultgren tables to convert temperature to enthalpy.<sup>(61)</sup> Liquid state specific volumes are those of Rohr and Wittenberg<sup>(62)</sup> with Stephen's expressions used for conversion to enthalpy.<sup>(58)</sup> There appears to be a systematic displacement to higher enthalpies for the data of this work that cannot be explained by the enthalpy of compression. Further there is no resolution beyond experimental inaccuracies between the 0.2 and 0.4 GPa data which would indicate that none should be expected between the 0.1 MPa and higher pressure data. Because the discrepancy increases as the temperature goes up it is reasonable to assume that the inherent problems of the static measurement at high temperature might be the cause of the off-set. The inverse relation of Eq. (4-24) is given in Eq. (4-25) and has been used along with Eqs. (4-23) to produce the values listed in the first part of Table 16.

$$\frac{V}{V_0} = 0.9885 + 0.3398 H + 0.1964 H^2 \quad (4-25)$$

Figure 31 presents uranium resistivity measurements made at pressures of 0.2 and 0.4 GPa. Enthalpy plotted is that due to resistive heating only. The resistivities measured in ref. 13 are shown for comparison and are systematically higher than those of the current work. A shift to higher resistivities is consistent with the shift toward higher volumes necessary to bring the data of Figure 30 into line with static data. However, the magnitude of the required change in resistivity would leave it very close to the measurements depicted. The accuracy of the current

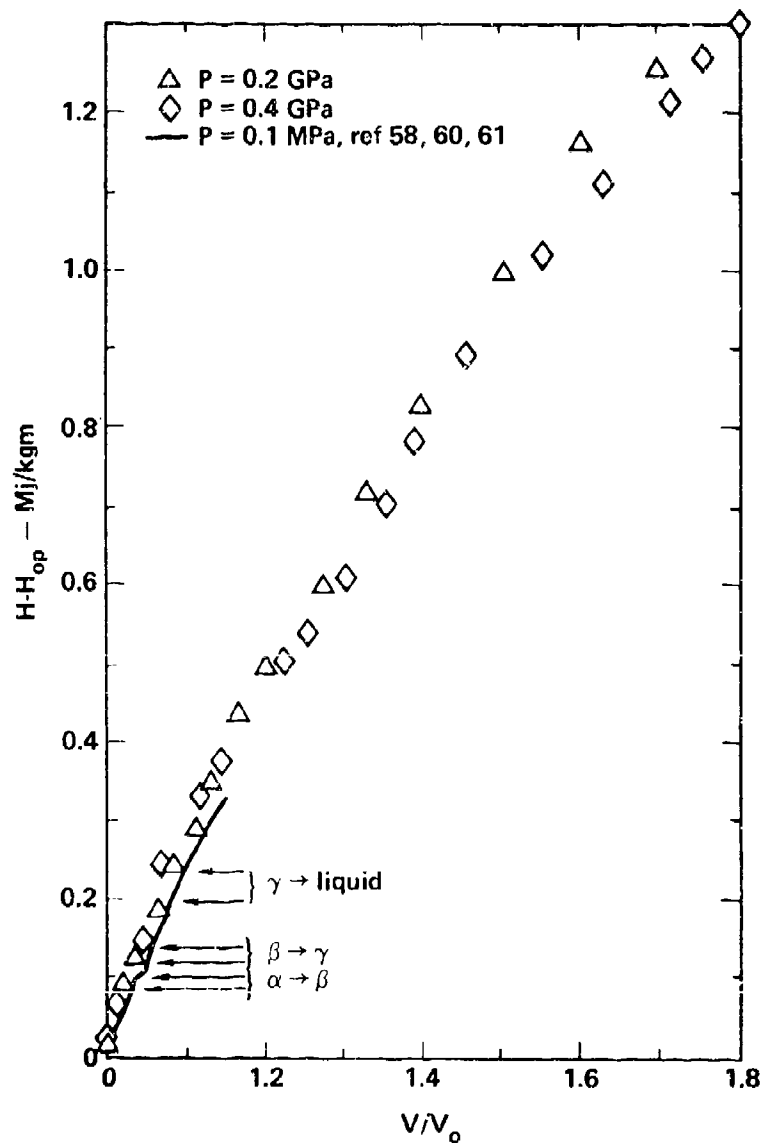


Fig. 30 Uranium Enthalpy vs Volume

Uranium expansion data taken at 0.2 and 0.4 GPa. The vertical scale is specific enthalpy referenced to 300 K and cell pressure while the horizontal scale is volume relative to an initial specific volume of  $0.052 \text{ cm}^3/\text{gm}$ . Stephen's data <sup>(58)</sup> are plotted for comparison with the tables of Touloukian <sup>(60)</sup> and Hultgren <sup>(61)</sup> used for conversion from temperature to enthalpy. The data of this work exhibit a consistent offset to higher enthalpy.

work can be considered to be better than that of ref. 13 because of improvements in the streak photography technique. A least squares fit of the liquid state resistivities is:

$$\rho = 0.3424 + 1.3310 H - 1.1426 H^2 + 0.6602 H^3 \quad (4-26)$$

Resistivity as a function of  $V/V_0$  can be obtained through successive application of Eqs. (4-24) and (4-26) and will be discussed in Chapter 5.

Table 16 presents the measured liquid uranium properties as described by Eqs. (4-23), (4-25), and (4-26). Enthalpy considered is referenced to cell pressure and 298 K for columns one, two, and four. However the enthalpy considered in calculating specific volume is referenced to 0.1 MPa and 298 K. For temperatures below detector response Stephen's enthalpy temperature relationship is used. (58)

### Niobium

Extensive niobium pyrometry data were taken at 0.3 GPa in order to corroborate results published in ref. 15 and to extend the range of temperature measurement above 4000 K. Detector windows were set at nominal wavelengths of 450, 650, and 900 nm. As shown in Figure 32 the two longer wavelength channels provide an opportunity to calculate TCT temperatures with better than the usual precision. This is the result of the calibration temperature's being high enough to produce significant and precisely measurable intensity at the two longer wavelengths yet having sufficient spread between the channels to cause the intensity ratio to be sensitive to temperature (see Eq. 3-13). Graphed confidence intervals are computed from Eqs. (A-1) and (A-4) using intensity

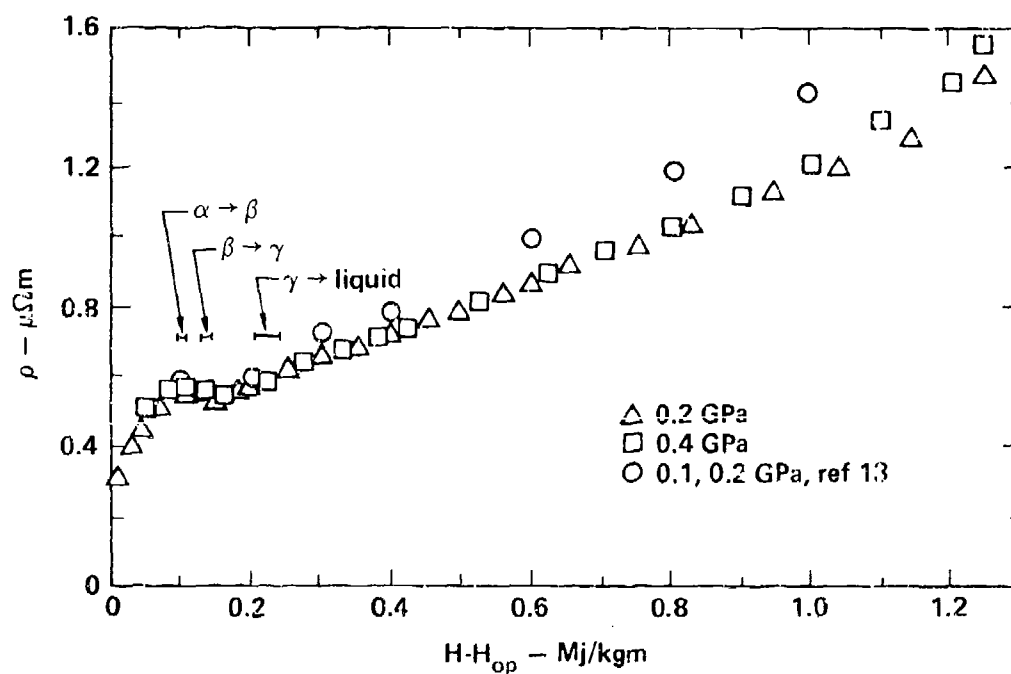


Fig. 31 Uranium Resistivity vs Enthalpy

Uranium resistivity data taken at 0.2 and 0.4 GPa. The horizontal scale is enthalpy relative to 300 K and cell pressure while the vertical scale is resistivity in  $\mu\Omega\text{m}$ . Indicated phase transitions are taken from Hultgren<sup>(61)</sup>, and previous measurements of Shaner, et al<sup>(13)</sup> are plotted for comparison.

Table 16  
Measured Properties of Liquid Uranium

T(K)	H-H(T <sub>0</sub> ,P)	V/V <sub>0</sub>	ρ (μΩm)
1407	0.2420*	1.081	0.6073
1600	0.2843*	1.101	0.6440
1800	0.3250*	1.120	0.6774
2000	0.3426	1.128	0.6912
2200	0.4002	1.156	0.7348
2400	0.4578	1.185	0.7760
2600	0.5154	1.216	0.8157
2800	0.5731	1.248	0.8546
3000	0.6307	1.281	0.8934
3200	0.6883	1.315	0.9329
3400	0.7459	1.351	0.9739
3600	0.8036	1.388	1.0171
3800	0.8612	1.427	1.0633
4000	0.9188	1.466	1.1132
4200	0.9764	1.507	1.1677
4400	1.0341	1.550	1.227
4600	1.0917	1.594	1.293
4800	1.1493	1.638	1.366
5000	1.2070	1.685	1.446
5200	1.2646	1.732	1.534
5400	1.3222	1.781	1.631

\*Ref. 58

$$V_0 = 0.052 \text{ cm}^3/\text{gm}$$

uncertainties of 5% in mid-range and 10% at the extremes. Calibration is accomplished by assigning a temperature of 2741 K to the prominent melting plateau. The emissivities necessary to reach the agreement illustrated varied 20% over the full temperature range for the 650 nm channel and not at all for the 900 nm channel. Cezairliyan reports a radiance temperature of 2425 K at the melting plateau for  $\lambda = 650$  nm which, when compared to a true temperature of 2750 K, yields an emissivity at melt of 0.340.<sup>(63)</sup> The present calculation, then, yields an emissivity varying between 0.32 and 0.39. A variation of this magnitude may be numerical artifact introduced by imprecision in measuring the melting point intensity.

Figure 33 is a plot of measured enthalpies, referenced to cell pressure, versus the SCT temperatures deduced from the longer wavelength channels of two separate runs. Earlier data are plotted to demonstrate the consistency of the measurements.<sup>(15)</sup> Liquid state points can be represented by the following least squares fit:

$$H = C_1 + C_2T + C_3T^2 \quad (4-27)$$

$$C_1 = 4.0783 \times 10^{-3}$$

$$C_2 = 2.9706 \times 10^{-4}$$

$$C_3 = 4.1968 \times 10^{-8}$$

The liquid state specific heat is then approximately  $5.321 \times 10^{-4}$  Mj/kgm-k (5.95 R) at 2800 K which is comparable to the constant heat capacity of  $6.10 \times 10^{-4}$  Mj/kg-k reported in the earlier work.<sup>(15)</sup> Also plotted are solid state measurements made by Cezairliyan<sup>(64)</sup> and Sheindlin, et al.<sup>(65)</sup>, both of which are in agreement with the current



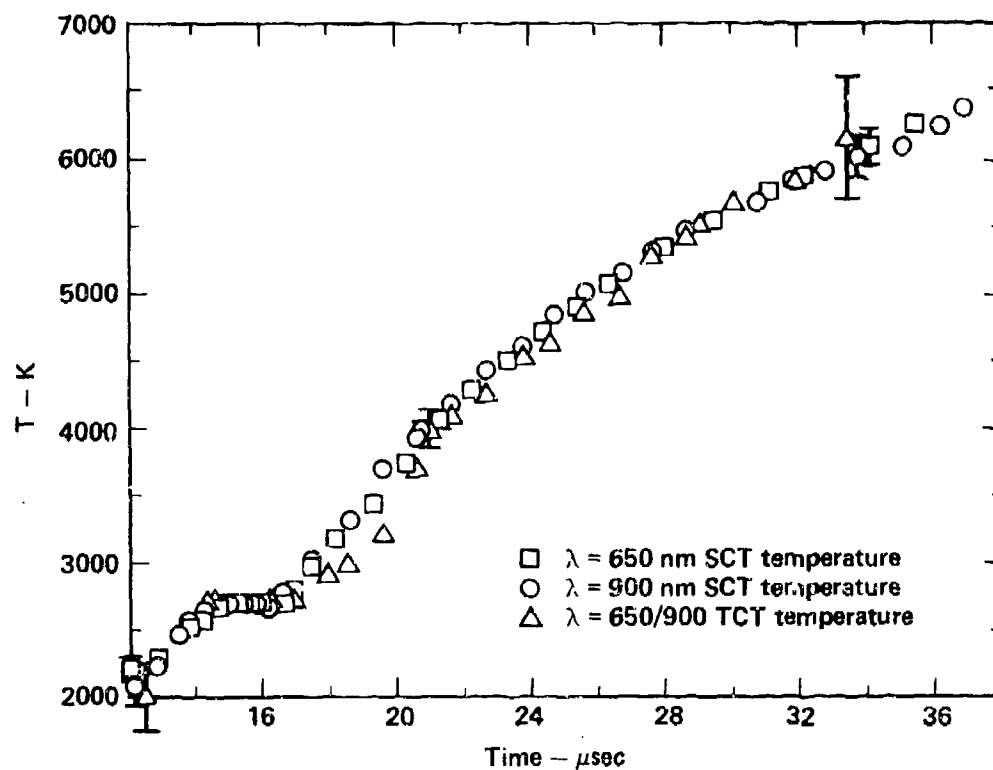


Fig. 32 Niobium Temperature

Niobium temperatures calculated from data taken at 650 and 900 nm are shown as a function of time. Calibration is accomplished by ascribing a temperature of 2741 K to the prominent melting plateau. The excellent agreement among the SCT and TCT temperatures is typical of the results obtainable when both channels have a strong calibration signal yet are sufficiently separated in wavelength to cause significant variations in the ratio of measured intensities over the temperature range.

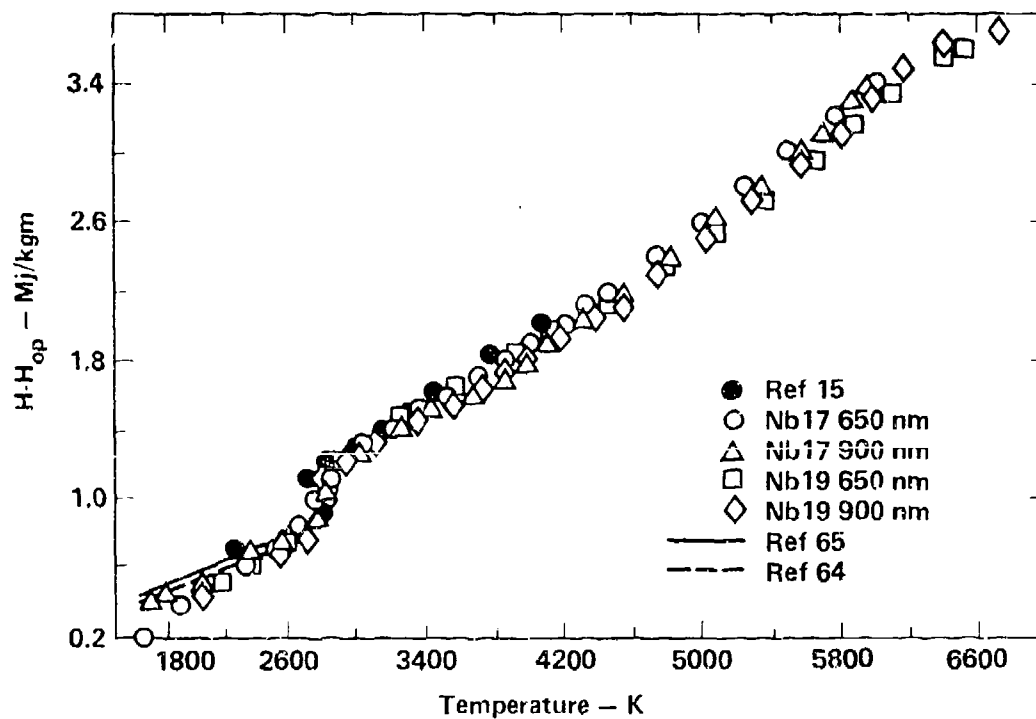


Fig. 33 Niobium Enthalpy vs Temperature

Enthalpy referenced to 300 K and cell pressure is shown as a function of SCT temperatures derived from data taken at 650 and 900 nm. Comparison is made to the solid state measurements of Sheindlin, et al (65) and Savvatimskii (66) and previous IEX data covering a lower temperature range. (15)

data. If the sharp breaks in the curve of Figure 33 are interpreted as the beginning and ending of melt the enthalpy of fusion is determined to be  $0.30 \pm 0.02$  MJ/kgm. Savvatimskii measures the enthalpy of fusion to be  $0.297 \pm 0.0015$  MJ/kgm. (66)

Figure 34 presents niobium resistivities computed from the measured enthalpies of the current work and the 0.2 GPa volumes of the earlier work. (15) The 0.2 GPa volumes are fit with the following expression up to an enthalpy of 3.0 MJ/kgm as referenced to 298 K and cell pressure (0.2 GPa).

$$\frac{V}{V_0} = C_1 + C_2 H + C_3 H^2 \quad (4-28)$$

$$C_1 = 1.0109$$

$$C_2 = 4.0652 \times 10^{-2}$$

$$C_3 = 3.0888 \times 10^{-2}$$

Having a bulk modulus of 170 GPa, niobium is sufficiently stiff that the expected separation between specific volume isobars is much less than measurement errors for IEX range pressures. Thus, Eq. (4-28) is applicable to the current 0.3 GPa data but, because of a lower specific volume boiling point, does not cover the full 4 MJ/kgm range of the recent measurements. For this reason the resistivities of Figure 34 are truncated at 3.0 MJ/kgm. Liquid resistivities are fit by the following expression:

$$\rho = C_1 + C_2 H + C_3 H^2 \quad (4-29)$$

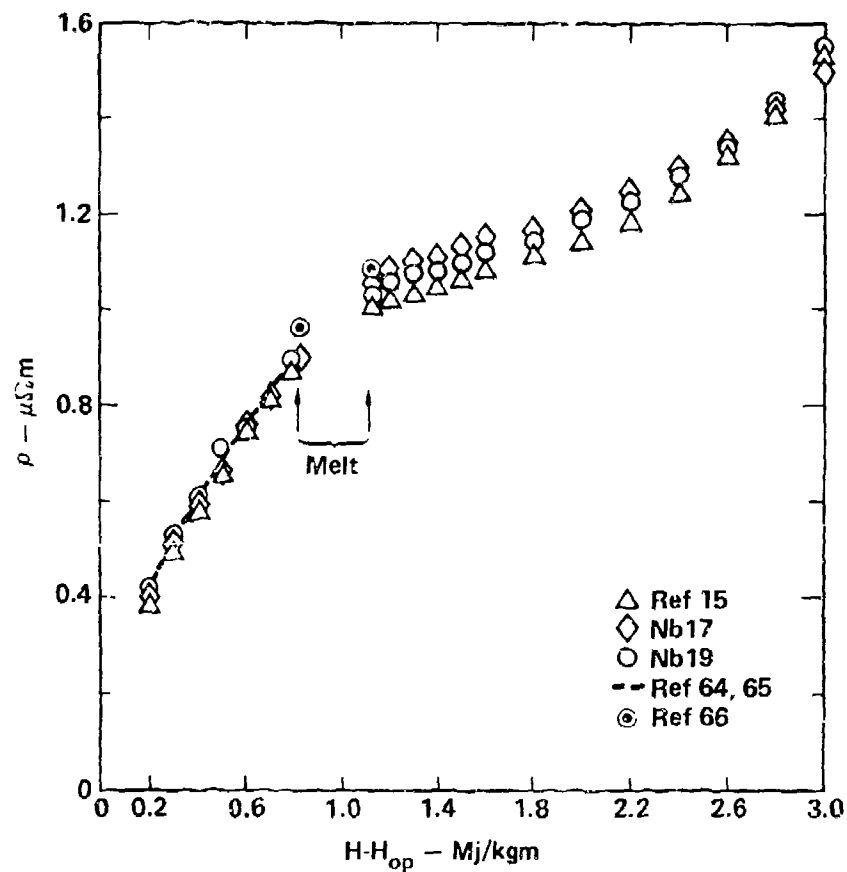


Fig. 34 Niobium Resistivity vs Enthalpy  
Resistivity in  $\mu\Omega m$  is shown as a function of enthalpy referenced to 300 K and cell pressure. Agreement is good with the solid state measurements of Cezairliyan <sup>(64)</sup> and Sheindlin, et al <sup>(65)</sup> but less perfect with the melting point measurements of Savvatimskij.

$$C_1 = 1.0942$$

$$C_2 = -1.2317 \times 10^{-1}$$

$$C_3 = 8.7008 \times 10^{-2}$$

Also plotted for comparison purposes are Cezairliyan's resistivities which are fit by the expression: (64)

$$\rho = 0.1074 + 3.396 \times 10^{-4} T - 1.823 \times 10^{-8} T^2 \quad (4-30)$$

The data of Sheindlin, et al. are used to convert from enthalpy to temperature. (65) Agreement of the current data with Cezairliyan's earlier results is very close. However, Savvatimskii's measurement of the solid and liquid resistivities at the melting point are approximately 5% higher than ours and Cezairliyan's.

Eqs. (4-27), (4-28), and (4-29) are used to generate representative values listed in Table 17 for liquid state niobium. Solid state temperatures and resistivities are either data or literature values, while specific volumes are computed from Eq. (4-28). Enthalpy is referenced to cell pressure for all parameters and is thus only that added resistively.

#### Niobium-Hafnium

Equation of state and resistivity measurements have been made on an alloy of niobium and hafnium, labelled here NbHf. The nominal composition includes 10% hafnium, 1% titanium, 88% niobium, and trace amounts of zirconium, tungsten, tantalum and lesser constituents. Temperature data were taken at 0.3 GPa while density and resistivity were

Table 17  
Measured Properties of Niobium

T(K)	H-H(T <sub>0</sub> ,P) Mj/kgm	V/V <sub>0</sub> <sup>τ</sup>	ρ (μΩm)
400	0.2074*	1.012	
800	0.1412*	1.017	
1200	0.2623*	1.024	0.48
1600	0.3919*	1.032	0.60
2000	0.5322*	1.041	0.72
2400	0.6862*	1.053	0.83
2741 (ℓ)	0.830	1.066	0.90
2741 (S)	1.1336	1.097	1.066
2800	1.1649	1.100	1.059
3200	1.3844	1.126	1.090
3600	1.6174	1.157	1.123
4000	1.8638	1.194	1.167
4400	2.1236	1.236	1.225
4800	2.3969	1.286	1.299
5200	2.6836	1.342	1.390
5600	2.9837	1.407	1.501
6000	3.2973	1.481	
6400	3.6243		
6800	3.9647		

\*Ref. 65

τ Ref. 15

$$V_0 = 0.117 \text{ cm}^3/\text{gm}$$

measured at both 0.2 GPa and 0.4 GPa. For these pressures no parameters exhibit any discernible dependence upon pressure, i.e. there is no resolution between the 0.2 GPa and 0.4 GPa isobars for the specific volume data.

Enthalpy versus temperature data are plotted in Figure 35. A comparison of Figs. 33 and 35 reveals quite similar data traces with two possible exceptions. First, assuming each material was driven as close as possible to the liquid vapor two phase boundary, the NbHf required more enthalpy addition to traverse the liquid regions and thus achieved higher temperatures. Secondly, the melting plateau is less sharply defined for NbHf, as might be expected for the alloy melting transition. Although full range agreement among the graphed SCT temperatures is excellent some qualification is necessary in interpreting these data. Calibration was accomplished by assigning to the melting plateau a temperature of 2741 K (see Eq. 3-10), which is the melting point of pure niobium and not necessarily applicable to the alloy. The NbHf melting point might actually be suppressed as it was in gold-copper or it could be higher than that of pure niobium. In the absence of a suitable phase diagram it was felt best to use the niobium number. This choice is vindicated somewhat by the resulting overall consistency of the calculation. Experience has shown that an improper choice of calibration point leads to difficulty in achieving agreement among the independently determined temperatures. The error flags of Figure 35 are identically those of Figure 32 and do not accommodate the above discussed possibility of a large systematic error. The entire range of liquid NbHf data are least squares fit by the following expression:

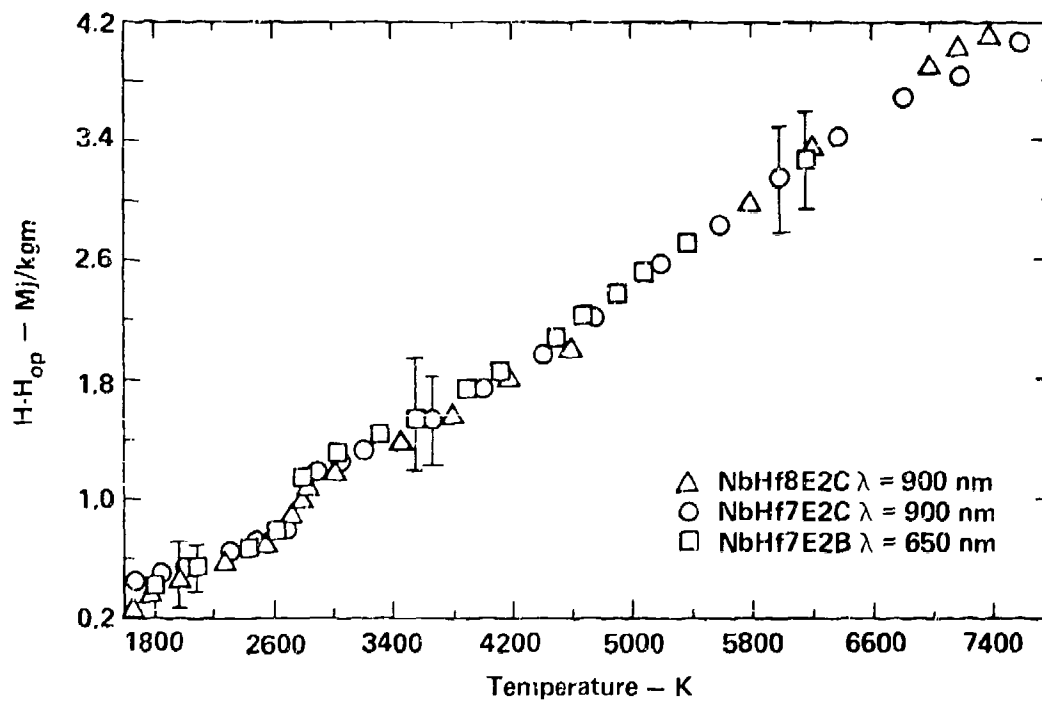


Fig. 35 Niobium-Hafnium Enthalpy vs Temperature

Enthalpy referenced to 300 K and cell pressure is displayed as a function of SCT temperatures derived from data taken at 650 and 900 nm. Calibration is accomplished by assuming the rather indistinct melting plateau of the alloy to occur at the melting temperature of pure niobium.



$$H = C_1 + C_2 T + C_3 T^2 \quad (4-31)$$

$$C_1 = -0.33655$$

$$C_2 = 4.4606 \times 10^{-4}$$

$$C_3 = 2.0857 \times 10^{-8}$$

where enthalpy is again referenced to 298 K and the cell pressure.

For completeness the results of three recent volume measurements on NbHf are graphed in Figure 36.<sup>(67)</sup> The plotted data are representative of several runs made at 0.2 and 0.4 GPa with the 5% uncertainty intervals appearing to model well the scatter. The full range of expansion is least squares fit by the following expression:

$$H = C_1 + C_2 \left( \frac{V}{V_0} \right) + C_3 \left( \frac{V}{V_0} \right)^2 + C_4 \left( \frac{V}{V_0} \right)^4 \quad (4-32)$$

$$C_1 = -16.789$$

$$C_2 = 25.814$$

$$C_3 = -10.346$$

$$C_4 = 14.010$$

The inverse expression is:

$$\frac{V}{V_0} = C_1 + C_2 H + C_3 H^2 \quad (4-33)$$

$$C_1 = 1.0165$$

$$C_2 = 5.3616 \times 10^{-2}$$

$$C_3 = 2.7721 \times 10^{-2}$$

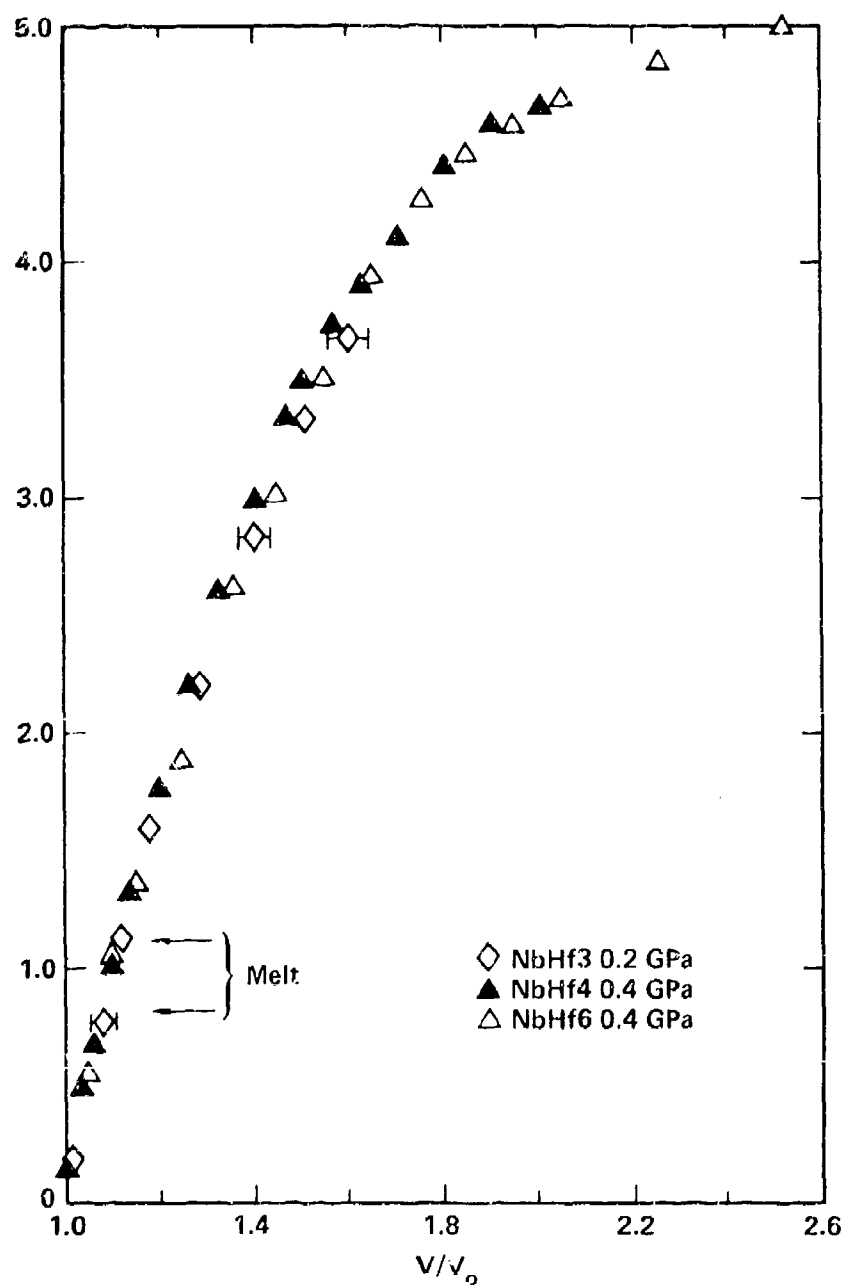


Fig. 36 Niobium-Hafnium Enthalpy vs Volume

Enthalpy referenced to 300 K and cell pressure is shown as a function of volume normalized to  $V_0 = 0.113 \text{ cm}^3/\text{gm}$ . Data are taken at 0.2 and 0.4 GPa and exhibit no separation between the isobars.

where it was necessary to truncate the range to less than 4.5 MJ/kgm in order to achieve a reasonable low order fit.

NbHf resistivities are plotted in Figure 37 as a function of enthalpy.<sup>(67)</sup> The resistivities of the alloy are quite similar to those of niobium which can be seen by comparing Figs. 34 and 37. The extended range of the alloy data is made possible because the 0.4 GPa pressures suppress boiling to higher enthalpies and lower densities. Liquid state alloy data are fit as follows:

$$\rho = C_1 + C_2 H + C_3 H^2 \quad (4-34)$$

$$C_1 = 1.1414$$

$$C_2 = -1.2459 \times 10^{-1}$$

$$C_3 = 8.5510 \times 10^{-2}$$

Enthalpy is again only that due to resistive heating.

Eqs. (4-31), (4-33), and (4-34) are used to generate the numbers tabulated in Table 18. A comparison of Tables 17 and 18 reveals that in the liquid state the enthalpies necessary to reaching a given temperature are consistently less in NbHf than for niobium. Solid state enthalpies are quite similar for the two materials. Measured volume expansions are equivalent as a function of temperature but the alloy requires less enthalpy to get to the same expansion. Further refinement of the temperature data is possible should the necessary melting point data become available.

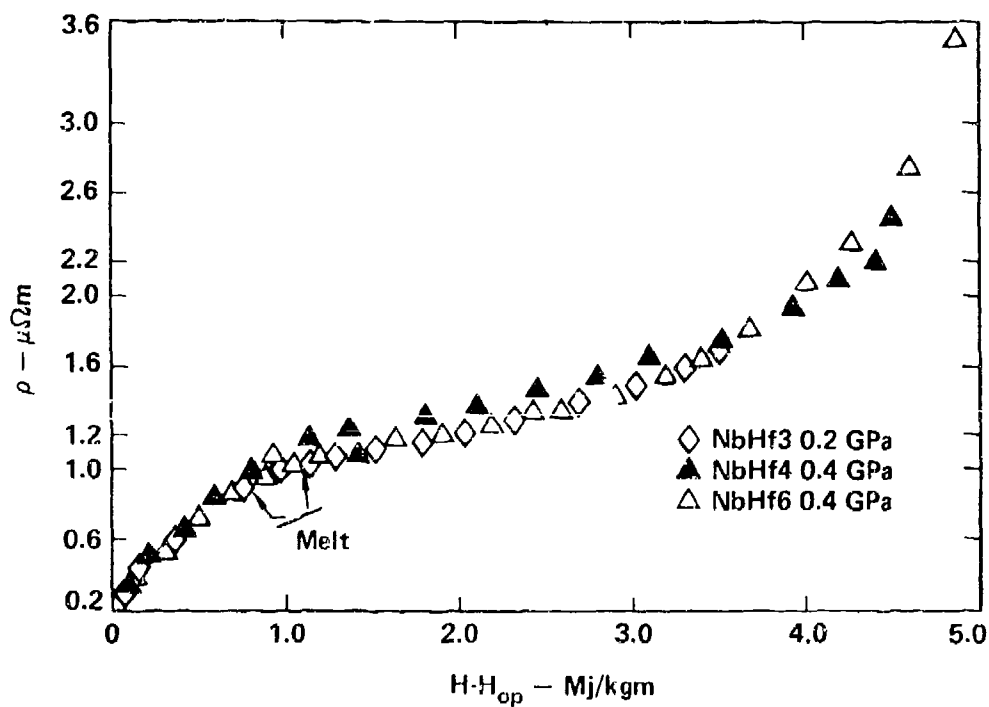


Fig. 37 Niobium-Hafnium Resistivities

Resistivity in  $\mu\Omega\text{m}$  is displayed as a function of enthalpy referenced to 300 K and cell pressure for data taken at 0.2 and 0.4 GPa. The transition from the solid to the liquid state is less sharply defined than for pure niobium.

Table 18  
Measured Properties of Niobium-Hafnium

T(K)	H-H(T <sub>0</sub> ,P)Mj/kgm	V/V <sub>0</sub>	$\rho$ ( $\mu\Omega\text{m}$ )
400	0.0274*	1.018	0.30'
800	0.1412*	1.025	0.43'
1200	0.2623*	1.032	
1600	0.3919*	1.042	0.55'
2000	0.530 <sup>T</sup>	1.052	0.76'
2400	0.690 <sup>T</sup>	1.067	0.90'
2741 (L)	0.830 <sup>T</sup>	1.080	1.07'
2741 (S)	1.0428	1.103	1.104
2800	1.0759	1.106	1.106
3200	1.3044	1.134	1.124
3600	1.5396	1.165	1.152
4000	1.7814	1.200	1.191
4400	2.0299	1.240	1.241
4800	2.2851	1.284	1.303
5200	2.5469	1.333	1.379
5600	2.8155	1.387	1.469
6000	3.0907	1.447	1.574
6400	3.3725	1.513	1.694
6800	3.6611	1.584	1.832
7200	3.9563	1.663	1.988
7600	4.2582	1.747	2.162

\* Ref. 65 for Niobium

<sup>T</sup> Data Figure 35

' Data Figure 37

$$V_0 = 0.113 \text{ cm}^3/\text{gm}$$

## 5. ELECTRICAL RESISTIVITY AND EQUATION OF STATE MODELLING

This chapter is devoted to the rudimentary beginnings of using the data presented in the previous chapter to reach some basic understanding of liquid metals. The basic theory applied, labelled by Ziman "the method of neutral pseudo-atoms",<sup>(17)</sup> is not new and has been widely discussed in the literature for the past twenty years. What has emerged is a theory rife with necessary simplifications and adjustable parameters to be determined empirically. The major value and innovation of the calculations presented here is that they take advantage of a much broader range of liquid metal data than has been available previously. Because of these data it has been possible to subject the theory to calibration points at much higher temperatures and pressures and lower density than were formerly attainable.

Electrical resistivity is the primary material property modelled, and extensive calculations are presented on liquid lead and liquid uranium. Lead has been chosen because of the free electron like nature of its conduction electrons while uranium presents a much more complex case having d and f bands near the Fermi surface. It is believed that Ziman's nearly free electron model of a metal should be applicable to both materials although the theory has a somewhat simpler form for lead whose conduction electrons retain inherent s and p characteristics. For lead it is possible to use non-unique screened ion model potentials to characterize the scattering of the "free" electrons by the ionic cores, while for uranium it is necessary to use the t matrix of a muffin tin potential to calculate the relevant scattering cross sections.<sup>(69)</sup>

This chapter will begin with an elementary development of the nearly free electron expression for liquid metal resistivity. This is shown to depend only on the interaction potential between an electron and a single ion plus the distribution of the ions. The necessary distribution function is obtained by treating the ionic cores as hard spheres and employing the hard sphere pair distribution function as developed by Ashcroft and Lekner from a known solution to the Percus-Yevick equation.<sup>(47)</sup> Among the issues to be discussed will be the choice of hard sphere diameter as a function of liquid density, and the selection of an appropriate dielectric function to properly account for the otherwise neglected electron-electron interactions and electron correlation and exchange effects. Next the computations on liquid lead resistivity will be presented along with some parallel but slightly different equation of state calculations using a code developed by Ross<sup>(21)</sup> from a theory outlined by Jones.<sup>(69)</sup> Finally, the results of t-matrix calculations on liquid uranium will be discussed with allusions to possible methods of improving the agreement between data and theory.

#### Nearly Free Electron Resistivity

In the nearly free electron theory of metals the metal is considered to be a matrix of ionic cores, each consisting of a nucleus plus the most closely held electrons, immersed in a sea of conduction electrons. The cores have an effective charge  $z_{\text{eff}}$  and the conduction electrons tend to form screening clouds about each ion. The usual practice is to ignore the screening initially in deriving an expression for electron-ion interaction potential, and incorporate it later on in the form of a

dielectric function. With this simplification each conduction electron can be considered to move independently of the others in a field  $\epsilon$  due to the ionic cores. In concert with Reif's treatment of this situation the equation of motion of each conduction electron is: (70)

$$m \frac{dv_z}{dt} = e\epsilon \rightarrow v_z = v_{z0} + e\epsilon t \quad (5-1)$$

where  $v_z$  is that component of velocity in the direction of the impressed field. If the system is assumed to be in equilibrium just after a collision the net component of the particle velocity will be zero at time  $t = 0$ . Letting  $\tau$  be the average time between collisions the average velocity of a particle in the direction of the field will be:

$$\langle v_z \rangle = \frac{e\epsilon\tau}{m} \quad (5-2)$$

The current density may be given as:

$$j_z = n_e e \langle v_z \rangle = z_{\text{eff}} n e v_z = \sigma \epsilon \quad (5-3)$$

which is an expression of Ohm's law where  $n$  is the ion density,  $z_{\text{eff}}$  is the number of free electrons per ion, and  $\sigma$  is the electrical conductivity. The resistivity, defined as the reciprocal of the conductivity, is:

$$\rho = \frac{m}{z_{\text{eff}} n e^2 \tau} \quad (5-4)$$



Eq. (5-4) expresses the resistivity of a metal, a fraction of whose electrons may be considered to move freely independent of each other under the influence of a spatially uniform field for an average time,  $\tau$ , between collisional encounters with the ions. In modifications to make the model more realistic it is common practice to retain the form of Eq. (5-4) but to accommodate the electron's periodic potential environment with an effective mass in place of true mass, and to incorporate electron-electron interactions in the calculation of  $\tau$ , the relaxation time.

Following a development originally suggested by Mott<sup>(71)</sup> and discussed in detail in Appendix C the relaxation time may be expressed as:

$$\frac{1}{\tau_f} = 2\pi K_f^2 \int_0^\pi (1 - \cos\theta) P(\theta) \sin\theta d\theta \quad (5-5)$$

where  $\theta$  is the angle between incident and scattered wave vectors,  $K_f$  is the wave vector magnitude of a free electron at the Fermi surface, and  $P(\theta)$  is a transition rate derivable from time dependent perturbation theory.<sup>(72)</sup> Implicit in Eq. (5-5) is the assumption that only those electrons very near the Fermi surface participate in the scattering process.  $P(\theta)$  is given by:

$$P(\theta) = P_{\vec{K}, \vec{K}+\vec{q}} = \frac{2\pi}{\hbar} |\langle \vec{K}+\vec{q} | W(\vec{r}) | \vec{K} \rangle|^2 n(E') \quad (5-6)$$

where  $W(\vec{r})$  is the scattering potential experienced by the electron due to the ionic cores, and  $n(E')$  is the density of states available to the electron at the Fermi surface. If it is assumed that the potential,

$W(\vec{r})$ , can be expressed as the sum of the potentials due to the  $N$  ion sites it is possible to factor the matrix element as follows: <sup>(73)</sup>

$$\langle \vec{K} + \vec{q} | W(\vec{r}) | \vec{K} \rangle = S(q) \langle \vec{K} + \vec{q} | \omega(\vec{r}) | \vec{K} \rangle \quad (5-7)$$

where

$$S(q) = \frac{1}{N} \sum_j e^{i\vec{q} \cdot \vec{r}_j} \quad (5-8)$$

is the structure factor and  $\omega(\vec{r})$  is the scattering potential due to a single ion. The normalized Fourier transform of this single ion scattering potential is known as the form factor. Using the transformation  $q = 2K_f \sin \frac{\theta}{2}$  in Eq. (5-5) and substituting the result into Eq. (5-4) the expression for the free electron resistivity becomes:

$$\rho = \frac{3\pi\Omega}{2e^2 v_f} \int_0^1 S^2(q) [\langle \vec{K} + \vec{q} | \omega(\vec{r}) | \vec{K} \rangle]^2 \left( \frac{q}{2K_f} \right)^3 d\left( \frac{q}{2K_f} \right) \quad (5-9)$$

$\Omega$  is the volume of the system and  $v_f$  is a velocity related to the Fermi energy and the Fermi wave number by the free electron expression

$$E_f = \frac{mv_f^2}{2} = \frac{\hbar^2 K_f^2}{2m}.$$

In order to implement Eq. (5-9) it is necessary to obtain a representation for the structure factor,  $S(q)$ , to model the ion electron potential, and to provide a modification of the form factor that will accommodate electron-electron interactions and electron correlation and exchange effects. While in principle  $S(q)$ , the Fourier transform of the

pair distribution function, is directly obtainable from diffraction experiments,<sup>(74,75)</sup> there exists no data over much of the temperature range of this work. However, a closed form expression for  $S^2(q)$  has been obtained by Ashcroft and Lekner<sup>(47)</sup> who assume that the ion-ion interaction is the dominant phenomenon in determining the ionic arrangement in a liquid metal, and model that interaction with a hard sphere potential. Subject to these assumptions they solve the Percus-Yevick equation for the factor  $a(q) = NS^2(q)$ . In terms of this factor the resistivity may be expressed as:

$$\rho = \frac{3\pi\Omega_0}{\hbar e^2 v_f^2} \int_0^1 a(\vec{q}) [ \langle \vec{K} + \vec{q} | \omega(\vec{r}) | \vec{K} \rangle ]^2 4 \left( \frac{q}{2K_f} \right)^3 d \left( \frac{q}{2K_f} \right) \quad (5-10)$$

where  $\Omega_0$  is the volume per ion and  $\hbar k_v = mv_f$ . The Percus-Yevick derived factor is then:

$$a(q\sigma) = [1 - nc(q\sigma)]^{-1} \quad (5-11)$$

where  $\sigma$  is a hard sphere diameter,  $n$  is the ion density, and  $c(q\sigma)$  is given by:

$$c(q\sigma) = -4\pi\sigma^3 \int_0^1 ds s^2 \frac{\sin(sq\sigma)}{sq\sigma} (\alpha + \beta S + \gamma S^3) \quad (5-12)$$

with

$$\begin{aligned} \eta &= \pi/6 n\sigma^3 \\ \alpha &= (1+2\eta)^2 / (1-\eta)^4 \\ \beta &= -6(1+\eta/2)^2 / (1-\eta)^4 \\ \gamma &= (1/2) \eta (1+2\eta)^2 / (1-\eta)^4 \end{aligned} \quad (5-13)$$

The principle method employed for determining a suitable hard sphere diameter with which to implement Eq. (5-10) rests upon requiring the packing fraction,  $\eta$ , to be 0.45 on the melting curve (liquidus), a value for which calculated  $a(q)$  fit the neutron diffraction data of Sharrah, et al., in the case of liquid lead.<sup>(74)</sup> For a given temperature,  $T_m$ , it is possible to determine the melting volume using Eq. (4-7), where  $V_m$  is the volume at the solidus.  $V_L$ , the volume at the liquidus, can then be obtained by adding a  $\Delta V$  which is assumed to be approximately the same increment prevailing at the normal melting temperature.  $V_L$  can then be used with the first of Eq. (5-13), the packing fraction expression, to find a value for  $\sigma$ , the hard sphere diameter. The relevant quantities are shown schematically in Fig. 38 and the resulting hard sphere diameters computed for liquid lead are graphed in Fig. 39. The function  $a(q)$  is thus fully determined.

The unscreened electron ion interaction potential,  $\omega(\vec{r})$ , is not uniquely determined. It is common practice to choose both the form and the adjustable parameters of  $\omega(\vec{r})$  to achieve agreement between data and calculation. One form found to work particularly well with lead is a combination of coulombic and exponential terms usually identified with Harrison<sup>(76)</sup> and discussed in detail by Egelstaff.<sup>(77)</sup>

$$\omega(r) = \frac{-z_{\text{eff}}e^2}{r} + C e^{-r/R_c} \quad (5-14)$$

Evaluation of the matrix element with this potential function produces the Harrison bare sphere form factor:

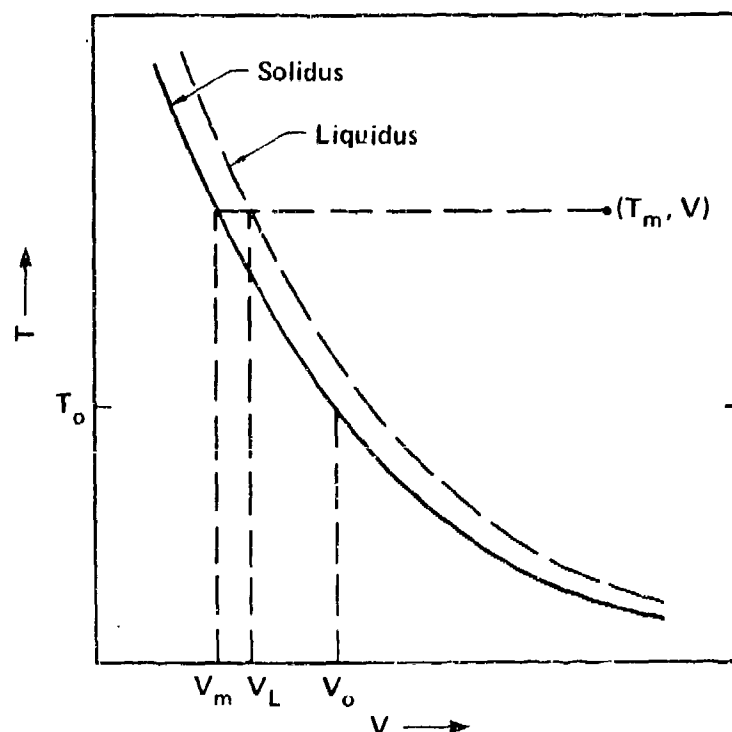


Fig. 38 Melting Line Quantities for Lindemann Scaling

This is a schematic representation of the quantities necessary to the Lindemann scaling law as expressed in Eq. (4-7). Given any temperature,  $T_m$ , it is possible to compute the "melting volume",  $V_m$ , using the normal melting volume,  $V_0$ , and the normal melting temperature,  $T_0$ .  $V_L$ , the volume at the liquidus for temperature  $T_m$  is used with a known packing fraction to find a hard sphere diameter.

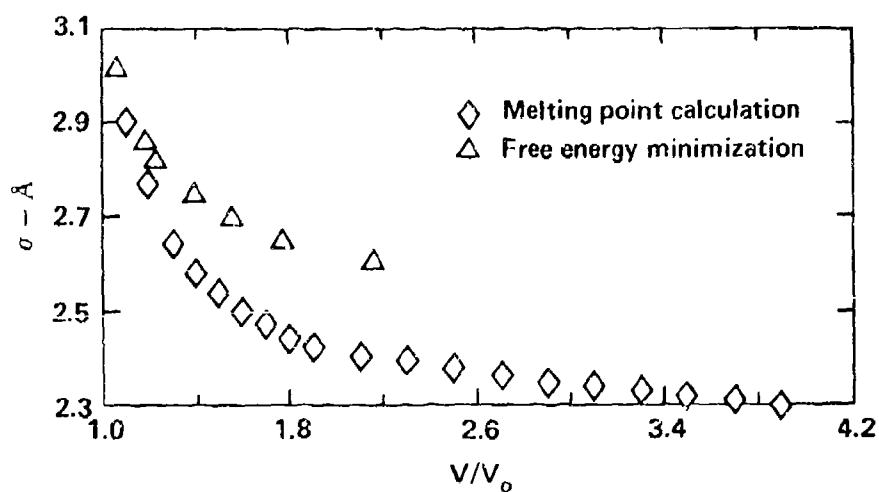


Fig. 39 Hard Sphere Diameters for Liquid Lead

The hard sphere diameter in angstroms is shown as a function of volume normalized to  $V_0 = 0.088 \text{ cm}^3/\text{gm}$ . Comparison is made between diameters calculated from Lindemann melting point scaling of Eq. (4-7) and Helmholtz free energy minimization as computed in "MET". (81)

$$V(q) = \left\{ \frac{4\pi z_{\text{eff}} e^2}{q^2} + \frac{8\pi C R_c^3}{[1 + (q R_c)^2]^2} \right\} \frac{1}{\Omega_0} \quad (5-15)$$

where  $C$  and  $R_c$  allow a two parameter fit to the resistivity data. The choice of  $\omega(r)$  and derivation of Eq. (5-15) are further discussed in Appendix D along with several other form factors. The guiding philosophy of these modelling calculations has been to choose an ion-electron interaction potential based on physical considerations with the minimum number of adjustable parameters necessary to obtain a good fit to available data. This has resulted in local potential form factors analogous to Eq. (5-15). The approach has been used by Ross<sup>(44)</sup> and Wallace<sup>(78)</sup> among others who have chosen pseudo-potential parameters based upon matching resistivity and phonon spectrum aluminum data, respectively. This methodology should be contrasted to the more usual approach described by Anamalu and Heine<sup>(79)</sup> and used by Sunstrom<sup>(80)</sup> and Evans<sup>(81)</sup> among others (see Appendix D).

In order to achieve reasonable computational results it is necessary to modify the bare sphere form factor with a dielectric function to account for electron-electron interactions. For this purpose the Linhard dielectric function given by:

$$\epsilon(q) = 1 - \frac{me^2}{2\pi^2 K_F x^2} \left[ \frac{1-x^2}{2x} \ln \left| \frac{1+x}{1-x} \right| + 1 \right] \quad (5-16)$$

with  $x = \frac{q}{2K_F}$  has been found to be appropriate<sup>(82)</sup> (see Appendix D). A further modification proposed by Hubbard and Sham<sup>(83,84)</sup> and

specifically applied by Wallace<sup>(78)</sup> accounts for exchange and correlation effects. The form factor used for the calculations of this work is then:

$$\langle \vec{k} + \vec{q} | \omega(\vec{r}) | \vec{k} \rangle = \frac{V(q)}{[1 + \{c(q) - 1\} \{1 - g(q)\}]} \quad (5-17)$$

where  $g(q) = q^2 / (q^2 + \lambda K_f^2)$ .

The parameter  $\lambda$  is calculated in a manner outlined by Brovman, et al:<sup>(85)</sup>

$$\lambda = \frac{2}{1 + \frac{0.0155\pi}{K_f a_B}} \quad (5-18)$$

where  $a_B$  is the Bohr radius and  $\lambda$  differs from 2 only due to the small second term in the denominator which introduces the effect of electron correlations.

The combination of Eqs. (5-10), (5-11), (5-15), and (5-17) is sufficient to compute the liquid metal resistivity. The independent variable is the specific volume,  $V$ , and the calculation is initiated by choosing  $V$  and from that finding the values of wave number and velocity at the Fermi surface.  $K_f = \left[ \frac{3\pi^2 N_a Z_{eff}}{V} \right]^{1/3}$  and  $v_f = \frac{\hbar K_f}{m}$  are the free electron values for these quantities with  $N_a Z_{eff}$  being the number of free electrons in the volume  $V$ . The integral in Eq. (5-10) is evaluated numerically choosing values of  $q$  from just above 0 to a maximum of  $2K_f$ . The process is repeated for each new value of  $V$  until values of resistivity have been computed for the entire range of measured specific volumes. Data are needed in order to associate a given temperature with each choice of specific volume, the temperature being required to compute



a hard sphere diameter (see Eq. 4-7 and Fig. 38). A comparison is made between computed and measured resistivities, and the parameters of the pseudo-potential (see Eq. 5-15) or the effective number of free electrons per ion,  $Z_{\text{eff}}$ , are varied until the best agreement is achieved.

#### Electrical Resistivity and Equation of State Calculations on Liquid Lead

Fig. 40 compares resistivity data with pseudo-potential calculations made on liquid lead. The data are the 0.3 and 0.4 GPa traces while the calculations employ either the Harrison bare sphere form factor of Eq. (5-15) or and Ashcroft hollow core form factor listed below:<sup>(18)</sup>

$$V(q) = \frac{-4\pi Z_{\text{eff}} e^2}{q^2} \cos(qR_c) \quad (5-19)$$

Eq. (5-19) represents a bare sphere form factor derived from the following potential:

$$V(r) = \begin{cases} 0 & r < R_c \\ -\frac{Z_{\text{eff}} e^2}{r} & r > R_c \end{cases} \quad (5-20)$$

The hard sphere diameters of Fig. 39 are common to all the calculations except those labelled MET. These diameters make use of the data of Kirschenbaum et al.<sup>(7)</sup> for volume expansions between 1.1 and 1.3 and the current temperature-volume data for expansions between 1.3 and 2.3. Because of the lack of temperature data at higher expansions  $\sigma$  was allowed to vary linearly between 2.4 and 2.3A for 2.3 to 4.0 fold expansions. "MET"<sup>(21)</sup> calculations employ the bare sphere form factor of Eq. (5-15) but use a hard sphere diameter obtained by minimizing the Helmholtz free energy with respect to the hard sphere diameter.<sup>(69)</sup>

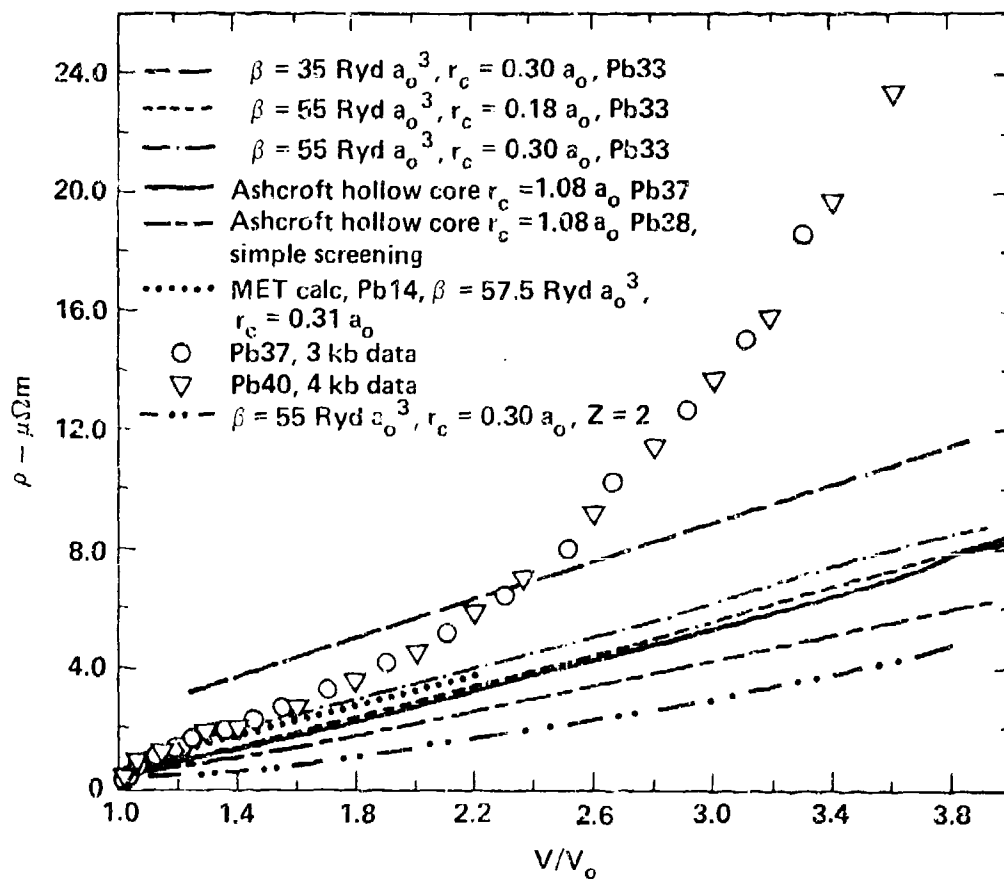


Fig. 40 Liquid Lead Pseudo-Potential Calculations

Lead resistivity data taken at 0.3 and 0.4 GPa displayed as a function of volume normalized to  $V_0 = 0.028 \text{ cm}^3/\text{gm}$  are compared to pseudo-potential calculations. The calculations are done with Ashcroft hollow core and Harrison-Wallace bare sphere form factors employing screening of various degrees of sophistication. Results show that liquid lead resistivity is a strong function of volume and that nearly free electron theory is capable of modelling this only for relatively small expansions.

These latter hard sphere diameters which are tabulated in Table 19 are plotted in Fig. 39 for comparison purposes.

To demonstrate the effect of screening the Ashcroft hollow core form factor is used both with simple Linhard dielectric screening and the more complex screening of Eq. (5-17). In both cases the parameter  $R_C$  is the 0.57 Å chosen by Ashcroft to produce a form factor that correctly predicts the known band gap of lead.<sup>(18)</sup> The more complex screening produces slightly better agreement with experiment but neither calculation produces the dramatic growth in resistivity measured at higher expansions.

The initial choice of parameters used with the Harrison-Wallace form factor, Eq. (5-15), was based upon those reported by Harrison.<sup>(86)</sup> He models measured dispersion relations rather imperfectly with two sets of parameters, the first being  $\beta = 96.9 \text{ ryd} \cdot a_0^3$ ,  $R_C = 0.31 a_0$  and the second being  $\beta = 19.6 \text{ ryd} \cdot a_0^3$ ,  $R_C = 0.30 a_0$ . In these calculations  $\beta = 8 \pi C R_C^3$  and is held constant independently of  $R_C$ . By trial and error the best fit to the resistivity data was obtained using  $\beta = 55 \text{ ryd} \cdot a_0^3$  and  $R_C = 0.30 a_0$ . The calculational sensitivity to  $\beta$  and  $R_C$  is illustrated by two additional traces, one done with  $\beta = 55 \text{ ryd} \cdot a_0^3$  and  $R_C = 0.18 a_0$ , and a second with  $\beta = 35 \text{ ryd} \cdot a_0^3$  and  $R_C = 0.30 a_0$ . These variations show that resistivity can be off-set to higher or lower values with a change in these parameters but that the overall functional dependence on specific volume is not appreciably altered.

One further variation tried in order to better model the data was a change in the number of free electrons per ion. It seems reasonable to assume that at the higher expansions there might be a tendency for some

of the electrons that were free at more normal densities to associate themselves more closely with individual ions. Using this reasoning the pseudopotential parameters that gave the best fit with a  $z_{\text{eff}}$  of 4 were tried with a  $z_{\text{eff}}$  of 2. The result graphed in Fig. 40 was a lessening of the resistivity, further widening the discrepancy between data and calculation. It was possible to bring the  $z_{\text{eff}} = 2$  calculation into line with the best  $z_{\text{eff}} = 4$  curves by reducing  $\beta$  to approximately 30 ryd  $a_0^3$ . However, the dependence upon relative volume is still almost linear rather than the steep exponential required to model the data.

Table 19 summarizes the equation of state and resistivity calculations done with the computer code "MET".<sup>(21)</sup> As has been pointed out MET implements the theory discussed in detail by Jones<sup>(69)</sup> and makes use of the Harrison-Wallace form factor, Eq. (5-15). The first three columns of Table 19 are data while the last five columns list computed values. Volume-temperature data are appropriate to 0.4 GPa so a completely successful calculation should reproduce 0.4 GPa in the column labelled pressure. The best fit resistivities were obtained using  $\beta = 57.5$  ryd  $a_0^3$  and  $R_C = 0.31 a_0$ . The resistivities, sound speeds, and packing fractions all appear reasonable while computed pressures are totally unrealistic. In an attempt to obtain a more realistic pressure without altering the transport properties an overlap potential of the Born-Mayer form was incorporated into the calculation. Benedek calculates the two-body overlap potential using nonrelativistic Hartree-Fock wave functions and expresses the result in the form,  $\phi = Ae^{-R/\rho}$ .<sup>(87)</sup> He determines the parameters A and  $\rho$  from a least squares fit of several of these calculations performed for separation

Table 19  
MET Calculations on Liquid Lead

T(K)	Vol/mole $\text{cm}^3$	$V/V_0$	$\rho (\mu\text{g}/\text{cm})$	Press (GPa)	$U_s$ km/sec	Packing Fraction	$\sigma$ cm
600	19.35	1.06	0.953	-16.7	1.2	0.449	$3.02 \times 10^{-8}$
1600	21.50	1.18	1.214	-15.3	1.18	0.342	$2.86 \times 10^{-8}$
2000	22.54	1.235	1.344	-15.0	1.13	0.313	$2.82 \times 10^{-8}$
3000	25.39	1.39	1.713	-14.2	1.16	0.258	$2.75 \times 10^{-8}$
4000	28.53	1.56	2.134	-13.4	0.88	0.217	$2.70 \times 10^{-8}$
5000	32.58	1.78	2.696	-12.5	0.76	0.181	$2.65 \times 10^{-8}$
5980	39.34	2.16	3.665	-11.5	1.27	0.143	$2.61 \times 10^{-8}$

distances between 1.99 and 2.39A, which correspond to compressed states for lead. Nearest neighbor distances for the expanded liquid states of interest to current calculations are on the order of 4A or more. Not surprisingly Benedek's calculated parameters,  $A = 1.566 \times 10^4$  ryd and  $\rho = 0.361 a_0$ , yield an insignificant overlap potential at the interatomic distances characteristic of expanded liquid lead. Subsequent adjustment of these parameters to raise the potential led to greater than solid density packing fractions and nonconsistent thermodynamic properties. The effects of ionic core overlap apparently cannot be made to model the physics of the expanded states of lead.

In reviewing the calculations illustrated in Fig. 40 some broad conclusions may be reached. First, it is quite possible to precisely model measured liquid lead resistivities over the very limited range of previous data with a variety of form factors and a range of reasonable form factor parameters. Secondly, dispersion relationship modelling is not sufficiently precise to yield an unequivocal choice of form factor. Finally, while pseudo-potential theory appears to be effective for low specific volumes it fails to predict the correct volume dependence for resistivity over the highly expanded states of the current measurements.

#### Uranium T-Matrix Calculations

In the event that the conduction or valence electrons are not s or p like the weak scattering criterion inherent in the cross section calculations based upon Eq. (5-6) is not automatically satisfied by the screened coulomb pseudo-potential approach discussed so far. As pointed out by Ziman what is needed is a quasi-potential whose matrix elements give the true scattering amplitude from the ionic cores.<sup>(17)</sup> Such a

matrix is most commonly referred to as a t-matrix. The conduction electrons of uranium are known to exhibit d and f character making it necessary to pursue t-matrix formalism in calculating uranium resistivities. Skipping for the moment the justification, the t-matrix calculation is quite similar in form to the pseudo potential calculation. Resistivity is given by the following expression:

$$\rho = \frac{3\pi\Omega_0}{e^2\hbar v_f^2} \int_0^1 a(q) |t(\vec{k}, \vec{k}')|^2 4\left(\frac{q}{2k_f}\right)^3 d\left(\frac{q}{2k_f}\right) \quad (5-21)$$

where all quantities are identical to those of Eq. (5-10) with the exception that the t-matrix has been substituted for the screened coulomb form factor. The t-matrix gives the probability of an electron in state  $|\vec{k}\rangle$  being scattered into state  $|\vec{k}'\rangle$  and can be written as: <sup>(68)</sup>

$$t(\vec{k}, \vec{k}') = \frac{2\pi\hbar^3}{m(2mE)} \frac{1}{\Omega_0} \sum_{\ell} (2\ell+1) \sin\eta_{\ell}(E) \exp[i\eta_{\ell}(E)] P_{\ell}(\cos\theta) \quad (5-22)$$

The  $\eta_{\ell}$ 's are phase shifts calculated at energy E.

Qualitatively, the conduction electrons are again assumed free and are thus represented as before by a plane wave. The plane wave may then be expanded into a set of spherical waves given by:

$$e^{i\vec{k}\cdot\vec{r}} = \sum_{\ell=0}^{\infty} (2\ell+1) i^{\ell} j_{\ell}(Kr) P_{\ell}(\cos\theta) \quad (5-23)$$

where each component or partial wave is associated with an angular momentum  $\sqrt{\ell(\ell+1)} \hbar$ . <sup>(88)</sup> Upon interacting with an ionic core different components experience different phase shifts,  $\eta_{\ell}$ , each of

which depends upon the free electron's energy and the potential used to compute the phase shift. The advantage of using phase shifts to describe the scattering potential is that, although quite deep interaction potentials may be modelled, the form of the t-matrix, Eq. (5-22), automatically satisfies the weak scattering criterion.<sup>(17)</sup> This is because only those portions of  $\eta_l$  over and above multiples of  $2\pi$  enter into the calculations. Shifts greater than  $2\pi$  correspond to rapid oscillations within the potential well, and are indicative of large electron kinetic energy which cancels the effect of the deep attractive well.

As with the pseudo-potential calculation the electrons participating in the scattering are considered to be near the Fermi level in energy, and the Fermi energy is a function of density or specific volume. It is therefore necessary to obtain the phase shifts as a function of specific volume in order to calculate resistivities. For uranium it was felt that the conduction electrons could be adequately described by s, p, d, and f components. The required phase shifts were obtained by extrapolating self consistent augmented plane wave calculations of McMahon<sup>(20)</sup> from the compressed volumes at which they were made to the expanded regime of the current data. A linear fit produced the following expressions for phase shifts good from normal density to two fold expanded:

$$\begin{aligned}
 \eta_s &= 0.82 (V/V_0) - 2.64 \\
 \eta_p &= 0.63 (V/V_0) - 1.73 \\
 \eta_d &= 0.015 (V/V_0) + 5.5 \\
 \eta_f &= -0.39 (V/V_0) + 1.38
 \end{aligned}
 \tag{5-24}$$



The Fermi energy was also taken from McMahan's APW calculation and is fit by the following expression:

$$E_f = [4.39 - 3.46 \left( \frac{V}{V_0} \right) + 0.8 \left( \frac{V}{V_0} \right)^2] \times 10^{-11} \text{ ergs} \quad (5-25)$$

Using this energy  $K_f$  is derived from the usual free electron relationship,  $K_f = [E_f 2m/\hbar^2]^{1/2}$ .

Fig. 41 displays the results of the uranium t-matrix calculation with the measured resistivities of Table 16 for comparison. It should be pointed out that the computation does not depend upon a choice of  $z_{\text{eff}}$ , the number of free electrons per atom, because  $z_{\text{eff}}$  enters in only through  $K_f$  and  $K_f$  is derived from the APW supplied  $E_f$ 's. The most evident result of the calculation is that direct application of Eq. (5-21) with  $m^*/m_e = 1$  yields resistivities that are an order of magnitude above the measured values and show the wrong specific volume dependence. Several factors are eligible contributors to this discrepancy. The calculation is sensitive to the phase shifts used, and it could be that the APW calculations that proved self consistent for compressed uranium are not applicable to the expanded states and therefore supplied inappropriate phase factors. It could also be that the conduction electrons in uranium are inadequately described by the assumed free electron dispersion relationship,  $E = \frac{\hbar^2 K^2}{2m}$ , and that this inadequacy has a pronounced effect on the resistivity.

In an effort to improve the agreement between the t-matrix calculation and measurement a purely pragmatic approach has been adopted. It was heuristically assumed that the phase shift and Fermi energies derived from the APW calculation were truly representative of

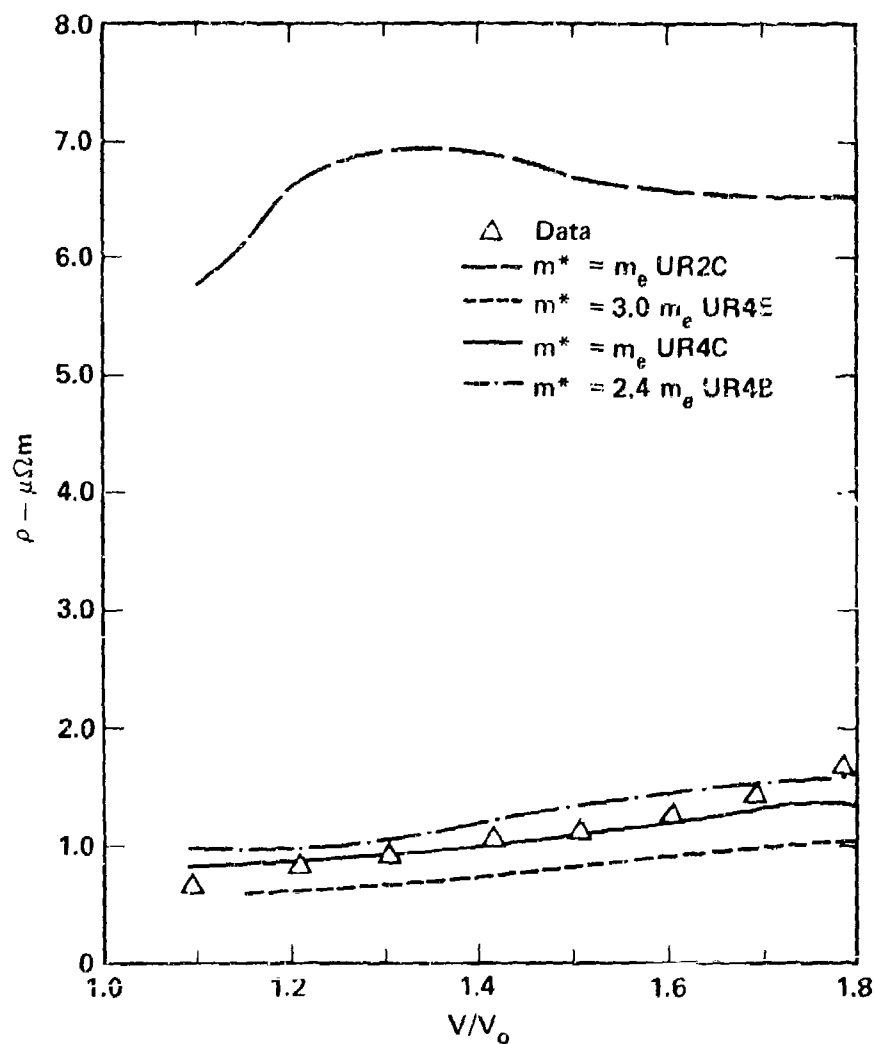


Fig. 41 T-Matrix Calculations on Uranium

T-matrix calculations on uranium are displayed as a function of volume normalized to  $V_0 = 0.052 \text{ cm}^3/\text{gm}$ . Necessary phase shifts and Fermi energies are provided from a selfconsistent APW calculation done by McMahan.<sup>(20)</sup> Results indicate that the data are best modelled with an effective electron mass of  $m^* \approx 2.6 m_e$ .

the physics of liquid uranium. It was further assumed, then, that the computational discrepancies arose from an incorrect assumption on the relationship between  $E_f$  and  $K_f$ , and that good agreement could be produced by varying this relationship. This variation was achieved by retaining the free electron form but changing the effective mass,  $m^*$ , of the electrons. As shown in Fig. 41 it was possible to attain reasonable agreement between theory and measurement by using  $m^*/m_e$  of 2.4 to 3.0. The low specific volume resistivities are well modelled with  $m^*/m_e = 3.0$  while high specific volume requires  $m^*/m_e = 2.4$  for accurate calculation. Resistivities at expansions between 1.2 and 1.6 are best calculated using  $m^*/m_e = 2.6$ . The implication is that whatever the actual configuration of the Fermi surface is it must exhibit a changing curvature with density since  $\frac{1}{m_{ij}^*} = \frac{1}{\hbar^2} \frac{\partial^2 E}{\partial K_i \partial K_j}$ .

One rather subtle dependency of this calculation concerns the effective number of free electrons per ion. As previously pointed out the wave number at the Fermi surface is deduced from the APW calculated Fermi energy. It is also possible to calculate from  $E_f$  a  $z_{\text{eff}}$  through the following relationship: (89)

$$z_{\text{eff}} = \frac{1}{3\pi^2 n} \left[ \frac{2mE_f}{\hbar^2} \right]^{3/2} \quad (5-26)$$

where  $n$  is the ion density. Table 20 lists the APW supplied  $E_f$ 's along with the resulting  $K_f$ 's and  $z_{\text{eff}}$ 's for two choices of effective mass. It can be seen that the use of a specific volume dependent Fermi energy results in an effective charge which also varies with volume. The  $z_{\text{eff}}$  dependency has some intuitive physical validity. One might expect the number of conduction electrons per ion to drop as the density goes

Table 20  
Fermi Surface Parameters of Liquid Uranium

$V/V_0$	$E_f$ joules	$m^*/m_e = 1$		$m^*/m_e = 2.6$	
		$K_f m^{-1}$	$Z_{eff}$	$K_f m^{-1}$	$Z_{eff}$
1.0	$1.73 \times 10^{-18}$	$1.68 \times 10^{10}$	3.34	$2.71 \times 10^{10}$	14.00
1.1	$1.55 \times 10^{-18}$	$1.59 \times 10^{10}$	3.12	$1.57 \times 10^{10}$	13.09
1.2	$1.39 \times 10^{-18}$	$1.51 \times 10^{10}$	2.89	$2.43 \times 10^{10}$	12.10
1.3	$1.24 \times 10^{-18}$	$1.43 \times 10^{10}$	2.65	$2.30 \times 10^{10}$	11.10
1.4	$1.11 \times 10^{-18}$	$1.35 \times 10^{10}$	2.42	$2.13 \times 10^{10}$	9.76
1.5	$1.00 \times 10^{-18}$	$1.28 \times 10^{10}$	2.20	$2.06 \times 10^{10}$	9.23
1.6	$9.02 \times 10^{-19}$	$1.22 \times 10^{10}$	2.01	$1.96 \times 10^{10}$	8.44
1.7	$8.20 \times 10^{-19}$	$1.16 \times 10^{10}$	1.85	$1.87 \times 10^{10}$	7.77
1.8	$7.54 \times 10^{-19}$	$1.11 \times 10^{10}$	1.73	$1.79 \times 10^{10}$	7.25
1.9	$7.04 \times 10^{-19}$	$1.07 \times 10^{10}$	1.65	$1.73 \times 10^{10}$	6.91
2.0	$6.70 \times 10^{-19}$	$1.05 \times 10^{10}$	1.61	$2.00 \times 10^{10}$	6.75

down because the "free" electrons should associate themselves more and more with individual ionic cores. In the limit of large separation there should remain only neutral atoms and no shared electrons. In uranium there are three 5f, one 6d, and two 7s electrons which might exist at energies within the conduction band. The normal density  $z_{\text{eff}}$  of 14 necessary to compute a reasonable resistivity seems too high while  $z_{\text{eff}} = 3.34$  implied by the  $m^*/m_e = 1$  calculation is low. These values are merely artifacts of forcing the nonsimple uranium conduction electrons into the free electron formalism.

Another feature that warrants some examination is the dependence of the resistivity upon effective mass. As revealed in Eqs. (5-21) and (5-22) the electron mass enters directly into the resistivity both through the t-matrix and in the coefficients of the q-space integral. The coefficient term  $v_f^2$  contributes an  $m^2$  dependence through the relation  $mv_f = \hbar K_f$  while the squared magnitude of the t-matrix is proportional to  $m^{-3}$  for an overall  $m^{-1}$  resistivity dependence. Intuitively, larger electron masses should result in more lethargic transport yielding higher resistivities. In opposition to and overriding this effect is the lessened scattering of the higher masses. The net effect in this formulation is a resistivity that decreases with effective mass.

A perplexing result that awaits better knowledge of the liquid state dispersion relationship is the fact that higher effective masses better model higher density states while slightly lower masses are needed to calculate the lower density states. Through the definition,  $\frac{1}{m_{ij}^*} = \frac{1}{\hbar^2} \frac{\partial^2 E}{\partial K_i \partial K_j}$ , larger effective masses correspond to dispersion

relationships with little curvature, or "flat bands" as they are known. Free electrons, having a parabolic dispersion function, have more curvature meaning smaller effective masses. Physical reasoning would indicate that the behavior of the conduction electrons should be more free electron like near normal density but should move to higher masses as the material expanded. The calculation indicates the opposite trend.

In summary, the t-matrix resistivity calculation using APW generated phase factors and Fermi energies produces resistivities with both the wrong magnitude and wrong specific volume dependency. Due to the assumed complex nature of the conduction electrons it was deemed reasonable to model them as other than free electrons through the choice of a larger effective mass. An effective mass of 2.6 led to good agreement with measurement but did not reproduce exactly the right volume dependency. Although there is a measure of volume dependence in the calculation through the volume dependent Fermi overall energies, it is not strong enough to correctly reproduce measured values. As with the screened-ion pseudo-potential lead results the t-matrix uranium calculations are good over a limited expansion range but fail to effectively model the high temperature low density liquid resistivities.

## 6. RECOMMENDATIONS

The discussions of the previous chapters have supported the concept of making equation of state and resistivity measurements on equilibrium states of liquid metals. Accurate reproducible results have been reported for six materials, the confidence level being sufficiently high to deduce even derivative quantities in some cases (see Table 1). A new temperature determining technique has been developed and applied to a range of materials which presented a variety of pyrometric problems. Finally the experimental results have been used to make pseudo-potential and t-matrix calculations for the resistivities of liquid lead and liquid uranium, respectively. In each of these areas several avenues of investigation have presented themselves which, for one reason or another, have not been completely examined at this time. The interesting but unresolved issues fall naturally into three categories—projected improvements to the experiment and experimental techniques, further refinements on the reported data, and projected uses for the wealth of data made available here for the first time. This chapter is a brief discussion of points thought to warrant further pursuit.

### Experimental Improvements

The high temperature fast pyrometry is an area that would benefit most from further development. Although the consistency of the data is quite good the calibration technique could be improved. Currently intensity calibration is accomplished with Wratten neutral density filters which are susceptible to damage and rather imprecisely characterized. The use of better grade glass filters would improve the pyrometer response voltage to intensity transfer function.

Probably the largest contributor to inaccuracy in the temperature measurement is the current method of establishing a temperature calibration point. As has been discussed for much of these data a calibration point was fixed by extrapolating published lower temperature data to a temperature within the range of good pyrometer response. This of necessity meant extending known data approximately 1000 K with estimated specific heats. While the technique involved some iteration to ensure a smooth joining of the new data to the old, the uncertainty was always greater for this procedure than for the cases in which a high temperature melting transition provided a "self" calibration point (see Eq. 3-10). What is needed then is a method of superimposing the intensity of a known standard radiator on the data trace. Initial attempts to do this involved running a tantalum standard in conjunction with each data run and assuming that the pyrometric voltage measured at the tantalum melting plateau could be used to establish a similar point in the data trace. In practice the intensity corresponding to the tantalum melting temperature in the unknown sample was found as follows:

$$I_i(T_c)|_{\text{unknown}} = \frac{I_i(T_c)|_{\text{Tant.}} \epsilon_{\text{unk}}(\lambda_i, T_c)}{\epsilon_{\text{Tant.}}(\lambda_i, T_c)} \quad (6-1)$$

where  $I_i(T_c)|_{\text{unknown}}$  and  $I_i(T_c)|_{\text{tantalum}}$  are intensities for the unknown and tantalum, respectively.  $I_i(T_c)|_{\text{unknown}}$  is then used in Eq. (3-10) to find the calibration factor,  $G_i$ .

There are at least two problems with this calibration technique. First  $\epsilon_{\text{unk}}(\lambda_i, T_c)$ , the emissivity of the sample at the tantalum melting temperature, is unknown and must be estimated. Secondly, the response of the pyrometers must be assumed to remain unchanged over the



long times necessary to perform the two experimental runs. It was these considerations that made the extrapolated calibration point method seem attractive. Fortunately, relatively large errors in the estimated emissivity,  $\epsilon_{\text{unk}}(\lambda_i, T_c)$ , result in much smaller errors in the computed temperatures. Therefore, it would be fruitful to compare temperatures calculated with a tantalum calibration to those calculated with a calibration taken from previous low temperature data. For the tantalum calibration it is important that both  $I_i(T_c)|_{\text{unknown}}$  and  $I_i(T_c)|_{\text{tantalum}}$  be computed using the same pyrometer voltage to relative intensity transfer function. Agreement of these two sets of temperatures would give added confidence in the measurement.

The objective of obtaining the full range of temperatures on one pyrometer trace should be abandoned in favor of optimizing the measurement to either the low or high temperatures. All available sample radiation would be used for the low temperature measurement while well characterized neutral density filters could be used to attenuate the radiation for high temperature readings. Separate runs made to optimize either end of the temperature scale would overlap in the intermediate temperature ranges and could be correlated through measured enthalpy. The high temperature run would thus be calibrated on the low temperature data in the same way that current measurements are calibrated on published data.

One of the unresolved experimental issues is the inconsistent occurrence of baseline offset in the pyrometry traces. As illustrated in Fig. 8 the pyrometer baseline is recorded during the initial stages of the scope sweep from before the resistive heating is started until the sample temperature is high enough to cause the emitted radiation to be

above minimum detector response. Infrequently this baseline suffers an irregular deflection due either to electrical noise or to a spurious optical signal. Even though it may last but a few microseconds the noise signal destroys the record of the baseline and renders the remaining trace unusable since all data measurements must be made with respect to the baseline (see Appendix B). It is very unlikely that the baseline shifts on the timescale of the experiment (100  $\mu$ sec) but the loss of the early record to noise makes it necessary to sample the baseline at some later time in the trace. The short experimental times and the relatively slow (0.3  $\mu$ sec)<sup>(12)</sup> pyrometer response times make intermittent chopping of the sample radiation unfeasible. However, an electro-optical shutter could be placed between the sample and the end of the fibre optics bundle (see Fig. 11) which could be timed to open before the scopes are triggered and close 60-100  $\mu$ sec after the heating is initiated. This shuttering of the sample radiation would place an additional record of the baseline on the pyrometer data trace.

Better accuracy could be achieved by abandoning the logarithmic amplifiers in favor of linear amplifiers. The sample intensity within the spectral window of a pyrometer channel may vary by as much as five to seven orders of magnitude over the temperature range of an experiment, making logarithmic amplification an attractive choice. To cover this temperature range with linear amplifiers would require a series of oscilloscopes each adjusted to receive an individual order of magnitude signal. Current logarithmic signals range up to 2.5 volts with a 1 volt baseline offset meaning that linearly amplified signals for a similar gain would require oscilloscope settings to achieve full scale ranges of

0-2 volts, 0-20 volts, 0-200 volts, and 0-2000 volts to adequately cover the sample intensity.

#### Projected Data and Calculational Refinements

One of the most interesting aspects of the experimental work of this project is the capability to characterize those states near the liquid vapor two phase boundary. If the assumptions as discussed in Chapter 4 are valid it is within the realm of possibility to determine the equation of state parameters at or near the two phase boundary. In cases where the critical point lies within the attainable pressure range it should be possible to measure the critical point parameters to an accuracy determined by the amount of data taken. In the work reported here only lead has received the experimentation necessary to locate the two phase boundary with acceptable accuracy. To increase this accuracy additional specific volume measurements (streak photography) need to be made at pressures of 0.1 GPa and below and between 0.2 and 0.3 GPa. Additional temperature data are also needed for expansions above  $V/V_0 = 2.3$ . These added data and possible soft sphere modelling should establish the critical point of lead more accurately than has been done for any metal to this date. (5)

Among the materials studied here the next most likely subject for further investigation of the liquid vapor two phase boundary is niobium. Although estimates place the critical point parameters of niobium at the limits of IEX experimental capability it should be relatively easy to locate the low pressure portion of the liquid phase boundary with accuracy. These data should enable a further refinement of the currently

estimated parameters:  $T_C = 9989\text{K}$ ,  $V_C/V_0 = 4.25$ , and  $p_C = 0.963$  GPa. <sup>(5)</sup>

In this paper are no reported temperatures above 8000 K. In the case of some of the materials, e.g. Au-Cu and Pt, higher temperatures were measured than were reported because the reliability of the highest temperatures was not comparable to the other data. Confidence in these higher temperature measurements can be readily improved through two refinements. First, as discussed in the last section the highest temperature sample emission can be attenuated with neutral density filters to bring it within the range of good detector sensitivity. Secondly, the exhaustive thermal transport calculation alluded to in Chapter 2 needs to be done in order to establish the credibility of the higher temperatures.

The temperature determining technique being newly developed could benefit from further study. In addition to the comparison of calibration techniques suggested in the previous section certain parametric sensitivities could be more closely defined. Calculations could be made to establish exactly the effect of calibration point errors in the computed temperatures over the range of the data. A second study might be made to more closely evaluate the effect of choosing the calibration temperature at a range of values.

#### Applications of the Reported Data

The major value of this work lies in the wealth of data presented on highly expanded liquid metals. Opportunities for exploiting this information have only begun to be realized. A major use is in formulating equations of state as has been begun by Grover <sup>(39)</sup> and

Young<sup>(5)</sup>. The formulation of such equations of state are carried out in a semi-empirical manner and require data to determine adjustable parameters. A first principles approach to equation of state development is being pursued by Ross<sup>(21)</sup> in which the current data are necessary to choosing suitable interaction potentials for liquid metals. "MET" calculations are just begun and should be pursued as a means of gaining theoretical insight as well as producing engineering data.

As a project in itself calculations of liquid metal resistivity should be continued for lead and uranium and initiated for the other four materials. Further calculations should define the limits of applicability for both pseudo-potential and t-matrix calculations. Use of the t-matrix theory will require new APW calculations which would preferably be carried out for expanded rather than compressed states. A principal objective should be to unfold the effects of mass and effective charge, possibly developing a volume dependence for each. An optimistic result might be to correctly model the low density resistivity and the metal to insulator (Mott) transition.

## REFERENCES

1. J. G. Linhart, "Acceleration of Projectiles to Hypervelocity", Proceedings of the International School of Physics (Enrico Fermi), Course XLV III, Physics of High Energy Density, pg. 151 (1971).
2. Brueckner, K. A., S. Jorna, "Laser-Driven Fusion", Reviews of Modern Physics, 46, 325-367, April 1974.
3. Linhart, J. G., "Very-High-Density Plasmas for Thermonuclear Fusion", Nuclear Fusion 10, 211 (1970).
4. Young, D. A., B. J. Alder, "Critical Point of Metals from the van der Waals Model", Phys. Rev. A 3, 364-371 (1971).
5. Young, D. A., "A Soft Sphere Model for Liquid Metals", University of California, Lawrence Livermore Laboratory, UCRL-52352 (1977).
6. Barker, J. A., D. Henderson, "What is 'Liquid'? Understanding the States of Matter", Rev. of Modern Physics 48, 587 (1976).
7. Kirshenbaum, A. D., J. A. Cahill, A. V. Grosse, "The Density of Liquid Lead from the Melting Point to the Normal Boiling Point", J. Inorg. Nucl. Chem. 22, 33 (1961).
8. Cezairliyan, A., "Design and Operational Characteristics of a High Speed (Millisecond) System for the Measurement of Thermophysical Properties at High Temperatures", J. of Research of the National Bureau of Standards - C. Engineering and Instrumentation, 75C, 7 (1971).
9. Vermij, "The Melting Process of Current Carrying Cylindrical Metal Conductors", Z. Angew. Physik. 28, Bd., Heft 6, page 316 (1970).

10. Henry, K. W., "A Technique for Measuring the Pressure, Volume, Enthalpy and Resistance of Equilibrium Thermodynamic States of Liquid Metals at High Temperatures and Pressures", Univ. of Calif. Lawrence Livermore Laboratory, UCRL-51035, PhD Thesis (1971).
11. Henry, K. W., D. R. Stephens, D. J. Steinberg and E. B. Royce, "A Technique for Measuring Equilibrium Thermodynamic States of Liquid Metals at High Temperatures and Pressures", Rev. of Sci. Inst., 43, 1777 (1972).
12. Gathers, G. R., J. W. Shaner and R. L. Brier, "Improved Apparatus for Thermophysical Measurements on Liquid Metals up to  $8000^{\circ}\text{K}$ ", Rev. of Sci. Inst., 47, 471 (1976).
13. Gathers, G. R., J. W. Shaner and D. A. Young, "Experimental, Very High-Temperature, Liquid-Uranium Equation of State", Phys. Rev. Letters 33, 70 (1974).
14. Shaner, J. W., G. R. Gathers and C. Minichino, "A New Apparatus for Thermophysical Measurements above  $2500^{\circ}\text{K}$ ", High Temp-High Press 8, 425 (1976).
15. Shaner, J. W., G. R. Gathers and W. M. Hodgson, "Thermophysical Measurements on Liquid Metals above  $4000^{\circ}\text{K}$ ", in Proceedings of the 7th Symposium on Thermophysical Properties, Ared Cezairliyan, ed., Am. Soc. Mech. Eng., New York (1977).
16. Lincoln, R. C. and R. B. Pettit, "A Two-Wavelength Technique for the Simultaneous Measurements of High Temperature and the Temperature Dependence of Spectral Emittance", High Temp-High Pres 5, 421 (1973).
17. Ziman, J. M., "The Method of Neutral Pseudo-Atoms in the Theory of Metals", Advances in Physics 13, 89-138 (1974).

18. Ashcroft, N. W., "Electron-Ion Pseudopotentials in Metals", Phys. Lett. 23, 48 (1966).
19. Hirata, K., Y., Waseda, A. Jain and R. Srnastava, "Resistivity of Liquid Transition Metals and Their Alloys using the T-Matrix", J. Phys. F: Metal Phys. 7, 419 (1977).
20. McMahan, A., private communication, 1978.
21. Ross, M., "MET", unpublished computer code, 1978.
22. McQueen, R. G., S. P. Marsh, J. W. Taylor and J. N. Fritz, "The Equation of State of Solids from Shock Wave Studies", High-Velocity Impact Phenomena, R. Kinslow, ed., (Academic Press, 1970) pp. 294-415.
23. Shaner, J. W., G. R. Gathers and C. Minichino, "Thermophysical Properties of Liquid Tantalum and Molybdenum", High Temp-High Press 9, (1977).
24. Jackson, J. D., Classical Electrodynamics, 2nd Edition (John Wiley & Sons, 1975) pp. 482-490.
25. See e.g., Adamson, A. W., A Textbook of Physical Chemistry (Academic Press, 1973) pp. 67-68.
26. See e.g., Kittel, C., Introduction to Solid State Physics, 4th Edition (John Wiley & Sons, 1971) pp. 263-264.
27. American Institute of Physics Handbook, 3rd Edition (McGraw-Hill, 1973) pp. 2-15.
28. Ref. 27, pp. 2-208.
29. Gathers, G. R., EOSDTA, Fortran computer code, unpublished, 1978.
30. Stratton, J. A., Electromagnetic Theory (McGraw-Hill, 1941), pp. 553.
31. Jenkins, F. A. and H. E. White, Fundamentals of Optics (McGraw-Hill, 1976) pp. 396.



32. See e.g., Harrison, T. R., Radiation Pyrometry and its Underlying Principles of Radiant Heat Transfer (John Wiley & Sons, 1960) p. 31.
33. Knox, R. J., "Curve", University of California, Lawrence Livermore Laboratory, UR-505, Rev. 1 (1973).
34. Hultgren, R., P. De. DeSai, D. T. Hawkins, M. Gleiser, K. K. Kelley, D. D. Wagman, Selected Values of the Thermodynamic Properties of the Elements, 1973, p. 382.
35. Gschneidner, K. A., Jr., "Physical Properties and Interrelationships of Metallic and Semimetallic Elements", in Solid State Physics Advances in Research and Applications, Vol. 16, 1964, p. 315.
36. Cezairliyan, A., J. L. McClure, I. Coslovi, F. Righini, A. Rosso, "Radiance Temperature of Tantalum at its Melting Point", High Temp-High Press 8, 103 (1976).
37. Lucas, L. D., "Densite' de Me'taux a' Haute Temperature (dans les 'etats solide et liquide)", Mem. Sci. Rev. Metallurg. 69, 395-409 (1972).
38. Cordoba, C. and C. R. Brooks, "Heat Capacity of Lead from 300° to 850° K", Phys. Stat. Sol. (a) 7, 503 (1971).
39. Grover, Richard, "High Temperature Equation of State for Simple Metals, Proceedings of the Seventh Symposium on Thermophysical Properties, Washington, D.C., May 10-12, 1977.
40. Grover, Richard, "Liquid Metal Equation of State Based on Scaling", J. of Chem. Phys. 55, 3435 (1971).
41. Royce, E. B., "GRAY A Three-Phase Equation of State for Metals", Univ. of Calif. Lawrence Livermore Laboratory UCRL-51121 (1971).
42. Ashcroft, N. W., and N. D. Mermin, Solid State Physics (Holt, Rinehart, and Winston, 1976) p. 47.
43. Ref. 42, page 493.

44. Ross, Marvin, "The Electrical Conductivity of Liquid Aluminum", Univ. of Calif. Lawrence Livermore Laboratory UCRL-51322, January (1973).
45. Fortov, V. E., Moscow, personal communication via J. W. Shaner, 1977.
46. Fortov, V. E., A. N. Dremin, A. A. Leont'ev, "Evaluation of the Parameters of the Critical Point", High Press-High Temp, Translated from Teplofizika Vysokokh Temperatur 13, 5, 1072-1080 (1976).
47. Ashcroft, N. W. and J. Lekner, "Structure and Resistivity of Liquid Metals", Phys. Rev. 145, 83-90 (1966).
48. Banchila, S. N. and L. P. Filippov, "Study of the Electrical Conductivity of Liquid Metals", High Temperature 11, 1166 (1974), translated from Teplofizika Vysokikh Temperatur 11, 1301-1305 (1973).
49. Waseda, Y., K. Hirata and M. Ohtani, "High Temperature Thermal Expansion of Platinum, Tantalum, Molybdenum and Tungsten Measured by X-ray Diffraction", High Temp-High Press 7, 221 (1975).
50. Ref. 34, page 398.
51. Lucas, L. D., "Densite' de l'argent, du cuivre, du palladium et du platine a l'etat liquide", Comptes Rendus Academic des Sciences, 253, 2526 (1961) (in French).
52. Dubinin, E. L., V. M. Vlasov, A. I. Timofeev, S. O. Safonov, and A. I. Chegodaev, Izv. V. U. Z. Tsvetn. Metall. 1975 (4) 160-161 (in Russian).
53. Shaner, J. W. and G. R. Gathers, "Thermophysical and Transport Properties of Metals at High Pressure and Very High Temperature", Proceedings of the Sixth AIRAPT International High Pressure Conference, Boulder, Colorado, July 25-29, 1977.
54. Ref. 27, page 9-39.
55. Ref. 34, page 50.

56. Hansen, M., and K. Anderko, Constitution of Binary Alloys, 2nd Edition (McGraw-Hill, 1958) p. 199.
57. Ref. 35, page 313.
58. Stephens, H. P., "Determination of the Enthalpy of Liquid Copper and Uranium with a Liquid Argon Calorimeter", High Temp. Sci. 6, 156-166 (1974).
59. Shaner, J. W. and G. R. Gathers, unpublished, 1978.
60. Thermophysical Properties of High Temperature Solid Materials, Y. S. Touloukian, ed. (MacMillan, New York, 1967) Vol. 1, p. 1058.
61. Ref. 34, page 538.
62. Rohr, W. G. and L. I. Wittenberg, J. Phys. Chem. 74, 1151 (1970).
63. Cezairliyan, Ared, "Radiance Temperature of Niobium at its Melting Point", Journal of Research of the National Bureau of Standards - A. Physics and Chemistry, 77A, 3, p. 333 (May-June 1973).
64. Cezairliyan, Ared, "High-Speed (Subsecond) Measurement of Heat Capacity, Electrical Resistivity and Thermal Radiation Properties of Niobium in the Range 1500 to 2700K", Journal of Research of the National Bureau of Standards - A. Physics and Chemistry, 75A, p. 565 (1971).
65. Sheindlin, A. E., B. YaBerezin, V. YaChekhovskoi, "Enthalpy of Niobium in the Solid and Liquid State", High Temp-High Press 4, 611 (1972).
66. Savvatimskii, A. I., "Heat of Melting and Electrical Conductivity of Niobium and Rhodium at the Melting Point", High Temperature, 11, 1057 (1972). (Translation of Teplofizika Vysokikh Temperatur, 11, 1182 (1972)).
67. Shaner, J. W. and G. R. Gathers, unpublished data, 1978.

68. Dreidach, O., R. Evans, H.-J. Guntheradt and H.-U. Kunzi, "A Simple Muffin Tin Model for the Electrical Resistivity of Liquid Noble and Transition Metals and their Alloys", *Journal of Physics F: Metal Physics*, 2, 709 (July 1972).
69. Jones, H. D., "Theory of the Thermodynamic Properties of Liquid Metals", *Phys. Rev. A* 8, 3215 (1973).
70. Reif, F., Fundamentals of Statistical and Thermal Physics (McGraw-Hill, 1965) pp. 488-490.
71. Mott, N. F. and H. Jones, The Theory of the Properties of Metals and Alloys, (Dover Publications Inc., 1958) pp. 258-262.
72. See e.g., Eisberg, R. M., Fundamentals of Modern Physics (John Wiley & Sons, Inc., New York) pp. 285-291.
73. Harrison, Walter A., Pseudopotentials in the Theory of Metals (W. A. Benjamin, Inc., 1966) p. 31.
74. Sharrah, P. C., and G. P. Smith, "Neutron Diffraction and Atomic Distribution in Liquid Lead and Liquid Bismuth at Two Temperatures", *J. Chem. Phys.* 21, 228-232 (1953).
75. North, D. M., J. E. Enderby and P. A. Egelstaff, "The Structure Factor for Liquid Metals: II. Results for Liquid Zn, Tl, Pb, Sn and Bi", *J. Phys. C* 1, 1075 (1968).
76. Ref. 73, page 298.
77. Egelstaff, P. A., An Introduction to the Liquid State (Academic Press, 1967) pp. 43 ff.
78. Wallace, Duane C., "Dependence of Phonon Frequencies on the Pseudopotential Form Factor for Aluminum", *Phys. Rev.* 87, 999 (1969).
79. Animalu, A. D. E., and V. Heine, "The Screened Model Potential for 25 Elements", *Philosophical Magazine* 12, 1249 (1965).

80. Sundstrom, Lorna J., "A Theory of the Electrical Properties of Liquid Metals IV. Quantitative Calculations of Resistivity and Thermoelectric Power", Philosophical Mag. 11, 665 (1965).
81. Evans, R., "The Resistivity and Thermopower of Liquid Mercury and Its Alloys", J. of Phys. C: Metal Physics, Supplement 2, 5137 (1970).
82. Ref. 73, page 49.
83. Hubbard, J., "The Description of Collective Motions in Terms of Many Body Perturbation Theory II. The Correlation Energy of a Free-Electron Gas", Proceedings of the Royal Society A243, 336 (1958).
84. Sham, L. J., "A Calculation of the Phonon Frequencies in Sodium", Proceedings of the Royal Society A282, 33 (1964).
85. Brovman, E. G., Yu.Kagan and A. Kholas, "Properties of Alkalai Metals", Soviet Physics-Solid State 12, 786 (1970).
86. Ref. 73, pp. 302-303.
87. Benedek, Roy , "Core Overlap Interactions in Metals", Phys. Rev. B 15, 2902 (1977).
88. Ref. 24, page 767.
89. Ref. 26, page 247.
90. Ref. 73, pp. 46-49.

## ACKNOWLEDGEMENTS

I take this opportunity to recognize the contributions of the many whose assistance has been so beneficial to me and this thesis project. I especially appreciate the guidance and inspiration of Dr. J. W. Shaner, my thesis advisor, who generously allowed me many times a fair share of his time while aiding my understanding of experimental physics. Thanks go to Dr. G. R. Gathers for contributing his excellent experimental and computational skills to my problems when called upon. Deep appreciation and thanks are extended to Mr. V. Morasch and Mr. E. Romero who with exceptional ability and resourcefulness transformed ideas into physical reality. Thanks go to Mr. J. Dub and others who helped make the complex electronics of the system function. Dr. D. A. Young, Dr. A. McMahan, Mr. R. Grover, and Dr. M. Ross contributed many hours to discussing liquid metal theory with me for which I am most appreciative. Special thanks to the John and Fannie Hertz Foundation and the U. S. Air Force whose financial support have made my education and this project possible. Ms. Kathy Rieser has cheerfully and accurately typed the thesis through many rewritings and I thank her. And finally I express my deepest appreciation and sincere thanks to my children, Greg and Lisa, for their love and support through all the pressures of student life.

## APPENDIX A. TEMPERATURE UNCERTAINTIES

The sample temperature measurement is subject to four major sources of error which act both singly and in concert to determine the final uncertainty in a given temperature. Factors to be considered are random measurement imprecision, systematic errors caused by instrument limitations, the systematic effects of less than perfect calibration techniques, and the limits on accuracy imposed by the functional relationship between temperature and radiated energy. Although some effects are most significant in only narrow parts of the temperature range the calibration technique and the full range criterion for determining the unknown emissivity parameters tend to make problems of one temperature region important to all the calculated temperatures.

The temperature determining scheme rests upon the coupled solution of Eqs. (3-12) and (3-13). Recognizing the equivalence of Eq. (3-8) to (3-12) the former may be written as:

$$I_i(T) = G_i \epsilon(\lambda_i, T) F_i(T) = G_i \epsilon(\lambda_i, T_c) [1 + a_i(T - T_c)] F_i(T)$$

Since it is difficult to extract the individual parameters  $G_i$  and  $\epsilon(\lambda_i, T_c)$  from their product no information is lost if the intensity is expressed as:

$$I_i(T) = G_i \alpha_i(T) F_i(T)$$

where  $\alpha_i(T) = 1 + a_i(T - T_C)$  and  $G_i$  has been redefined to designate the product  $G_i \varepsilon(\lambda_i, T_C)$ . With these changes in nomenclature the uncertainty of the SCT temperatures is given by:

$$\Delta T_i = \left[ \frac{\Delta I_i}{I_i} + \frac{\Delta G_i}{G_i} \right] \left[ \frac{a_i}{1 + a_i(T - T_C)} + \frac{\partial F_i}{\partial T} / F_i \right]^{-1} \quad (A-1)$$

where the error in the temperature dependence of the emissivity is:

$$\frac{\Delta \alpha_i}{\alpha_i} = \frac{a_i}{1 + a_i(T - T_C)} \quad (A-2)$$

The uncertainties of  $\varepsilon(\lambda_i, T_C)$  and  $G_i$  derive from a variety of sources and have been combined into  $\Delta G_i/G_i$ .

In order to simplify the expression for the TCT temperature uncertainty Eq. (3-13) may be rewritten as:

$$R_{i,j} = G_{i,j} \frac{[1 + a_i(T - T_C)]}{[1 + a_j(T - T_C)]} F_{i,j} \quad (A-3)$$

$R_{i,j}$  is the ratio of measured intensities in channels  $i$  and  $j$ ,  $G_{i,j} = \frac{I_i(T_C) F_j(T_C)}{I_i(T_C) F_i(T_C)}$  and  $F_{i,j}$  is the ratio of blackbody functions. Uncertainty in the TCT temperature is then:

$$\Delta T_{i,j} = \left[ \frac{\Delta R_{i,j}}{R_{i,j}} + \frac{\Delta G_{i,j}}{G_{i,j}} \right] \left\{ \frac{a_i - a_j}{[1 + a_i(T - T_C)][1 + a_j(T - T_C)]} + \frac{\partial F_{i,j}}{\partial T} / F_{i,j} \right\}^{-1} \quad (A-4)$$

$\Delta T_i$  and  $\Delta T_{i,j}$  as defined by Eqs. (A-1) and (A-4) are the total error in the temperatures to include all measurement imprecision and systematic inaccuracies.



The least significant contributor to the magnitude of either  $\Delta T_i$  or  $\Delta T_{i,j}$  is the imprecision in obtaining a true voltage from the oscilloscope trace. Careful calibration of the time and voltage axes for each experimental run reduce this random error to much less than 1%. Much more serious is the issue of translating these voltages into a correct sample intensity. As detailed in Chapter 3 this voltage to intensity conversion entails constructing an accurate intensity scale which in turn depends on having an extremely stable laser source, taking standard intensity measurements without any hard to recognize mistakes, and reading the intensity scale precisely. Sample emissions in some cases may produce a maximum pyrometer response above 2.5-2.7 volts which corresponds to complete saturation of the photo diode. The low end of the detector response curve is unreliable because of a small signal to noise ratio. Therefore,  $\Delta I_i/I_i$  and  $\Delta R_{i,j}/R_{i,j}$  are estimated to be 5% and 10%, respectively, except at the extremes of the voltage scales where they become prohibitively large.

Uncertainties in calibration are characterized by  $\Delta G_i/G_i$  and  $\Delta G_{i,j}/G_{i,j}$ . The calibration schemes outlined in Chapter 3 in some sense represent a compromise between conflicting requirements. With the current pyrometer configuration the most precise calibration is achieved with a material which melts at a temperature that produces a response of 1.0-2.0 volts, i.e. at the center of the detector range. Depending on emissivities a 1.0 volt response corresponds to a temperature in the neighborhood of 3000 K. Of the materials in this study only Nb and NbHf which melt near 2750 K exhibit an identifiable trace feature in a range where the measured intensities are reliable enough to be used for calibration purposes. Evidence of the melting plateau ( $T_C = 2045$  K)

was always seen in the platinum data but occurred too near minimum detector response to be used reliably for calibration. All other materials melted at lower temperatures. Therefore, the calibration of all but the niobium and NbHf data was done by extrapolating published low temperature-enthalpy data to temperatures of 2600 K to 3000 K. For all cases except uranium this involved an extrapolation of over 1000 K which provided the opportunity for a significant error. To minimize this error heat capacities were chosen that agreed well with the new data and the published data. The choice of a calibration temperature lower than 2600 K would mean a shorter range extrapolation but the associated calibrating intensities were found to be too unreliable to produce consistent temperatures. Even then the calibration temperatures are near an unreliable region of instrument response so  $\Delta G_i/G_i$  and  $\Delta G_{i,j}/G_{i,j}$  are estimated at 10% and 20%, respectively.

The factors  $\frac{\partial F_i}{\partial T}/F_i$  and  $\frac{\partial F_{i,j}}{\partial T}/F_{i,j}$  are the normalized rates at which the blackbody functions change as a function of temperature. These are numerically evaluated functions and depend very sensitively on the temperature and the spectral range encompassed by a particular interference filter. In calculating the percentage error,  $\Delta T_i/T_i$ , the relevant parameters are the above discussed rates times the temperature at which they are evaluated. To illustrate the significance of these parameters Table A-1 presents values calculated for the lead analyses of Chapter 4. It can be seen that the temperature dependence of the blackbody function provides a demagnification of the uncertainties associated with the SCT temperatures. This beneficial demagnification lessens as the temperature increases and the blackbody peak moves to shorter wavelengths. The situation is not so fortunate for the TCT

temperatures where the weak temperature dependence of the blackbody function actually magnifies the uncertainties over much of the useful temperature range of the pyrometers. For this reason the TCT temperatures have proven much less reliable than the SCT temperatures.

Table A-1. Lead Blackbody Uncertainty Factors

T	$T \frac{\partial F_i}{\partial T} / F_i$		$T \frac{\partial F_{i,j}}{\partial T} / F_{i,j}$	
	$\lambda_i=450$	$\lambda_i=600$	$\lambda_i=650$	$\lambda_i/\lambda_j \approx 600/650$
2000	15.44	11.89	10.32	1.57
4000	7.86	6.04	5.24	.80
6000	5.30	4.10	3.59	.52

The range of the emissivity parameter,  $a_i$ , that is investigated in finding the true sample temperatures is chosen based upon the full scale temperature agreement criterion. In other words that set of  $a_i$ 's, one for each channel, that gives the best agreement among the three independent SCT temperatures and two independent TCT temperatures over the entire temperature range of the experiment is the one chosen to specify the temperatures dependence of the emissivities. In practice the emissivity temperature dependence was found to be rather weak so that a typical  $a_i$  value gave an emissivity variation of no more than 20% over a temperature range of 3400 K. Referencing Eq. (3-11) usual  $a_i$ 's are less than  $6 \times 10^{-5} \text{K}^{-1}$ . A conservative estimate of the importance of the  $a_i$  parameters is found by comparing  $a_i T$  to  $(-\frac{\partial F_i}{\partial T} / F_i) T$ . Using the values in Table A-1 it can be seen that the term involving the emissivity parameters in the denominators of Eqs. (A-1) and (A-4) is never more than 10% of the other term in the denominator and therefore is ignored in evaluating the uncertainties in the SCT and TCT temperatures.

With these discussed considerations the total uncertainty in the SCT temperatures for the case of lead illustrated in Figure 13 is 5% at 2000 K, 2-3% at 4000 K, and 3-4% at 6000 K. The uncertainty in the TCT temperature is 58% at 2000 K, 50% at 4000 K, and 116% at 6000 K. Although the analyses have been admittedly conservative the uncertainties illustrate the primary issues in determining sample temperatures with fast radiation pyrometry. The confidence in the SCT temperatures is well founded while the usefulness of the TCT temperatures is severely compromised by an unfavorable functional relationship and the cumulative effects of many measurements and computations.

The specification of temperature uncertainties is incomplete without identifying areas of possible consequence which are not adequately accounted for in this analyses. One such issue concerns the stability of the pyrometer baseline as the pyrometer is subjected to a rather violently dynamic electromagnetic field environment. The pyrometer amplifier was designed to provide a stable reference voltage.<sup>(12)</sup> However, evidence of baseline shifts was encountered in some experimental runs which were discarded for that reason. There exists a possibility, though, that baseline shifts could occur in a region of the trace that would make their detection very difficult. Such shifts would have a significant effect on the uncertainty in the temperatures. The repeatability of the data presented in Chapter 4 reduces the possibility of random baseline fluctuations but does not completely eliminate the risk. A possible diagnostic fix for this problem is suggested in Chapter 6.

A second issue is the reliability of the temperatures measured near the saturation limit of the detectors. Extreme temperatures were

achieved with some samples having an apparently high emissivity also. The emissions of these samples drove the detectors to and beyond saturation, i.e., the point where further intensity caused no further increase in voltage. The antidote for this problem is purely a procedural one and will also be discussed in Chapter 6.

## APPENDIX B. PYRO, A COMPUTER CODE FOR DETERMINING TEMPERATURES

PYRO uses computed blackbody functions (Eq. 3-9) and oscilloscope pyrometer readings to calculate intensities relative to a standard intensity, SCT temperatures, TCT temperatures, and emissivities relative to an undetermined standard emissivity. To simplify the calculations there are three versions of PYRO, one for each of the possible combinations of two channels available from the three data channels. All versions assume linear temperature dependence for the emissivity, and all use the same input card deck. This appendix reveals no new information about fast radiation pyrometry, but is designed to enable the uninitiated user to apply the techniques of Chapter 3. The code contains no computing subtleties, being in fact crude but straightforward. Cubic splines, as computed in subroutine SPLINE, are used for the many times interpolation between discrete data points is required. The code listing is given in sections with explanatory commentary accompanying each section. The version discussed, stored in file PYROLLN, analyzes data from the shortest wavelength channel (Channel 1) and the longest wavelength channel (Channel 3).

```

C
C C
C
PROGRAM PYRO3(TAPE2,HSP,CEROUT,TAPE10=CEROUT,COUT,TAPE15=COUT)
CALL ASSIGN(2,0,4RDATA,0)
CALL ASSIGN(3,15)
CALL CHANGE(5R+MARK)
CALL KEEP80(1)

THE DIMENSION STATEMENTS

DIMENSION RDT(200),RDD(200),DRI(15),DTVX(20),DTVY(20),STVX(20)
DIMENSION STVY(20),C1(251),C2(251),C3(251),C4(251),SEM(3)
DIMENSION CERN(1506),BTEMP(3,200),CTEMP(3,200),RINT(6,200)
DIMENSION TMPC(3),TCERN(251),COMT(200),SMPI(3),C12(251)
DIMENSION C22(251),C32(251),C42(251),C13(251),C23(251),C33(251)
DIMENSION C43(251),EM(3,200),DRI1(15),XND(15),TTIE(3)

```

Each of the variables dimensioned here will be discussed as they are used. The size of the arguments allow up to 200 data points in each of three channels with a resulting 200 computed points for each output SCT or TCT temperature. Space is allotted for 251 calculated blackbody functions for each of three SCT and three TCT temperatures. The program reads these functions from file CEROUT into the one dimensional array CERN in the order channel 1, channel 2, channel 3, channel 1/channel 2, channel 1/channel 3, channel 2/channel 3. This particular version of PYRO then uses functions for channels 1 and 3 and channel 1/channel 3.

```

C      READ(2,10)NTC
      READ(2,11)(SEM(I),I=1,NTC)
10     FORMAT(15)
11     FORMAT(3F10.3)
      READ(2,11)(TMPC(I),I=1,NTC)
      READ(2,48)TLO,THI,NUMT
48     FORMAT(2F10.0,15)
      CHOOSE COMMON TIMES AT WHICH TO COMPUTE INTENSITIES

```

NTC = number of data channels in the calculation. This is almost always 3.

SEM = Time in seconds at which the calibration intensity occurs. This is either the time the center of the melting plateau is reached or the time a calibration enthalpy is reached.

TMPC = Calculated blackbody function for the temperature reached by the sample at time SEM. These values are read from a table of computed functions output by the code ARBPLT.

TLO = Experimental time in seconds at which temperature calculations are to begin.

THI = Latest time in the experiment for which experimental calculations are to be made.

NUMT = Total number of points for which calculations are to be made.

```

C
C
      XT=NUMT
      DT=(THI-TLO)/XT
      COMT(1)=TLO
      DO 49 I=2, NUMT
49      COMT(I)=COMT(I-1)+DT
C      READ THE NUMBER OF CALCULATED KERNELS PER COLOR.
      READ(2,10)NCK
      WRITE(3,23)NCK
23      FORMAT(/,13,38H KERNELS ARE CALCULATED FOR EACH COLOR)
      READ(10,24)(TCERN(I),CERN(I),I=1,NCK)
24      FORMAT(3(E12.4,3X,E12.4,3X))
      READ(10,25)(CERN(I),I=NCK+1,2*NCK)
      READ(10,25)(CERN(I),I=2*NCK+1,3*NCK)
      READ(10,25)(CERN(I),I=3*NCK+1,4*NCK)
      READ(10,25)(CERN(I),I=4*NCK+1,5*NCK)
      READ(10,25)(CERN(I),I=5*NCK+1,6*NCK)
25      FORMAT(3(15X,E12.4,3X))
      WRITE(3,26)5*NCK+1,6*NCK
26      FORMAT(/,19H CALCULATED KERNELS ,14,6H THRU ,14,6H ARE--)
      WRITE(3,27)
27      FORMAT(/,3(3X,9HTEMP (K),9X,6HKERNAL,4X),/)
C      WRITE(3,24)(TCERN(I),CERN(5*NCK+1),I=1,NCK)

```

COMT = Points in experimental time at which temperature is to be calculated.

NCK = Number of computed blackbody functions for each SCT and TCT temperature. This is 251 to agree with the dimension statement.

TCERN = Temperatures for which blackbody functions are calculated.

These are determined by the data on CEROUT and typically range from a low around 1500 K to a high of 9000 K.

CERN = The blackbody functions as computer by ARBPLT.

```

C
5      READ(2,12)NC,NDET,NDP
12      FORMAT(3I5)
      WRITE(3,13)NDET,NC
13      FORMAT(/,33HTEMPERATURE ANALYSIS FOR DETECTOR,13,8H CHANNEL,13)
      WRITE(3,14)NDP
14      FORMAT(/,25HTHE TEMPERATURE CURVE HAS,15,12H DATA POINTS)
      READ(2,15)(RDT(I),RDD(I),I=1,NDP)
15      FORMAT(6F12.3)
      WRITE(3,16)
16      FORMAT(///,3(5X,4HTIME,8X,11HTEMPERATURE,2X),/)
      DO 17 I=2,NDP
      RDT(I)=RDT(I)-RDT(1)

```



```

17  RDD(1)=RDD(1)-RDD(1)
    RDT(1)=0.
    RDD(1)=0.
    WRITE(3,15)(RDT(1),RDD(1),I=1,NDP)

```

NC = Number of the pyrometer channel. This is 1, 2, or 3 depending on the wavelength of the interference filter. The order is shortest wavelength to longest wavelength.

NDEF = The pyrometer used with the NC channel. This is also 1, 2, or 3.

NDP = The number of data points in channel NC.

RDT = Time in microns that a particular reading is made.

RDD = Pyrometer reading in microns. Both RDT and RDD are cards punched by the film reader.

RDT and RDD are converted to measurements with respect to the first read point which is placed on the baseline at the time of bankfire.

```

C      READ(2,18)NR1,NR1L
18     FORMAT(2I5)
      WRITE(3,19)NR1
19     FORMAT(/,21H THE REL INT CURVE HAS,13,12H POINTS MEAS)
      WRITE(3,20)NR1L
20     FORMAT(/,11,35H MOST INTENSE POINTS WERE OFF SCALE)
      READ(2,15)(DRI(I),I=1,NR1)
      DO 21 I=2,NR1
21     DRI(I)=DRI(I)-DRI(1)
      DRI(1)=0.
C      READ THE TIME-VOLTAGE CALIBRATION FOR THE DATA.
      READ(2,15)(DTVX(I),DTVY(I),I=1,18)
22     FORMAT(F10.3)
C
      READ(2,28)DSCALX,DSCALY
28     FORMAT(2F10.3)
      WRITE(3,29)DSCALX
29     FORMAT(/,15H DATA X-SCALE = ,E10.2,8H SECS/CM)
      WRITE(3,30)DSCALY
30     FORMAT(/,15H DATA Y-SCALE = ,E10.2,9H VOLTS/CM)

```

- NRI = Total number of lines on the relative intensity scale. See Figure 14.
- NRIL = Number of most intense lines that are off scale and missing from the picture. Because of electronic variations between the pyrometers if  $I_0$  is adjusted to obtain full scale oscilloscope deflection in one channel it will be off scale in others.
- DRI = Relative intensity deflections in microns. These are immediately converted to distances with respect to the baseline.
- DTVX & DTIVY = x and y positions of 18 points read from the time and voltage calibration film. The points comprise a 7x4 array with the number one point being one up from the bottom on the right (as viewed through the film reader) and successive points read counter-clockwise around the outside of the array ending with the bottom right-hand corner.
- DSCALX = Time in seconds between the time voltage points.
- DSCALY = Vertical space in voltages between the time voltage points.

```

C      CHANGE ALL DATA FROM MICRONS TO VOLTS.
C
C      THE DATA CONVERSION.
C      YSFD=0.
C      DO 33 I=3,9
33     YSFD=YSFD-DTVY(I)+DTVY(I+9)
C      YSFD=21.*DSCALY/YSFD
C      DO 34 I=1,NUP
34     RDD(I)=RDD(I)*YSFD
C      THE RELATIVE INTENSITY
C      DO 35 I=1,NRI
35     DRI(I)=YSFD*DRI(I)
C      YSFD=1.0E+04*YSFD
C      WRITE(3,37)YSFD
37     FORMAT(/,16H THE DATA CAL IS ,E10.3,9H VOLTS/CM)
C      CALIBRATE THE TIME
C      XSFD=0.
C      DO 39 I=1,3
39     XSFD=XSFD+DTVX(I+8)-DTVX(I)
C      XSFD=XSFD+DTVX(12)-DTVX(18)
C      XSFD=24.*DSCALX/XSFD
C      DO 40 I=1,NDP
40     RDT(I)=RDT(I)*XSFD
C      XSFD=1.0E+04*XSFD
C      WRITE(3,41)XSFD
41     FORMAT(/,12H TIME CAL IS ,E10.3,7H SEC/CM)

```

YSFD = Volts per micron conversion factor. This is multiplied by  $10^7$  and printed as volts/cm. The distances involved are actual film distances and because of variations in camera magnification may be significantly different than oscilloscope settings.

XSFD = Seconds per micron conversion factor.

```

C
C
C      FIND THE VOLTS TO INTENSITY TRANSFER FUNCTION.
      XND(1)=0.
      XND(2)=.3
      XND(3)=.6
      XND(4)=1.0
      XND(5)=1.3

      XND(6)=1.6
      XND(7)=2.0
      XND(8)=2.3
      XND(9)=2.6
      XND(10)=3.0
      XND(11)=3.3
      XND(12)=3.6
      XND(13)=4.0
C      CREATE A RELATIVE INTENSITY FOR EACH DRI VOLTAGE.
      DO 42 I=2,NRI
      K=NR1+NRIL+I-1
42      DRII(1)=10.**(-XND(K))
      DRII(1)=0.
C      PLOT TRANSFER FUNCTION.
      CALL FRAME(1)
      CALL MAPGSL(DRI(1),DRI(NRI),DRII(2),DRII(NRI))
      CALL SETCH(37,1,0,0,1,0,0)
      CALL CRTBCD(32HREL INTENSITY DEFLECTION (VOLTS))
      CALL SETCH(1,35,0,0,1,1,0)
      CALL CRTBCD(25HLOG OF RELATIVE INTENSITY)
      CALL SETCH(37,40,0,0,1,0,0)
      WOT 100,43,NC
43      FORMAT(46HREL INTENSITY TRANSFER FUNCTION FOR CHANNEL # ,12)
      CALL TRACE(DRI(2),DRII(2),NRI-1)

```

XND = Neutral density filter number.

DRII = Relative intensity,  $I/I_0$ , for a given measured voltage on the relative intensity calibration film. This is plotted versus DRI on a semi-log graph beginning with the second point to avoid plotting the log of 0.

```

C      SPLINE FIT TRANSFER FUNCTION.
C      CALL SPLINE(DRI,DR11,NRI,C1,C2,C3,C4)
C      FIND REL INTENSITIES FOR RDD VOLTAGES.
      KC=0
      DO 44 I=1,NDP
      DO 45 J=1,NRI-1
      IF(RDD(I).GE.DRI(J).AND.RDD(I).LT.DRI(J+1))GO TO 46
45     CONTINUE
      KC=KC+1
      RDD(I)=0.
      GO TO 44
46     SEP=RDD(I)-DRI(J)
      RDD(I)=SEP*(C3(J)+SEP*(C2(J)+SEP*C1(J)))+C4(J)
44     CONTINUE
      NDP=NDP-KC
C
C      RDD IS NOW RELATIVE INTENSITY.  PLOT RDD.
C
      CALL FRAME(1)
      CALL MAPGSL(RDT(2),RDT(NDP),RDD(3),RDD(NDP))
      CALL SETCH(37,,1,,0,0,1,0,0)
      CALL CRTBCD(24HTIME FROM BANKFIRE (SEC))
      CALL SETCH(1,,35,,0,0,1,1,0)
      CALL CRTBCD(25HLOG OF RELATIVE INTENSITY)
      CALL SETCH(37,,40,,0,0,1,0,0)
      WGT 100,47,NC
47     FORMAT(35HLOG OF REL INTENSITY FOR CHANNEL # ,I2)
      CALL TRACE(RDT(3),RDD(3),NDP-2)
C

```

The voltage to intensity transfer function is fit with cubic splines and this curve is used to convert RDD in volts to RDD expressed as a fraction of  $I_0$ . This relative intensity is plotted as a function of time.

```

C      FIND DATA REL INTENSITIES AT COMMON TIMES.
C      CALL SPLINE(RDT(2),RDD(2),NDP-1,C1,C2,C3,C4)
C
      DO 50 I=1,NUMT
      IF(COMT(1).LT.RDT(2).OR.COMT(1).GT.RDT(NDP))GO TO 53
      DO 51 J=2,NDP-1
      IF(COMT(1).GT.RDT(J).AND.COMT(1).LT.RDT(J+1))GO TO 52
51     CONTINUE
52     SEP=COMT(1)-RDT(J)
      RINT(NC,I)=SEP*(C3(J)+SEP*(C2(J)+SEP*C1(J)))+C4(J)
      GO TO 50
53     RINT(NC,I)=0.
52     CONTINUE
C      RINT IS NOW DATA REL INTENSITY AT COMMON TIMES.
      WRITE(3,24)(COMT(1),RINT(NC,I),I=1,NUMT)

```

The relative intensity versus time transfer function is fit with cubic splines and the relative intensity at common times is then found and labelled RINT.

```

C
C   FIND MEASURED REL INT AT CALIBRATION ENTHALPY.
C
DO 93 I=2,NDP-2
IF (SEM(NC).GT.RDT(I).AND.SEM(NC).LT.RDT(I+1))GO TO 94
93 CONTINUE
94 SEP=SEM(NC)-RDT(I)
SMPI(NC)=SEP*(C3(I)+SEP*(C2(I)+SEP*C1(I)))+C4(I)
WRITE(3,95)NC,SMPI(NC),SEM(NC)
95 FORMAT(2,4HCHAN,13,11H CAL INT IS,E10.2,9H OCCURS AT,E10.2,5H SECS)
CALL SETPCH(1,0,1,0)
CALL POINTC(1HM,SEM(NC),SMPI(NC),1)
C
IF(NC.LT.3)GO TO 5

```

The same spline fit is used to find the relative intensity at the calibration time, SEM, and this is plotted as the letter M on the intensity vs time plot.

This marks the end of the film distance to volts to relative intensity conversion process which is repeated for all three channels.

```

C
C   FORMULATE THE RATIOS OF MEASURED REL INTENSITIES.
C
A=0.
DO 54 I=1,NUMT
IF (RINT(1,I).EQ.A.OR.RINT(2,I).EQ.A)GO TO 55
RINT(4,I)=RINT(1,I)/RINT(2,I)
GO TO 54
55 RINT(4,I)=0.
54 CONTINUE
C
DO 56 I=1,NUMT
IF (RINT(1,I).EQ.A.OR.RINT(3,I).EQ.A)GO TO 57
RINT(5,I)=RINT(1,I)/RINT(3,I)
GO TO 56
57 RINT(5,I)=0.
56 CONTINUE
C
DO 58 I=1,NUMT
IF (RINT(2,I).EQ.A.OR.RINT(3,I).EQ.A)GO TO 59
RINT(6,I)=RINT(2,I)/RINT(3,I)
GO TO 58
59 RINT(6,I)=0.
58 CONTINUE
DO 89 K=4,6
69 WRITE(3,24)(COMT(I),RINT(K,I),I=1,NUMT)
A=0.
B=1.0
CALL FRAME(1)
CALL MAPG(COMT(1),COMT(NUMT),A,B)
CALL SETCH(37,1,0,0,1,0,0)
CALL CRTBCD(24H TIME FROM BANKFIRE (SEC))
CALL SETCH(1,35,0,0,1,1,0)
CALL CRTBCD(13H REL INT RATIO)
CALL SETCH(37,40,0,0,1,0,0)

```

```

      WOT 100,36
      CALL SETPCH(1,0,1,0)
86  FORMAT(21)MEASURED POWER RATIOS)
      DO 90 I=1,NUMT
90  RDD(I)=RINT(4,1)
      CALL TRACEC(1HD,COMT,RDD,NUMT)
      DO 91 I=1,NUMT
91  RDD(I)=RINT(5,1)
      CALL TRACEC(1HE,COMT,RDD,NUMT)
      DO 92 I=1,NUMT
92  RDD(I)=RINT(6,1)
      CALL TRACEC(1HF,COMT,RDD,NUMT)

```

Ratios of the measured relative intensities are formulated and plotted. These are for use in finding the TCT temperatures.

```

      READ(2,10)IFLAG
      IF(IFLAG.EQ.1)GO TO 85
C
C
C
C
      NOW HAVE MESD. (RINT) AND CALC. (CERN) RELATIVE INTENSITIES.
      CALCULATE EM10,EM20,AND EM30.
      EM10=SMPI(1)/TMPC(1)
      EM20=SMPI(2)/TMPC(2)
      EM30=SMPI(3)/TMPC(3)
      WRITE(3,96)EM10
96  FORMAT(/,31)THE TIE POINT CAL FOR CHAN 1 IS,E10.2)
      WRITE(3,140)EM20
140 FORMAT(/,31)THE TIE POINT CAL FOR CHAN 2 IS,E10.2)
      WRITE(3,97)EM30
97  FORMAT(/,31)THE TIE POINT CAL FOR CHAN 3 IS,E10.2)

```

The option to omit the temperature calculation is a 1 in col 5.

EM10 is  $G_1(\lambda_1, T_c)$  with reference to Eq. (3-8). EM20 and EM30 are the same quantities for channels 2 and 3.

```

C
C
C
      CHOOSE FITTING PARAMETER GRID
      READ(2,150)TMAX,TTIE(1),TTIE(2),TTIE(3)
150  FORMAT(4F10.0)
      READ(2,48)A1MIN,A1MAX,NEM1
      READ(2,48)A2MIN,A2MAX,NEM2
      READ(2,48)A3MIN,A3MAX,NEM3

```

```

T=TMAX-TTIE(1)
A1MAX=A1MAX/T
A1MIN=A1MIN/T
T=TMAX-TTIE(2)
A2MAX=A2MAX/T
A2MIN=A2MIN/T
T=TMAX-TTIE(3)
A3MAX=A3MAX/T
A3MIN=A3MIN/T
XNEM1=NEM1-1
XNEM2=NEM2-1
XNEM3=NEM3-1
DTA1=(A1MAX-A1MIN)/XNEM1
DTA2=(A2MAX-A2MIN)/XNEM2
DTA3=(A3MAX-A3MIN)/XNEM3

```

TMAX = Temperature at which the emissivity will reach ALMAX-ALMIN per cent variation.

TTIE = Temperature at the calibration point for each channel.

ALMIN, ALMAX Minimum and maximum fractional changes in emissivity.

ALMAX

NEM1 = Number of emissivity coefficients to try in channel 1.

DTA1 = Change in temperature coefficient for linear emissivity fit.

```

C
C THE OUTSIDE FITTING PARAMETER LOOP.
C
EA1=A1MIN-DTA1
WRITE(3,117)
117 FORMAT(1X,6X,2HA1,13X,2HA2,10X,8HF(A1,A2),/)
PMIN=1.0E+50
DO 100 I=1,NEM1
EA1=EA1+DTA1
EA3=A3MIN-DTA3
C
C SPLINE FIT CALCULATED KERNELS VS TEMP FOR CHANNEL 1.
C
DO 101 K=1,NCK
T=TCERN(K)-TTIE(1)
T=1.+EA1*T
101 CERN(K)=T*CERN(K)
CALL SPLINE(CERN,TCERN,NCK,C1,C2,C3,C4)

```

```

C      FIND CHAN 1 BRIGHT TEMP FOR COMMON TIMES.
C
C      A=0.
C      DO 102 K=1, NUMT
C      IF(RINT(1,K).EQ.A)GO TO 103
C      TRINT=RINT(1,K)*TMPC(1)/SMPI(1)
C      IF(TRINT.LT.CERN(1).OR.TRINT.GT.CERN(NCK))GO TO 103
C      DO 104 J=1, NCK-1
C      IF(TRINT.GE.CERN(J).AND.TRINT.LT.CERN(J+1))GO TO 105
104  CONTINUE
105  SEP=TRINT-CERN(J)
C      BTEMP(1,K)=SEP*(C3(J)+SEP*(C2(J)+SEP*C1(J)))+C4(J)
C      GO TO 102
103  BTEMP(1,K)=0.
102  CONTINUE

```

A temperature coefficient is chosen and the SCT temperature for channel 1 is calculated. The technique is to compare:

$$1+a_i(T-T_c) F_i(T) \text{ with } I_i(T)*F_i(T_c)/I_i(T_c)$$

See Eq. (3-12).

```

C      THE INSIDE FITTING PARAMETER LOOP.
C
C      DO 106 J=1, NEM3
C      EA3=EA3+DTA3
C
C      SPLINE FIT CALCULATED KERNELS FOR CHANNEL 3.
C
C      DO 107 K=1, NCK
C      KK=2*NCK+K
C      T=TCERN(K)-TTIE(3)
C      T=1.+EA3*T
107  CERN(KK)=T*CERN(KK)
C      KK=2*NCK+1
C      CALL SPLINE(CERN(KK), TCERN, NCK, C12, C22, C32, C42)
C
C      FIND CHAN 3 BRIGHT TEMP FOR COMMON TIMES.
C
C      DO 108 K=1, NUMT
C      A=0.
C      IF(RINT(3,K).EQ.A)GO TO 109
C      TRINT=RINT(3,K)*TMPC(3)/SMPI(3)
C      KK=2*NCK+1
C      KKK=3*NCK
C      IF(TRINT.LT.CERN(KK).OR.TRINT.GT.CERN(KKK))GO TO 109
C      DO 110 L=1, NCK-1
C      LL=2*NCK+L
C      IF(TRINT.GE.CERN(LL).AND.TRINT.LT.CERN(LL+1))GO TO 111
110  CONTINUE
111  SEP=TRINT-CERN(LL)
C      BTEMP(3,K)=SEP*(C32(L)+SEP*(C22(L)+SEP*C12(L)))+C42(L)
C      GO TO 108
109  BTEMP(3,K)=0.
108  CONTINUE
C

```

The SCT temperatures are calculated for Channel 3.



```

C      SPLINE FIT CALCULATED KERNELS FOR CHAN1/CHAN3.
C
      CMAX=0.
      DO 112 K=1,NCK
      KK=4*NCK+K
      T1=TCERN(K)-TTIE(1)
      T3=TCERN(K)-TTIE(3)
      T=(1.+EA1*T1)/(1.+EA3*T3)
      CERN(KK)=T*CERN(KK)
      IF(CERN(KK).LT.CMAX)GO TO 112
      CMAX=CERN(KK)
112    CONTINUE
      KK=4*NCK+1
      CALL SPLINE(CERN(KK),TCERN,NCK,C13,C23,C33,C43)
C
C      FIND CHAN1/CHAN3 COLOR TEMP.
C
      A=0.
      COUNT=1.
      DO 113 K=1,NUMT
      IF(RINT(1,K).EQ.A.OR.RINT(3,K).EQ.A)GO TO 114
      TRINT=TMPC(1)*SMPI(3)*RINT(1,K)/(TMPC(3)*SMPI(1)*RINT(3,K))
      IF(TRINT.GT.CMAX)GO TO 114
C
      DO 115 L=1,NCK-1
      LL=4*NCK+L
      IF(TRINT.GE.CERN(LL).AND.TRINT.LT.CERN(LL+1))GO TO 116
115    CONTINUE
116    SEP=TRINT-CERN(LL)
      CTEMP(2,K)=SEP*(C33(L)+SEP*(C23(L)+SEP*C13(L)))+C43(L)
      GO TO 113
114    CTEMP(2,K)=0.
      COUNT=COUNT+1.
113    CONTINUE

```

The TCT temperatures are calculated for chan 1/chan 3.

```

C
C      CALCULATE THE MINIMIZATION FUNCTION F(A1,A2).
C
      Z=0.
      F=0.
      COUNT=COUNT*COUNT
      DO 118 K=1,NUMT
      IF(BTEMP(1,K).EQ.Z)GO TO 118
      IF(BTEMP(3,K).EQ.Z)GO TO 118
      IF(CTEMP(2,K).EQ.Z)GO TO 118
      A=BTEMP(1,K)-BTEMP(3,K)
      B=BTEMP(1,K)-CTEMP(2,K)
      C=BTEMP(3,K)-CTEMP(2,K)
      F=F+A*A+B*B+C*C
      A=0.
      B=0.
      C=0.
118    CONTINUE
119    WRITE(3,119)EA1,EA3,F
      FORMAT(3(2X,E12.3,1X))
C
C      CHECK FOR MINIMUM F.
C
      IF(F.GE.PMIN)GO TO 120
      PMIN=F
      EA1M=EA1
      EA3M=EA3
      DO 123 K=1,NUMT
      EM(1,K)=BTEMP(1,K)
      EM(2,K)=BTEMP(3,K)
123    EM(3,K)=CTEMP(2,K)

```

The minimization function, F, is computed as the sum of the temperature differences squared in the range of overlap. For the minimum F the two SCT temperatures and the one TCT temperature are stored in the parameter EM.

```

120 DO 121 K=1,NCK
    KK=2*NCK+K
    T1=TCERN(K)-TTIE(1)
    T3=TCERN(K)-TTIE(3)
    T=(1.+EA3*T3)/(1.+EA1*T1)
    CERN(KK)=CERN(KK)/(1.+EA3*T3)
    KKK=4*NCK+K
121 CERN(KKK)=T*CERN(KKK)
C
C   END OF INNER LOOP
C
106 CONTINUE
DO 122 K=1,NCK
    T=TCERN(K)-TTIE(1)
122 CERN(K)=CERN(K)/(1.+EA1*T)
C
C   END OUTER LOOP
C
100 CONTINUE

```

After the temperature calculations have been made it is necessary to recover the blackbody functions from the product quantities that had replaced them.

```

C
C   OUTPUT AND PLOT TEMPERATURES AND EMISSIVITIES.
C
DO 76 I=1,2
    WRITE(3,72)I
72  FORMAT(/,36HBRIGHTNESS TEMPERATURES FOR CHANNEL ,15)
    WRITE(3,73)
73  FORMAT(/,3(3X,9HTIME(SEC),4X,14HTEMPERATURE(K)))
    WRITE(3,74)(COMT(K),EM(I,K),K=1,NUMT)
74  FORMAT(3(2X,E12.4,3X,E12.4,1X))
    WRITE(15,75)(COMT(K),EM(I,K),K=1,NUMT)
75  FORMAT(3(E10.3,F10.0))
76  CONTINUE
    M=1
    N=3
    WRITE(3,77)M,N
77  FORMAT(/,24HTHE COLOR TEMP FOR CHAN ,11,11H OVER CHAN ,11,6H ARE--,/)
    WRITE(3,78)
78  FORMAT(/,3(3X,9HTIME(SEC),4X,14HCOLOR TEMP (K)),/)
    WRITE(3,74)(COMT(K),EM(3,K),K=1,NUMT)
    WRITE(15,75)(COMT(K),EM(3,K),K=1,NUMT)
C

```

```

C      PLOT THE TEMPERATURES.
C
      CALL FRAME(1)
      READ(2,79)TMN,TMX,BMIN,BMAX,IRUN
79      FORMAT(4F10.6,15)
      CALL MAPG(TMN,TMX,BMIN,BMAX)
      CALL SETCH(37,1,0,0,1,0,0)
      CALL CRTBCD(25HTIME FROM BANKFIRE (SECS))
      CALL SETCH(1,35,0,0,1,1,0)
      CALL CRTBCD(29HBRIGHTNESS AND COLOR TEMP (K))
      CALL SETCH(37,40,0,0,1,0,0)
      WOT 100,80,IRUN
80      FORMAT(23HTEMPERATURES FOR RUN * ,13)
      CALL SETPCH(1,0,1,0,100)
      DO 125 I=1,NUMT

125      RDD(I)=EM(1,1)
      CALL TRACEC(1HA,COMT,RDD,NUMT)
      DO 126 I=1,NUMT

126      RDD(I)=EM(2,1)
      CALL TRACEC(1HC,COMT,RDD,NUMT)
      DO 127 I=1,NUMT

127      RDD(I)=EM(3,1)
      CALL TRACEC(1HE,COMT,RDD,NUMT)

```

The three temperatures are plotted.

```

C      CALCULATE THE EMISSIVITIES.
C
      NET=31
      RDT(1)=1500.
      DO 131 I=2,NET
131      RDT(I)=RDT(I-1)+100.
      DO 128 I=1,NET
      T1=RDT(I)-TTIE(1)
      T3=RDT(I)-TTIE(3)
      EM(1,I)=EM10*(1.+EA1M*T1)
128      EM(3,I)=EM30*(1.+EA3M*T3)

```

The emissivities calculated here actually include the geometrical calibration factor,  $G_i$ , which is undetermined (see Eq. 3-10).

```

C      OUTPUT THE EMISSIVITIES.
C
      DO 81 I=1,3,2
      WRITE(3,82)I
82      FORMAT(/,25HEMISSIVITIES FOR CHANNEL ,15)
      WRITE(3,83)
81      WRITE(3,74)(RDT(K),EM(I,K),K=1,NET)
83      FORMAT(/,3(3X,9HTIME(SEC),4X,12HEMISSIVITIES,2X))

C      PLOT EMISSIVITIES
C
      CALL FRAME(1)
      T1=TMAX-TTIE(1)
      T3=TMAX-TTIE(3)
      TMIN=1500.
      B1M=1.5*EM10*(1.+EA1M*T1)
      B3M=1.5*EM30*(1.+EA3M*T3)
      BMAX=B3M
      IF(B1M GT. B3M)BMAX=B1M
      T1=TMIN-TTIE(1)
      T3=TMIN-TTIE(3)

```

```

B1M=.5*EM10*(1.+EA1M*T1)
B3M=.5*EM30*(1.+EA3M*T3)
BMIN=B3M
IF(B1M.LT.B3M)BMIN=B1M
CALL MAPG(TMIN,TMAX,BMIN,BMAX)
CALL SETCH(37.,1.,0,0,1,0,0)
CALL CRTBCD(15HTEMPERATURE (K))
CALL SETCH(1.,35.,0,0,1,1,0)
CALL CRTBCD(10HEMISSIVITY)
CALL SETCH(37.,40.,0,0,1,0,0)
WOT 100,84,IRUN
84  FORMAT(23HEMISSIVITIES FOR RUN * ,13)
   CALL SETPCH(1,0,1,0,100)
   DO 128 I=1,NET
129  RDD(I)=EM(I,1)
   CALL TRACEC(1HA, RDT, RDD, NET)
   DO 130 I=1,NET
130  RDD(I)=EM(3,I)
   CALL TRACEC(1HC, RDT, RDD, NET)
85  CALL EXIT(1)
   END

```

$G_i(\lambda_i, T)$  is plotted for all temperatures. This has no absolute emissivity information in it because of the undetermined  $G_i$ .

```

C  SUBROUTINE SPLINE(X,Y,N,A,B,C,D)
C  SUBROUTINE SPLINE TAKES N (X,Y(X)) UNEVENLY SPACED DATA POINTS AND
C  FITS A CUBIC SPLINE TO EACH OF THE N-1 INTERVALS. (REF. GERALD
C  PAGE 290). THE PROGRAM USES GAUSSIAN ELIMINATION TO SOLVE FOR
C  THE SECOND DERIVATIVE OF THE CUBIC SPLINE AT EACH OF THE N DATA
C  POINTS. REF. GERALD PAGE 164. INPUT PARAMETERS ARE...
C  1. N=THE NUMBER OF DATA POINTS (MAXIMUM OF 500).
C  2. (X,Y)=THE X AND Y VALUES OF THE DATA POINTS..
C  OUTPUT PARAMETERS ARE N-1 VALUES OF A, B, C, AND D. THESE ARE THE
C  COEFFICIENTS OF THE N-1 CUBIC SPLINES...
C  Y(X)=A(I)*(X-X(I))**3.+B(I)*(X-X(I))**2.+C(I)*(X-X(I))+D(I).
C  IN ORDER TO MAKE THE MATRIC TRIDIAGONAL BOUNDARY CONDITIONS WERE
C  CHOSEN THAT MAKE THE END SPLINES PARABOLIC AND NOT CUBIC.
C  DIMENSION X(N),Y(N),A(N),B(N),C(N),D(N),H(501),S(501)
C
C  P/R T U.. CONSTRUCT THE MATRIX
C
C  DO 10 I=1,N-1
10  H(I)=X(I+1)-X(I)
C  A=ABOVE DIAGONAL, D=DIAGONAL, B=BELOW DIAGONAL,C=CONSTANT VECTOR.
C  THE SECOND DERIVATIVES ARE STORED IN S.
C  D(I)=1.
C  A(I)=-1.
C  C(I)=0.
C  B(N)=-1.
C  D(N)=1.
C  C(N)=0.
C  DO 11 I=2,N-1
C  B(I)=H(I-1)
C  D(I)=2.*(H(I-1)+H(I))
C  A(I)=H(I)
C  C(I)=6.*(Y(I+1)-Y(I))/H(I)-(Y(I)-Y(I-1))/H(I-1))
11  CONTINUE
C  TRIANGULARIZE THE MATRIX
C  DO 12 I=2,N
C  R=B(I)/D(I-1)
C  D(I)=D(I)-R*A(I-1)
C  C(I)=C(I)-R*C(I-1)
12  CONTINUE

```

```

C      BACK SUBSTITUTION
      S(N)=C(N)/D(N)
      DO 14 I=2,N
        J=N-I+1
        S(J)=(C(J)-A(J)*S(J+1))/D(J)
14     CONTINUE
C      PRINT OUT HEADING
C      WRITE(3,200)N
200    FORMAT(/,35H SOLUTION TO TRIDIAGONAL SYSTEM OF ,14,26H EQUATIONS B
      1Y ELIMINATION ,//)
C      PRINT OUT MATRIX SOLUTION
C      WRITE(3,201)(I,S(I),I=1,5)
201    FORMAT(3H S( ,14,5H ) = ,E14,7)
C      CALCULATE THE SPLINE PARAMETERS
      DO 15 I=1,N-1
        A(I)=(S(I+1)-S(I))/(6.*H(I))
        B(I)=S(I)/2
        C(I)=(Y(I+1)-Y(I))/H(I)-(H(I)/6.)*(2.*S(I)+S(I+1))
        D(I)=Y(I)
15     CONTINUE
C      OUTPUT SPLINE PARAMETERS
C      WRITE(3,210)
210    FORMAT(/,9H INTERVAL,3X,4HA(1),9X,4HB(1),10X,4HC(1),11X,4HD(1))
C      WRITE(3,211)(I,A(I),B(I),C(I),D(I),I=1,5)
211    FORMAT(15,4X,E12.4,3X,E12.4,3X,E12.4,3X,E12.4)
      RETURN
      END

```

## APPENDIX C. FREE ELECTRON RELAXATION TIME

In developing the expression for free electron resistivity, Eq. (5-4), many of the physical considerations are deferred and consolidated into the relaxation time,  $\tau_f$ , which is a representative time between electron-ion collisions for electrons at the Fermi surface. The method of Mott and Jones<sup>(71)</sup> is used to establish a reasonable expression for  $\tau_f$ . They examine the number of electrons within a specific volume of K-space under the influence of an applied electric field and subject to electron-ion collisions. At equilibrium the rate of change of the distribution function due to collisions should be equal and opposite to that rate due to the applied electric field.

It can be shown that the volume in K-space occupied by one electronic state is  $\left(\frac{2\pi}{L}\right)^3 \left(\frac{1}{2}\right)$  where  $L^3$  is the volume of the sample and the  $1/2$  arises from the two possible spin orientations. Therefore, the number of states per unit K-space volume per unit volume is  $2/(2\pi)^3$ , and the number of electrons per unit volume within a volume element of K-space is

$$\frac{2d^3\vec{K}}{(2\pi)^3} f_0(\vec{K}) \quad (C-1)$$

where  $f_0(\vec{K})$  is the Fermi-Dirac distribution function which expresses the probability of a given state's being occupied.

$$f_0(\vec{K}) = \left[ e^{(E-E_f)/K_B T} + 1 \right]^{-1} \quad (C-2)$$

Under the influence of a field applied in the direction of  $K_x$  the distribution function will change and this change can be evaluated in terms of the K-space equation of motion of the electrons.

$$\frac{dp_x}{dt} = e\epsilon = \hbar \frac{dk_x}{dt} + K_x(t) = K_x(0) + \frac{e\epsilon t}{\hbar} \quad (C-3)$$

Therefore the equilibrium distribution function is:

$$f_0(K_x - \frac{e\epsilon t}{\hbar}, K_y, K_z) = f_0(K_{x0}, K_y, K_z) \quad (C-4)$$

The rate of change in the distribution function due to the applied field is:

$$\left. \frac{df}{dt} \right|_{\text{field}} = \frac{\partial f_0}{\partial K_{x0}} \frac{dK_{x0}}{dt} = \frac{\partial f_0}{\partial K_{x0}} \frac{e\epsilon}{\hbar} = \frac{-df_0}{dE} \frac{dE}{dK} \frac{dK}{dK_{x0}} \frac{e\epsilon}{\hbar} = \frac{-df_0}{dK} \frac{K_x}{K} \frac{e\epsilon}{\hbar} \quad (C-5)$$

A one term expansion of the distribution function about its equilibrium value yields:

$$f(\vec{k}) = f_0(\vec{k}) - \frac{df_0}{dK} \frac{K_x}{K} \frac{e\epsilon}{\hbar} \tau = f_0(\vec{k}) + g(\vec{k}) \quad (C-6)$$

Because of the factor  $\frac{df_0}{dE}, \left. \frac{df}{dt} \right|_{\text{field}}$  has significant value only at the Fermi surface (i.e.  $E = E_f$ ).

To determine the rate of change of  $f(k)$  due to collisions it is necessary to examine the collisionally induced flux of electrons through  $d^3\vec{k}$ . The number of electrons scattered out of  $d^3\vec{k}$  is the product of the number of electrons in  $d^3\vec{k}$ , the probability of finding an unoccupied state at  $\vec{k}'$ , and the probability of a  $\vec{k}$  to  $\vec{k}'$  transition summed over all possible  $\vec{k}'$ . If the scattering process is conservative the summation proceeds over a surface of constant radius,  $k_f$ .

$$N_{\text{out}} = 2 \frac{d^3 \vec{k}}{(2\pi)^3} f(\vec{k}) \int [1-f(\vec{k}')] P(\vec{k}, \vec{k}') dS' \quad (\text{C-7})$$

Analogously the number of electrons scattered into  $d^3 \vec{k}$  is the product of the number of unoccupied states in  $d^3 \vec{k}$ , the probability of a state at  $\vec{k}'$  being occupied, and the probability of a  $\vec{k}'$  to  $\vec{k}$  transition summed over all  $\vec{k}'$  on the Fermi surface.

$$N_{\text{in}} = 2 \frac{d^3 \vec{k}}{(2\pi)^3} [1-f(\vec{k})] \int f(\vec{k}') P(\vec{k}', \vec{k}) dS' \quad (\text{C-8})$$

Subtracting (C-7) from (C-8) and assuming  $P(\vec{k}\vec{k}') = P(\vec{k}'\vec{k})$  the rate of change of  $f(\vec{k})$  due to collisions may be expressed as:

$$\left. \frac{df}{dt} \right|_{\text{collisions}} = \int f(\vec{k}') P(\vec{k}', \vec{k}) dS' - f(\vec{k}) \int P(\vec{k}, \vec{k}') dS' \quad (\text{C-9})$$

Writing  $f(\vec{k}) = f_0(\vec{k}) + g(\vec{k})$  and recognizing that  $f_0(\vec{k})$  is a function only of the magnitude of  $k$  Eq. (C-9) becomes:

$$\left. \frac{df}{dt} \right|_{\text{collisions}} = \int [g(\vec{k}') - g(\vec{k})] P(\vec{k}, \vec{k}') dS' \quad (\text{C-10})$$

At equilibrium  $\left. \frac{df}{dt} \right|_{\text{collisions}} = - \left. \frac{df}{dt} \right|_{\text{field}}$  yielding:

$$\frac{df_0}{dE} \frac{dE}{dK} \frac{K_x}{K} \frac{e\epsilon}{h} = \int [g(\vec{k}') - g(\vec{k})] P(\vec{k}, \vec{k}') dS' \quad (\text{C-11})$$

Using Eq. (A-6), the definition of  $g(\vec{k})$ , and the fact that  $|\vec{k}'| = |\vec{k}| = k_F$  Eq. (C-11) becomes:



$$\frac{1}{\tau} = \int \left[ 1 - \frac{K'_x}{K_x} \right] P(\vec{k}, \vec{k}') dS' \quad (C-12)$$

The indicated integration is performed most easily by choosing a coordinate system centered on the scattering site with  $\theta$  being the angle between  $\vec{k}$  and  $\vec{k}'$ . In this case

$$K'_x = |\vec{k}'| \cos \theta = |\vec{k}| \cos \theta$$

$$K_x = |\vec{k}| \quad (C-13)$$

$$dS' = 2\pi K^2 \sin \theta d\theta$$

Assuming that  $P(\vec{k}, \vec{k}')$  is a function only of  $\theta$  and not of  $k$  the expression for the relaxation time at the Fermi surface becomes:

$$\frac{1}{\tau_f} = 2\pi K_F^2 \int_0^\pi (1 - \cos \theta) P(\theta) \sin \theta d\theta \quad (C-14)$$

which is the result expressed in Eq. (5-5). As pointed out in Eq. (5-6)  $P(\theta)$  is a transition rate which is given by: <sup>(72)</sup>

$$P(\theta) = P_{\vec{k}, \vec{k}+\vec{q}} = \frac{2\pi}{\hbar} \left| \langle \vec{k}+\vec{q} | W(\vec{r}) | \vec{k} \rangle \right|^2 n(E') \quad (C-15)$$

where  $n(E')$  is the density of states available to the electron at the Fermi surface. The matrix element of Eq. (A-15) will connect only states

of identical spin so that the number of accessible states per unit volume of k-space is:

$$\frac{1}{2} \frac{2}{(2\pi/L)^3} = \frac{\Omega}{(2\pi)^3} \quad (C-16)$$

where  $\Omega$  is the sample volume in direct space. The number of states within  $\delta k'$  of  $k'$  on the k-space surface  $ds'$  is therefore  $\delta k' ds' \Omega / (2\pi)^3$ . Noting that  $\delta E' = \frac{dE'}{dk'}$ ,  $\delta k'$  the number of states near  $ds'$  may also be expressed as  $ds' \Omega / (2\pi)^3 \frac{\delta E'}{dE'/dk'}$ , with the result that:

$$n(E') = \frac{\text{number of accessible states near } ds'}{\text{unit energy}} = \frac{ds' \Omega}{(2\pi)^3 \frac{dE'}{dk'}} \quad (C-17)$$

Eq. (C-14) becomes:

$$\frac{1}{\tau} = \int_0^\pi (1 - \cos\theta) P_{\vec{k}+\vec{q}, \vec{k}} dS' = \frac{\Omega}{4\pi^2 \hbar \frac{dE'}{dk'}} \int |\langle \vec{k}+\vec{q} | W | \vec{k} \rangle|^2 (1 - \cos\theta) dS'$$

or since  $E_f = \frac{\hbar^2 k_f^2}{2m}$

$$\frac{1}{\tau} = \frac{\Omega k_f}{2\pi \hbar^3} \int_0^\pi |\langle \vec{k}+\vec{q} | W | \vec{k} \rangle|^2 (1 - \cos\theta) \sin\theta d\theta \quad (C-18)$$

As alluded to in Eq. (5-7) the matrix element may be factored as follows: (73)

$$\langle \vec{k}+\vec{q} | W(\vec{r}) | \vec{k} \rangle = \frac{1}{\Omega} \int e^{-i(\vec{k}+\vec{q}) \cdot \vec{r}} \sum_j \omega(|\vec{r}-\vec{r}_j|) e^{i\vec{k} \cdot \vec{r}} d^3r$$

where  $\omega(|\vec{r}-\vec{r}_j|)$  is the potential at  $\vec{r}$  due to an individual ion at position  $\vec{r}_j$ . Multiplying and dividing by  $e^{i(\vec{k}+\vec{q})\cdot\vec{r}_j}$  reduces the element to:

$$\langle \vec{k}+\vec{q} | W(\vec{r}) | \vec{k} \rangle = \frac{\sum_j e^{-i\vec{q}\cdot\vec{r}_j}}{\Omega} \int e^{-i(\vec{k}+\vec{q})\cdot(\vec{r}-\vec{r}_j)} \omega(|\vec{r}-\vec{r}_j|) e^{i\vec{k}\cdot(\vec{r}-\vec{r}_j)} d^3\vec{r}$$

Noting that  $\vec{r}-\vec{r}_j$  is a dummy variable of integration the matrix element reduces to Eq. (5-7):

$$\langle \vec{k}+\vec{q} | W(\vec{r}) | \vec{k} \rangle = S(\vec{q}) \langle \vec{k}+\vec{q} | \omega(\vec{r}) | \vec{k} \rangle \quad (\text{C-19})$$

where  $S(\vec{q})$  is the structure factor defined in Eq. (5-8) and

$$\langle \vec{k}+\vec{q} | \omega(\vec{r}) | \vec{k} \rangle = \frac{1}{\Omega} \int e^{-i(\vec{k}+\vec{q})\cdot\vec{r}} \omega(\vec{r}) e^{i\vec{k}\cdot\vec{r}} d^3\vec{r}$$

is the form factor.

Elementary trigonometric identities,  $1 - \cos \theta = 2 \sin^2 \frac{\theta}{2}$  and  $\sin \theta = 2 \sin \frac{\theta}{2} \cos \frac{\theta}{2}$ , and Eq. (C-19) transform Eq. (C-18) into:

$$\frac{1}{\tau} = \frac{\Omega m K_f}{2\pi \hbar^3} \int_0^\pi S^2(\vec{q}) (\langle \vec{k}+\vec{q} | \omega(\vec{r}) | \vec{k} \rangle)^2 4 \sin^3 \frac{\theta}{2} \cos \frac{\theta}{2} d\theta \quad (\text{C-20})$$

For elastic scattering  $q = 2k_f \sin \frac{\theta}{2}$ . Thus switching the variable of integration to  $q/2k_f$  the relaxation time becomes:

$$\frac{1}{\tau} = \frac{\Omega n K_f}{\pi h^3} \int_0^1 S^2(\vec{q}) [\langle \vec{K} + \vec{q} | \omega(\vec{r}) | \vec{K} \rangle]^2 \left( \frac{q}{2K_f} \right)^3 d\left( \frac{q}{2K_f} \right) \quad (C-21)$$

which leads to the resistivity of Eq. (5-9).

## APPENDIX D. LOCAL POTENTIAL FORM FACTORS

Application of the Ziman nearly free electron theory to calculation of metal resistivities (Eq. 5-10) requires choosing an electron-ion interaction potential. For this work a series of simple "bare sphere" potentials were evaluated and used in Eq. (5-10) with a suitable dielectric function,  $\epsilon(K)$ . More involved Heine-Abarenkov potentials were not tested because it was felt that the degree of complexity was not warranted by the approximate nature of the theory.<sup>(79,90)</sup> This appendix deals with the chosen bare sphere potentials that model the ion-electron interaction and the dielectric function which best accommodates electron exchange and correlation effects.

The least complicated potential used is the Ashcroft hollow core for which the electron ion interaction is assumed to be coulombic beyond a core radius  $R_c$  and to be zero within that radius.

$$V(r) = \begin{cases} 0 & r < R_c \\ \frac{-Z_{\text{eff}}e^2}{r} & r > R_c \end{cases} \quad (\text{D-1})$$

Ashcroft has shown the form factor resulting from this potential to be in good agreement with more complex Heine-Abarenkov forms.<sup>(18)</sup> The bare sphere form factor is defined as:

$$V(q) = \langle \vec{K} + \vec{q} | V(\vec{r}) | \vec{K} \rangle = \frac{1}{\Omega_0} \int d^3r \left[ \frac{-Z_{\text{eff}}e^2}{r} \right] e^{-i\vec{q} \cdot \vec{r}} \quad (\text{D-2})$$

where  $\Omega_0$  = volume per atom. Choosing a coordinate system centered at the scattering center whose polar axis is coincident with  $K$  reduces Eq.

(D-2) to:

$$V(q) = \frac{-2\pi Z_{\text{eff}} e^2}{\Omega_0} \int_{R_C}^{\infty} \int_0^{\pi} r \sin \theta e^{-iqr \cos \theta} d\theta dr = \frac{-4\pi Z_{\text{eff}} e^2}{\Omega_0 q} \int_{R_C}^{\infty} \sin qr dr \quad (\text{D-3})$$

The integration of the last expression requires a ploy to circumvent the divergency.

$$\lim_{\mu \rightarrow 0} \int_{R_C}^{\infty} e^{-\mu r} \sin qr dr = \int_{R_C}^{\infty} \sin qr dr \quad (\text{D-4})$$

The result is:

$$V(q) = \frac{-4Z_{\text{eff}} e^2 \cos qR_C}{\Omega_0 q^2} \quad (\text{D-5})$$

The Ashcroft hollow core form factor includes only one parameter,  $R_C$ , through which to match theory to data.

A second model consists of a coulomb potential outside the core and a constant potential within. Labelled here the Heine-Azarenkov potential it is in fact less complex than that defined in reference 79.

$$V_0 = \frac{Z_{\text{eff}} e^2}{R_C} \quad \text{u} \quad r < R_C$$

$$V(\vec{r}) = \frac{-Z_{\text{eff}} e^2}{r} \quad r > R_C \quad (\text{D-6})$$

Defined as before the form factor becomes: (86)

$$V(q) = \frac{-4\pi Z_{\text{eff}} e^2}{q^2 \Omega_0} \left[ (1+u) \cos q R_C - u \frac{\sin q R_C}{q R_C} \right] \quad (\text{D-7})$$

where the second parameter,  $u$ , gives the relative height of the core potential in terms of the coulomb potential at  $R_C$ .

A third model, identified here as the Harrison potential and discussed in detail by Egelstaff<sup>(77)</sup> is the superposition of coulombic and exponential terms.

$$V(r) = \frac{-Z_{\text{eff}} e^2}{r} + C e^{-r/R_C} \quad 0 \leq r \quad (\text{D-8})$$

The second term is intended to cancel the coulombic attraction in the core region reflecting the fact that the free electrons are excluded from occupying the ionic bound states. This effect has an effective range of approximately atomic dimensions, i.e. a characteristic radius  $R_C$ .

Again choosing the coordinate system of Eq. (D-3) the Harrison form factor is

$$V(q) = \left[ \frac{-4\pi Z_{\text{eff}} e^2}{q^2} + \frac{8\pi C R_C^3}{[1+(q R_C)^2]^2} \right] \frac{1}{\Omega_0} \quad (\text{D-9})$$

The additional parameter chosen to correctly model the data is  $c$ , the height of the repulsive component at core center.

The form factors of Eqs. (D-5), (D-7), and (D-9) are known as local potential form factors, and their use should be contrasted to the more usual approach taken by Anomalu and Heine among others.<sup>(79)</sup> As outlined by Evans,<sup>(81)</sup> the latter procedure begins with the definition of a single ion bare sphere potential:

$$\omega_0(r) = \frac{-Z_{\text{eff}}}{r} - \sum_{\ell=0}^{\ell_0} \theta(R_\ell - r) \left( A_\ell \frac{-Z_{\text{eff}}}{r} \right) P_\ell \quad (\text{D-10})$$

$$\theta(x) = 1 \quad x > 0$$

$$\theta(x) = 0 \quad x < 0$$

$$P_\ell = \sum_{m=-\ell}^{\ell} |Y_\ell^m\rangle \langle Y_\ell^m|$$

where  $P_\ell$  as defined is the projection operator that picks out the component of the wave function with angular momentum  $\ell$ . The parameters  $A_\ell$  are determined by choosing that potential which will reproduce measured eigenvalues for an isolated ion. The  $R_\ell$ 's are then chosen through a variational technique seeking to produce the smoothest possible model wave function.<sup>(81)</sup> Such a requirement results in  $A_\ell = \frac{Z}{R_\ell}$ , i.e. the "best" wave function is produced for those values of  $R_\ell$  for which the discontinuity in (D-10) is eliminated. This Heine-Abarenkov procedure in some cases produces a potential remarkably similar in form to Eq. (D-8) (see reference 79, Eq. 24).

The form factors discussed have so far incorporated the physics of the electron-ion interaction. It can be shown that it is possible to modify these bare ion form factors with a dielectric function that accommodates the electron-electron interaction and the effects of electron exchange and correlation. We outline here a treatment given by Harrison<sup>(90)</sup> that demonstrates that inclusion of electron-electron interactions leads to a bare sphere form factor modified by the Hartree or Lindhard dielectric function. The potential energy at any point  $\vec{r}$  is



now defined as  $W(\vec{r}) = W^0(\vec{r}) + W^1(\vec{r})$  where  $W^0(\vec{r})$  is that due to the electron-ion interaction and  $W^1(\vec{r})$  is the contribution of the electron-electron interaction. Harrison's method is to compare the electron density computed quantum mechanically with the electron density derived from Poisson's relation and thus deduce the relationship between the total form factor,  $\langle \vec{K}+\vec{q} | W(\vec{r}) | \vec{K} \rangle$  and the bare ion form factor  $\langle \vec{K}+\vec{q} | W^0(\vec{r}) | \vec{K} \rangle$ .

The Kth wave function may be expressed as an expansion in K-space:

$$\begin{aligned} \phi_K &= \sum_{\vec{q}} a_{\vec{q}}(\vec{K}) |\vec{K}+\vec{q}\rangle \\ &= \frac{1}{\Omega^{1/2}} a_0(\vec{K}) e^{i\vec{K}\cdot\vec{r}} + \frac{1}{\Omega^{1/2}} \sum_{\vec{q} \neq 0} a_{\vec{q}}(\vec{K}) e^{i(\vec{K}+\vec{q})\cdot\vec{r}} \end{aligned} \quad (D-11)$$

where in the spirit of perturbation theory, the wave functions are almost plane waves, i.e.  $a_0(\vec{K}) \approx 1$  and the remaining  $a_{\vec{q}}(\vec{K})$  are small by comparison. Consequently the Kth state probability density is approximately:

$$\phi_{K^*} \phi_K \approx \frac{1}{\Omega} \left\{ 1 + \sum_{\vec{q} \neq 0} [a_{\vec{q}}(\vec{K}) e^{i\vec{q}\cdot\vec{r}} + a_{\vec{q}}^*(\vec{K}) e^{-i\vec{q}\cdot\vec{r}}] \right\} \quad (D-12)$$

and the electron density at any point,  $\vec{r}$ , is  $n(\vec{r}) = \sum_{\vec{K}} \phi_{K^*} \phi_K$  where the K summation is over all occupied states in the free electron Fermi sphere. If  $\sum_{\vec{K}}$  is replaced by  $\frac{2\Omega}{(2\pi)^3} \int d^3K$  the electron density becomes:

$$n(\vec{r}) = \frac{2}{(2\pi)^3} \int \left\{ 1 + \sum_{\vec{q} \neq 0} [a_{\vec{q}}(\vec{K}) e^{i\vec{q}\cdot\vec{r}} + a_{\vec{q}}^*(\vec{K}) e^{-i\vec{q}\cdot\vec{r}}] \right\} d^3K \quad (D-13)$$

The first term is the constant background that balances the ionic charge distribution while the summation terms reflect the electron-electron induced charge non-uniformity.  $a_q^*(\vec{k}) e^{-i\vec{q}\cdot\vec{r}}$  can be replaced by  $a_{-q}^*(\vec{k}) e^{i\vec{q}\cdot\vec{r}}$  without changing  $n(\vec{r})$ , and similarly  $a_{-q}^*(\vec{k})$  can be replaced with  $a_{-q}^*(-\vec{k})$ . (Due to the symmetry of the Fermi sphere for every wave vector there is another equal in magnitude and opposite in sign, and any summation or integration over accessible phase space includes both.) Further,  $a_{-q}^*(-\vec{k}) = a_q(\vec{k})$ . Therefore, neglecting the constant term

$$n(\vec{r}) = \frac{2}{(2\pi)^3} \int \sum_{q \neq 0} 2a_q(\vec{k}) e^{i\vec{q}\cdot\vec{r}} d^3\vec{k} = \sum_{q \neq 0} n_q e^{i\vec{q}\cdot\vec{r}} \quad (D-14)$$

where

$$n_q = \frac{4}{(2\pi)^3} \int d^3\vec{k} a_q(\vec{k})$$

Noting that:

$$a_q(\vec{k}) = \frac{\langle \vec{k} + \vec{q} | W(\vec{r}) | \vec{k} \rangle}{\hbar^2 / 2m (k^2 - |\vec{k} + \vec{q}|^2)} \quad \text{for } q \neq 0$$

the  $q$  Fourier component of the electron density is then:

$$n_q = \frac{4}{(2\pi)^3} \int \frac{d^3\vec{k} \langle \vec{k} + \vec{q} | W(\vec{r}) | \vec{k} \rangle}{\hbar^2 / 2m (k^2 - |\vec{k} + \vec{q}|^2)} \quad (D-15)$$

The matrix element is independent of  $K$  if the potential can be assumed to be local. Choosing  $K_z$  to be that component of the incident wave vector,  $K$ , in the direction of  $q$ , the electron density component becomes:

$$n_q = \frac{4}{(2\pi)^3} \int \frac{\pi(K_f^2 - K_z^2) dK_z}{\hbar^2/2m (-q^2 - 2qK_z)} \quad (D-16)$$

Integration of Eq. (D-16) yields:

$$n_q = \frac{-mK_f \langle \vec{K} + \vec{q} | W | \vec{K} \rangle}{2\pi^2 \hbar^2} \left[ \frac{1-x^2}{2x} \ln \left| \frac{1+x}{1-x} \right| + 1 \right] \quad (D-17)$$

where  $x = \frac{q}{2K_f}$

In addition to the quantum mechanical approach that produced Eq. (D-17) it is also possible to use Poisson's equation to find an expression for the potential at a point  $\vec{r}$  in terms of the charge density, and conversely to represent the charge density in terms of the potential. Recalling that  $W(\vec{r}) = W^0(\vec{r}) + W^1(\vec{r})$  is an expression for the potential energy at point  $\vec{r}$  in terms of electron-ion and electron-electron interactions the potential may be represented by:

$$\phi(\vec{r}) = \phi^0(\vec{r}) + \phi'(\vec{r}) = \sum_R \frac{Z_{eff} e}{|\vec{r} - \vec{R}|} + \phi'(r) \quad (D-18)$$

where  $\vec{R}$  is an ion site. The charge density is:

$$\rho(\vec{r}) = \sum_{\vec{R}} Ze\delta(\vec{r}-\vec{R}) - n(\vec{r})e \quad (\text{D-19})$$

where  $n(\vec{r})$  is the electron density. Poisson's equation ( $\nabla^2\phi = -4\pi\rho$ ) can be expressed as:

$$\nabla^2 \left\{ \sum_{\vec{R}} \frac{Ze}{|\vec{r}-\vec{R}|} + \phi'(\vec{r}) \right\} = -4\pi \sum_{\vec{R}} Ze\delta(\vec{r}-\vec{R}) + 4\pi n(\vec{r})e$$

which, in view of the identity  $\nabla^2 \left( \frac{1}{|\vec{r}-\vec{R}|} \right) = -4\pi\delta(\vec{r}-\vec{R})$  reduces to:

$$-4\pi \sum_{\vec{R}} Ze\delta(\vec{r}-\vec{R}) + \nabla^2 \phi'(\vec{r}) = -4\pi \sum_{\vec{R}} Ze\delta(\vec{r}-\vec{R}) + 4\pi n(\vec{r})e$$

$$\text{or: } \nabla^2 \phi'(\vec{r}) = 4\pi n(\vec{r})e \quad (\text{D-20})$$

In terms of potential energy Eq. (D-20) is  $\nabla^2 W'(\vec{r}) = 4\pi n(\vec{r})e^2$

Fourier transforming the Poisson expression yields:

$$q^2 W_q' = 4\pi e^2 n_q \quad (\text{D-21})$$

Making use of the fact that:

$$W_q' = \langle \vec{K} + \vec{q} | W'(\vec{r}) | \vec{K} \rangle = \langle \vec{K} + \vec{q} | W(\vec{r}) | \vec{K} \rangle - \langle \vec{K} + \vec{q} | W^0(\vec{r}) | \vec{K} \rangle$$

A second expression for the  $q$ th component of the electron density is found to be:

$$n_q = \frac{q^2}{4\pi e^2} \left\{ \langle \vec{k} + \vec{q} | W(\vec{r}) | \vec{k} \rangle - \langle \vec{k} + \vec{q} | W^0(\vec{r}) | \vec{k} \rangle \right\} \quad (D-22)$$

Comparison of Eq. (D-17) and (D-22) leads to a simple relationship between the bare sphere and more complete matrix elements.

$$\langle \vec{k} + \vec{q} | W | \vec{k} \rangle = \frac{\langle \vec{k} + \vec{q} | W^0 | \vec{k} \rangle}{\epsilon(q)} \quad (D-23)$$

$$\epsilon(q) = 1 + \frac{me^2}{2\pi\hbar^3 K_F x^2} \left[ \frac{1-x^2}{2x} \ln \left| \frac{1+x}{1-x} \right| + 1 \right]$$

Eq. (D-23) expresses the Hartree or Linhard dielectric function which models the electro-static repulsion of the free electrons but does not account for correlation or exchange. The latter effects are accommodated as indicated with respect to Eqs. (5-17) and (5-18).

To synopsise, the electrical resistivity calculations of this work were done using the matrix element of Eq. (5-17). The bare sphere potentials employed are the localized models of Eqs. (D-1), (D-6), and (D-8). Consideration has been given to electron-ion, electron-electron, and electron correlation and exchange interactions.